LONDON, METEOROLOGICAL OFFICE.

Met.O.19 Branch Memorandum No.63.

Design of rocket payloads to measure mesospheric ozone. By VAUGHAN,G.and SEYMOUR,J.S.

London,Met.Off.,Met.O.19 Branch Mem.No.63 1981,31cm.Pp.[ii]+19,28 pls.App.19.16 Refs.

An unofficial document - restriction on first page to be observed.

MET O 19 BRANCH MEMORANDUM NO 63

DESIGN OF ROCKET PAYLOADS TO MEASURE MESOSPHERIC OZONE

by

G Vaughan and J S Seymour

September 1981

Met O 19
(Satellite Meteorology)
Meteorological Office
London Road
Bracknell
Berkshire
RG12 2SZ

Contents

1. Introduction

A rocket experiment was mounted in October 1979 to investigate the diurnal variation of ozone in the mesosphere. The scientific background of the experiment, details of the flights, data analysis, results and their interpretation will be presented by G Vaughan (Oxford University D.Phil. thesis, to be published 1982). The results have been summarised and will be published elsewhere. This paper aims to record details of the ozone and ancilliary sensors used in the experiment, and the criteria which had to be satisfied in order to conduct it.

The principle of the experiments was that of absorption spectroscopy. In the mesosphere ultraviolet radiation with wavelength less than 310 nm is absorbed by ozone through:

$$O_3 + h\nu\ (< 310\,nm) \rightarrow O_2\ (^1\Delta_g) + O(^1D)$$

The variation of absorption coefficient with wavelength is shown in fig 5.2b; it is smooth and is known to a good degree of accuracy. Solar (or lunar) ultraviolet radiation is thus absorbed by ozone in a layer of the atmosphere, whose depth and height depends upon the wavelength and the geometry of illumination. A sensor with narrow optical bandwidth measuring the intensity of such radiation will show an extinction curve as it ascends (or descends) through the layer. From the shape of the extinction curve (known as the attenuation profile) the ozone path totals between rocket and source may be calculated, and hence ozone concentrations may be deduced.

The Meteorological Office has considerable experience of such experiments, utilising the advantages of occultation geometry (see Appendix C for a note on occultation geometry). Miller and Ryder (1973) reported on measurements made at sunset from Woomera and Fort Churchill, on Skylark and Black Brant rockets respectively, and other Skylark experiments were flown by the same group in the early 1970s. The experience gained with these flights, both in the sensor design and data reduction, was extensively used in the work described here. However, technological advances, especially in the fields of electronics and interference filters, demanded a fresh look at the design of the sensors.

Four rockets were available for the diurnal variation experiment, which was to consist of one night time and two daytime measurements and one at sunrise or sunset (see table 1). Since the purpose of the experiment was to measure the change in ozone concentrations from night to day, its success depended on a good night time measurement. This required using the moon as the source of ultraviolet radiation, which introduced the problems of photon noise in the results, because of the weak illumination and fast rocket ascent rate - see 5.8 for details. Theoretical models predict significant diurnal variation of ozone around 60 km, and a direct measurement (lunar zenith angle $< 90^\circ$) would not have sufficient accuracy to compare with daytime values at that level. (De Jonckheere and Miller (1974) described an ozone measurement by that technique where they estimated an error of $\pm$ 60% at 65 Km but they were able to use a moon-pointing Skylark rocket and long (1 second) continuous signal integration to reduce the effect of photon noise). It was therefore decided to perform the nighttime measurement as a lunar occultation experiment.

Such an experiment, because of the long atmospheric path length, is capable of measuring ozone up to 95 km. Night time ozone measurements in the lower thermosphere (eg Hays and Roble (1973); Riegler et al, (1977)), have shown considerable differences, so a new measurement there is of scientific value and interest. The night time payload was thus designed to measure ozone up to 95 km.

The payload to be flown at dawn or dusk was also intended to measure ozone up to 95 km by the occultation method. The remaining two payloads were to give daytime

measurements, the upper limit of which was ~70 km. The lower limit was the lowest height at which the nosecone could be deployed forward without endangering rocket stability (see sect. 3), which was ~ 42 km. This gave the lowest level required of the occultation measurements as well, since all four ozone profiles were to be compared below 70 km.

The required accuracy of the final ozone profiles at 60 km was ± 10–15% for the three solar rounds and ± 20% for the lunar round, with a height resolution of 4 km.

Table 1

Rocket designation	Time of launch, GMT	Radiation Source	Geometry for attenuation
MOP6	Night, 0200	Moon	Occultation at moonset
MOP3	Dawn, 0600	Sun	Occultation at sunrise
MOP5	Morning, 0930	Sun	Solar zenith angle 70 ± 2 deg
MOP7	Afternoon, 1530	Sun	

Note: MOP = Meteorological Office Petrel

2. Criteria for Launch

Since the main reason for the experiment was to investigate the chemistry of mesospheric ozone, it was desirable to keep dynamical influences to a minimum. If the meteorological state of the mesosphere had changed significantly during the course of the experiment the results would have been more difficult to interpret. For this reason, the experiment was best conducted in summer, when the easterly stratospheric circulation blocks planetary wave propagation and the quieter meteorology of the troposphere causes fewer internal gravity waves than in winter.

However, a conflicting criterion also had to be considered. It was mentioned in Sect. 1 that the moon is a dim object in the ultraviolet, difficult to observe from a spinning rocket where long exposure times are not possible. In order to be sure that the payload would function correctly without expensive attitude control mechanisms it was necessary to ensure that the moon was the only object in the sky capable of exciting the sensors. Unfortunately sunlight scattered over the horizon was capable of exciting the sensors when the solar zenith angle was less than 115°; this had been observed in a previous flight. The night time round could only therefore be launched with a solar zenith angle greater than 115°.

The experiment, for logistical and financial reasons, was constrained to take place at South Uist, 57°N, and at this latitude the sun is never very far below the horizon in summer. A further constraint was the requirement (see sect 1) for the night time measurement to be at moonrise or moonset, and as near as possible to full moon because of the problem with lunar brightness.

To obtain the quiet atmospheric conditions together with a sufficiently large solar zenith angle the experiment had to be performed around the time of the autumn equinox (the spring equinox is sometimes marked by great dynamical disturbances in the upper atmosphere). Specific days had to be chosen during this time to give a satisfactory compromise between lunar brightness and solar depression. For logistical reasons it was highly desirable to have two successive days on which the rockets could be launched, since meteorological conditions or a ground failure could prevent the campaign from taking place on the first day. In the event the first choice day was 2nd October 1979 (lunar brightness at moonset 24.3% of full moon, solar zenith angle 122.6°) with the following day as backup (lunar brightness at moonset 41% of full moon, solar zenith angle 115.7°).

The times at which to launch the two occultation rounds had to be chosen carefully. As explained in Appendix C, the 'grazing ray height' is lower than the rocket height by approximately α^2 km, where

$$\alpha \text{ (in degrees)} = \text{source zenith angle} - 90^{\circ}$$

This is the height at which the ozone measurement is effectively made. Since the rocket's nosecone was ejected at 58 km, and ozone measurements were to be made down to $\sim$ 42 km, this required $\alpha^2 \geq 18$ km, or $\alpha \geq 4.2^{\circ}$ at 58 km. This was the limit used for the night time round. Because of the stratospheric water vapour sensor (sect 4) on the dawn round it was decided to use a solar depression angle $\alpha \geq 5.5^{\circ}$ at 60 km ($\alpha^2 \geq 30$ km). In order to ensure that the sensors could observe unattenuated sunlight (or moonlight) for several coning cycles of the rocket, to establish any drift in sensitivity, the grazing ray height at apogee had to be greater than 103 km. Clearly the likely apogee of the rocket had to be known before this requirement could be translated into a launch criterion. Apogee height may be predicted to within 3 km for Petrel rockets, given the payload weight and other relevant data, and some 'fine tuning' is possibly by varying the quadrant elevation at launch. The likely apogees for the two rockets were computed

to be 128 km + for the night time round and 135 km + for the dawn round. From this a maximum permitted value of α at apogee could be computed in each case, and the length of the launch slots determined. These turned out to be just 3 minutes long, but fortunately this did not prove to be a major problem on the day. The two daytime rounds were each launched at solar zenith angle $70^{\circ} \pm 2^{\circ}$; this gave launch slots of 45 minutes in each case.

One further criterion had to be considered before conducting the experiment. The disruption of stratospheric and mesospheric ozone by Polar Cap Absorption (PCA) events is well documented (Weeks et al 1972, Heath et al, 1977). A diurnal variation measurement conducted during such an event would be difficult to interpret, and this possibility had to be guarded against. Forecasts were therefore obtained, on a daily basis for about 3 weeks before the campaign, from the Observatoire de Paris at Meudon, France. These forecasts indicated the probability of a proton event during the next few days, and were used to decide whether to go ahead with the experiment. Fortunately, no PCA event was either forecast or observed near October 2nd, and the experiment took place as planned.

3. The Vehicle

This section is only meant as a brief guide to the Petrel Rocket. Further details may be obtained from the Petrel Users' Handbook (B.A.J. Ltd., Banwell, Weston-super-Mare).

The Petrel I rocket is about 3 m long and 190 mm in diameter. It can carry a payload of ~ 20 kg to ~130 km, with the obvious tradeoff between payload mass and apogee attainable. Consequently, during the design stage the desired apogee had to be used as a constraint on the mass of each payload; indeed a metal block was flown on the daytime rockets to lower the apogee.

For the first 200 ms of flight the rocket is accelerated at ~ 66g by boost motors; after this the main motor accelerates it at ~ 5g for 30s. It is the initial launch shock and the vibration associated with the main motor burning that provide the major mechanical problems of payload design. All payloads are checked for flight suitability by an 'environmental test' (ie vibration) before launch. The rocket is provided with fins canted at 20' to its axis, these cause it to spin at 8 $\pm$ 2Hz, thus helping to stabilise the direction of the axis.

A diagram of the space available for the experiment in the nose of the rocket is shown in fig 3(i). The experiment is bolted onto a bulkhead (the payload platform) through which power and telemetry lines are fed. Power is available from a battery (in the form of a 28V, 17V or stabilised 12V source). The telemetry is composed of a carrier (RF) wave amplitude modulated by a sub carrier which is in turn frequency modulated by the experimental outputs. Twenty-four output channels are sampled sequentially by a motor-driven switch, rotating 80 times a second. One of the channels is subcommutated to give 24 'low-speed' channels, used for housekeeping and telemetry calibration data. The latter consists of accurately known voltages between 0 and 5.4V (the range acceptable to the telemetry) which are used to convert raw flight data back to sensor outputs. After the flight the raw telemetry data is digitised to provide a tape suitable for computer processing.

Although the Petrel rocket, as mentioned above, is spin stabilised, the direction in which it points during flight is not accurately predictable. This depends primarily on the launch elevation angle and the lower level winds. The direction also varies during flight, irregularly under the influence of drag forces up to ~ 65 km, then a free coning motion under gravity with an amplitude of $\sim 5^{\circ}$. Towards 75 km on the descent leg the rocket begins to tumble uncontrollably as it enters the atmosphere, and the useful part of the flight is over. Any optical sensors to observe the sun (or moon) must have fields of view greater than $\sim 60^{\circ}$, large enough to cope with any vagaries in rocket behaviour.

Because of the influence of air drag up to 65 km, the rocket is streamlined with a fibreglass nosecone. In the standard Petrel this nosecone is ejected by a powerful spring at about 60 km, thus exposing the sensors. Such an arrangement was fine for the two occultation rounds, where observations did not need to be made below 60 km, but was clearly unsuitable for the two daytime rounds. A new system was devised for them, which entailed lifting the nosecone a few centimetres, again with a powerful spring, exposing holes in the sleeve (see fig 3(ii)). The rocket launch and safety authorities (AWRE Aldermaston) considered that this system could not safely be deployed below ~ 42 km, and so this was the lowest height at which ozone measurements could be made. A consequence of the lifting nosecone, was, of course, that the optical sections of the payloads had to lie next to the payload platforms.

4. Payloads

The chief objective of each payload was to measure the ozone density, from 45 to 90 km for the occultation rounds and from 40–60 km for the daytime rounds. The main sensors were therefore the filter photometers, which are described in Section 5. In order to cover the necessary height range two photometers sensitive to different wavelengths were needed for the occultation rounds (see 5.2), while only one was needed for the daytime rounds.

Because of the rockets' coning motion the angle between the sun (or moon's) direction and a sensor's axis changed periodically throughout a flight (see sect. 3). This introduced a modulation to the signal caused by the variation of sensitivity with angle of illumination (fig 4.1). In order to remove this modulation during the data analysis an attitude sensor was flown on each payload, to measure the angle of illumination.

The ozone photometers and attitude sensors were the primary instruments to be flown, but there was space available on each payload for secondary experiments. On MOP3 (the dawn round) two further instruments were included; the first was a molecular oxygen sensor to measure the extinction of radiation with wavelength ~ 210 nm (on a similar principle to the ozone photometers). The second instrument was a water vapour sensor, the spare for an experiment flown on a Skylark in 1970 (C.G. deJonckheere, 1975). This instrument was to measure the extinction of infra red radiation at 2.61μ, but it gave no signals during flight and will not therefore be mentioned any further.

On the other three payloads experiments were provided by the UCW Aberystwyth rocket group. Their instrument for the night-time round was a temperature sensor based on the twin hot wire principle, and intended to measure from 65 km to apogee (such measurements were also of interest to ourselves of course). A radio experiment, measuring electron density in the lower ionosphere by the Faraday rotation method, was flown on the two daytime rounds. The choice of a radio experiment was dictated by the fact that the rocket nosecone was not ejected.

As far as possible the payloads were designed on a modular principle, ie one instrument could be removed independently of the others. This was achieved by using two structural side pieces and 'trays' that fitted between them, a design successfully used for many years by UCW. It is advantageous to place the electronics at the bottom of the payloads: the rocket sleeve prohibits the positioning of optical instruments there, the electronics boxes help to stiffen the structure and there is less wiring running up and down the payload. However, this had to be abandoned for the daytime rounds, since the nosecone was only lifted ~ 5 cm and the optical sensors had to be at the bottom. Above the optical section for these rounds, however, the modular approach was retained.

Photographs of the payloads are provided:

- MOP3, dawn payload, fig 4.2;
- MOP5, morning payload, fig 5.6e;
- MOP6, night payload, fig 5.8d.

5. Payload design

5.1 Basic design of Photometers

All the photometers flown on the rockets consisted of an interference filter, defining a narrow spectral pass-band in the ultraviolet, placed in front of a detector. The detector was a vacuum photodiode for the three solar rounds and a photomultiplier for the lunar round.

The spectral pass-band of an interference filter varies with the angle of incidence of incoming radiation; as the angle increases the pass-band moves to shorter wavelength. Data supplied by filter manufacturers show that a pass-band shift of 1 nm occurs when an UV filter is illuminated around 8° off axis. In order to minimise the effect of off-axis illumination and still provide a wide field of view for the sensor a diverging lens was placed in front of the detector/filter combination.

The lens was designed so that angles of incidence at the filter were limited to $\pm 8^{\circ}$ for a $\pm 30^{\circ}$ field of view. A note on the calculation of ray paths through a lens is provided in Appendix D. The attenuation of the beam caused by the lens varies with the angle of incidence, and the design concentrated on means to minimise this effect. This was in order to minimise the influence of rocket coning motion on the flight signals. The final design was a trade-off between uniformity of attenuation and space available on the payload. The lenses were cylindrically concave and made from Spectrosil - B (fused silica). Although computer simulation of ray paths showed that the attenuation changes could be greatly reduced by using lenses of parabolic cross section it was not possible to find a manufacturer for such lenses using fused silica.

The field of view in roll of the solar photometers was about 20°. This meant that a pulse from one during flight would last about 7 ms, assuming a roll rate of 8Hz. This is too short to allow the telemetry to sample the pulse reliably, so each sensor was linked to a trigger diode - a photodiode behind a narrow slit which provided a brief pulse as it swept past the sun. This triggered a monostable, which instructed a sample and hold circuit to hold the output from the sensor at that point. By this means the sensor was always sampled at the same point in roll. Details of the construction of the sensors and trigger diodes for each payload will be given in the following sections.

5.2 Choice of Wavelengths for Ozone Sensors

There are several factors that need to be considered when choosing the peak wavelengths of the photometers. The first is the shape of the Hartley absorption band of ozone, which determines the region of the atmosphere where radiation of a particular wavelength is attenuated. The second is the fine structure of the solar ultraviolet spectrum which is full of peaks and troughs. A sensor whose pass-band coincides with a peak will have its optical bandwidth effectively reduced at no cost to its peak responsivity. A narrow bandwidth is favoured so that the variation of ozone absorption coefficient within the pass-band is kept as small as possible. Thirdly, the availability and cost of suitable filters is an important consideration.

The two occultation rounds were intended to measure ozone from 45 to 90 km. Two sensors were needed to do this, one with its pass-band near the peak of the Hartley band and a second at a wavelength where the absorption is much lower. Since the first observed the region from 60-95 km, the second was required to observe the region 45-60 km. This was best achieved by a wavelength in the

range 290–295 nm which is completely attenuated at 40 km and gives a profile from 45 to 70 km.

The choice of peak wavelength within the broad ranges described above depends onthe solar spectrum. A glance at the spectrum near the peak of the ozone absorption band shows a very pronounced jump near 264 nm, and a peak near 266 nm. A sensor with its peak wavelength at 266 nm would therefore have the shape of its spectral pass-band improved by the solar spectrum. A sensor with peak wavelength 290 nm would benefit in the same way, and this wavelength was chosen for the second sensor.

In the case of the daytime rounds the nosecone was to be lifted at ~40 km (sect. 3). Solar radiation at 266 nm is attenuated in the region 45–65 km with a 70° zenith angle, and therefore one sensor at this wavelength was all that needed to be flown.

5.3 Choice of Optical Components for the ozone sensors

The shape of the solar spectrum curve has an important bearing on the choice of filters and detectors. The steep rise in irradiance from UV to visible wavelengths means that the pass-band of a sensor must have a sharp cut off at the long wavelength side, so that the signal has no component from outside the desired pass-band. This requirement is met by 3-period interference filters, which have a very sharply defined pass-band. Unfortunately it is a common property of ultraviolet interference filters that they have a broad secondary peak in the visible part of the spectrum. Combined with the greater solar irradiance at those wavelengths this could give rise to significant unwanted signal. To counter this possibility detectors of the 'solar blind' variety were used. These had caesium telluride cathodes with very little response beyond 320 nm.

In choosing the interference filters a balance had to be struck between three factors: the requirement for a narrow bandwidth to minimise the variation of ozone absorption coefficient in the pass-band, the requirement for a wide bandwidth and high peak transmission to get large signals (especially for the moon round), and the cost and availability of filters. A survey of the market showed that 3-period filters with < 10 nm half power bandwidth and $> 15\%$ peak transmission were available at moderate cost, at 265 nm from Ditric Optics Inc., USA, and at 290 nm from Corion Inc., also USA, and these were chosen as a good practical solution to our requirements. As the accompanying diagrams show; when detector filter and solar spectrum were taken into account, the effective half power bandwidths were significantly less than 10 nm.

5.4 Choice of Optical Components for the Oxygen sensor

Molecular oxygen absorbs at wavelengths shorter than 242 nm, and this provides a means for measuring air density by the occultation technique. However, the absorption cross-section of oxygen is not a smooth function of wavelength, as with ozone. Its spectrum may be divided into three sections:

(i) The Schumann-Runge continuum, 175–125 nm, corresponding to

$$O_2(^3\Sigma_u^-) \longrightarrow O(^3P) + O(^1D)$$

excited oxygen molecule

Absorption is very strong and radiation in this wavelength band is absorbed above 80 km.

(ii) The Schumann-Runge band system, 175-204 nm, corresponding to

$$O_2(^3\Sigma_g^-) \rightarrow O_2(^3\Sigma_u^-)$$

ground state — excited state, caused by a change in the symmetry of the wavefunction

The absorption cross-section has a very complex dependence on wavelength - it can vary by orders of magnitude within fractions of a nanometre, (Ackerman 1972). The absorption is generally strong, and radiation in this region is chiefly absorbed above about 60 km in the mesosphere.

(iii) The Herzberg continuum 204-242 nm, corresponding to

$$O_2(^3\Sigma_g^-) \rightarrow 2\ O(^3P)$$

$$\text{via}\quad O_2(^3\Sigma_g^-) \rightarrow O_2(^3\Sigma_u^+)$$

which is a forbidden transition. The absorption is thus weak and it varies smoothly with wavelength (Shardanand and Prasad Rao, 1977; Ogawa, 1971). Radiation in the region 205-220 nm can penetrate to the lower stratosphere, and is the main source of oxygen atoms below 70 km.

The uncertainty in values of oxygen absorption cross sections in the Schumann-Runge bands, and the very sharp variations with wavelength, dictated that radiation below 204 nm needed to be outside the passband of the sensor. The absorption cross section beyond 204 nm is slowly varying and does not further inhibit the choice of passband wavelengths. However, the ozone absorption coefficient is at a minimum at 202 nm, and rises steeply towards longer wavelengths (Inn and Tanaka, 1959). In the region 215 nm onwards attenuation due to ozone is greater than that due to molecular oxygen for grazing ray heights below 60 km. It was therefore desirable to keep the passband to as short a wavelength as possible, consistent with the criterion imposed by the Schumann-Runge bands.

As with the ozone sensors the oxygen sensor must have a sharply defined passband and no 'visible leakage'; more so in fact as the solar intensity is that much lower around 210 nm. Thus a three-period filter and 'solar blind' detector must be used, as before. The solar spectrum (COSPAR, 1978) (fig 5.4b) shows a sharp jump in intensity from 207.5 nm to 209.5 nm, with a small peak near 212 nm. The optimum peak wavelength for the sensor was chosen to be 210 nm with a half power bandwidth of < 8 nm. This would put the passband beyond 204 nm, keep it relatively free from the influence of ozone absorption, and avoid having it badly distorted by the solar spectrum (which would be the case with wavelengths < 209 nm).

Unfortunately, the availability of narrowband filters centred at 210 nm is strictly limited. The requirement for a half power bandwidth of 8 nm, a sharp cut off on both sides of the passband, and a peak wavelength of 210 ± 1 nm meant that a custom built filter had to be used. The manufacturers, Infrared Industries Inc, USA, provided a filter with an excellent spectral shape but with its peak transmissivity at 211.5 nm. This made the sensor a little more susceptible to the influence of ozone absorption than was desirable. Nevertheless, it was still capable of measuring oxygen concentrations from 57 to 85 km.

5.5 Design of dawn round

a) Design of MOP3 sensors

The mechanical design of these sensors is illustrated by the diagram fig 5.5a(i). In order to protect the photocell (Hamamatsu type R765) adequately against launch it was mounted vertically. This meant that a mirror was necessary to allow the sensor to look out sideways. This configuration was also convenient for mounting the sensor in the payload.

For spectral calibration of the sensors currents as small as 10^{-14}A had to be measured. Since the tube cathode was held at -90V this required very good insulation between the anode and cathode leads, which were only 2 mm apart where they entered the tube. It was found by experiment that the leakage current was kept to a minimum when the back of the tube was exposed to air, so a perspex ring and rubber gasket were used to support it during flight. Rubber "O" rings were used to locate the photocell centrally in its housing, and the gap between metal and diode was filled with silicone rubber to protect the tube from lateral vibrations. 'Superglue' was used to attach rubber rings and gaskets to the perspex ring.

The aperture above the tube was 8 mm in diameter and the filter was mounted directly above this. A thermistor was mounted in the housing next to the filter; this was intended only to give a guide to temperature changes during flight to facilitate explanation of any drifts in sensor response. No attempt was made to calibrate the sensor at different temperatures.

The rubber gaskets 'A' were intended to allow the sensor to be flushed with dry nitrogen and sealed before flight. This was done to avoid any condensation of water on the optical parts due to the rocket being left out in the cold all night before launch.

(b) Trigger diodes (including day and night rounds)

As mentioned in section 5.1, the trigger diodes were optical devices with a very narrow field of view in roll, which gave a pulse each rotation to hold the sensor signal at normal incidence for sampling by the telemetry. Near normal incidence in roll the sensitivity of the main sensors was constant over about $.5^{\circ}$; the triggering device therefore had to be accurate to $\pm.25^{\circ}$ in roll angle.

The trigger diodes for all three sun rounds were optically identical. Two slits, 2mm wide and 8 mm apart, defined a field of view of 3°, and light was detected with a Siemens BPX63 photodiode. To achieve the required resolution in roll the electronics triggered off the leading edge of the optical pulse.

The electronic circuit was at its simplest for MOP3, consisting of a current to voltage converter and Schmitt trigger circuit to provide a pulse for a monostable. The monostable supplied the sample and hold circuits with a signal to hold the sensor outputs for about 50 ms (see fig 5.5b(i)).

This circuit was unfortunately too bulky for the daytime rounds, where space was more at a premium. Here, an alternative circuit was devised, using two NOR gates to trigger (as a Schmitt trigger), hold and invert the pulse to the sample and hold circuit (which required a negative going hold signal) - see fig 5.5b(ii).

The night time trigger diode was optically identical to the lunar attitude sensors' vertical diode - a BPX63 situated .25 mm behind a 1 mm wide slit. The increase in size was necessary in order to use the full active area of the

diode and preserve the narrow field of view. The current for the moon was much less than for the sun, so the bandwidth of the current-voltage converter had to be limited to preserve the stability of the amplifier. To allow the device to trigger on a low threshold voltage from the C-V converter, a specific comparator circuit replaced the Schmitt trigger. The circuit was otherwise the same as for the MOP3 trigger diodes.

Since the pulses from the night-time sensors were smoothed (see sect. 5.8) the peak of the flight pulse did not occur at normal incidence (see appx A, fig A). The slit on the trigger diode was adjusted so that the device triggered at the peak with a spin rate of 8Hz.

5.6 Design of Daytime Rounds

It has been mentioned in Sect. 2 that previous Met Office experience with solar occultation experiments has shown that the sensitivity of sensors may drift during flight. No physical explanation was offered for this (Miller and Ryder 1973), and an empirical exponential model was fitted to the drift during the data reduction. Since the corrections were greatest during the ascent leg this introduced greater uncertainties to the ascent ozone profile than to the descent profile.

With the daytime rounds, however, all the data was contained in the first few seconds after nose-cone release. A drift of the kind observed previously could therefore seriously impair the accuracy of the ozone measurements. Consequently an effort was made during the design to enable the direct evaluation of any drift.

Two possible causes were considered - changes in detector sensitivity and contamination of the optics, the first being thought more likely than the second. However, the space available on the payload allowed a monitoring of both possibilities. Ideally one would have measured the sensitivity of the instrument around the peak of the passband throughout the flight. This required a source of radiation more stable at those wavelengths than the detecting system. Unfortunately, no such source could be mounted on the rocket. Therefore the sun had to be used as the stable source.

During the full-sun part of the flight the drift of the sensor can be readily evaluated (with due consideration of coning motion). To find the drift during the attenuation part it is possible to monitor a wavelength band which is only slightly attenuated at 40 km. The behaviour of the sensor in full sun at both the main and monitor wavelengths can be compared, and if there is good correlation the monitor channel can be used to extrapolate the drift on the main channel back to the time of nosecone release. One would then say that the drift was due to the detector. In practice the monitor channel was constructed by using a piece of Corning 5840 glass in the optical section. This, when combined with the detector and other optics, gave a wavelength response as shown in fig 5.6b and a full sun current similar in magnitude to the 265 nm channel.

To check for drift due to contamination of the front lens a separate system of detectors was used. Such drift would not be sharply dependent on the wavelength, so the beam was monitored by silicon photodiodes (Siemens BPX63) whose response was mainly in the red and near infra-red part of the spectrum.

The main mechanical constraint to the design of the daytime round was the lifting nosecone. This meant that the optical section had to be right at the bottom of the payload, and any modular approach to design of the sensors had to be abandoned. The optical section was mounted directly on the experimental baseplate, and thus was part of the payload structure. Any faults developing in this section after

assembly necessitated stripping down the payload, but fortunately such problems were not as great as had been feared during the design phase.

Diagrams of the optical section are shown in figs. 5.6a and 5.6c. Each channel consisted of a diverging lens and 24° prism, a silica plate, a filter (or glass) and the beam-splitter assembly. It is not possible to predict with any accuracy the angle between the rocket axis and the vertical during flight, since this depends on the meteorological conditions at launch (see sect 3). One can, however, consider it to be in the range 0° - 20°. Since both daytime payloads were to be identical, and were to be launched at solar zenith angle 70° - 75° during morning and afternoon, the sensors had to have a field of view from -5° to +40° in pitch (positive angles looking up). Consequently the lenses were inclined to the rocket axis and prisms used to deflect the optical axis of the sensor. The choice of 12° deflection was dictated by mechanical constraints; a larger angle could not have been accommodated in the channel.

The silica plates acted as simple beamsplitters to direct some light onto the monitor diodes. Pieces of ground glass were placed before the diodes to reduce the variation of their response with solar attitude angle. Apart from the shiny dural 'mirror' in front of the monitor diodes all the metalwork in the channel was black anodised with matt finish to reduce reflections.

Directly before the central main beamsplitter the filter was mounted - in this case a Ditric Optics 1" square filter nominally peaking at 265 nm. The beamsplitter had a dielectric coating with a reflectivity of ~ 22% at 265 nm. The 'indirect reflectivity' (ie the fraction of the monitor beam transmitted towards the detector via the full aluminised mirror) was about 10% at 330 nm, but varied with wavelength as shown in Fig 5.6d.

The detector (HTV R765 photodiode) was mounted vertically in the main amplifier box. This part of the payload was of modular construction, and the amplifier and detector could easily be removed from the payload. The base of the box had a circular groove which locked into a baffle ring on the optics cover plate, to locate the detector correctly and blank out any stray light. The rubber gasket under the cover plate served two purposes: firstly to make the optics less susceptible to stray light and secondly to enable the channel to be flushed with dry nitrogen before launch to eliminate any condensation on the optical surfaces.

Trigger diodes were used on these payloads as previously described, and the electronics for both them and the attitude sensor was contained next to the main optics. The attitude sensor was of the inclined diode type described in Sect. 5.9.

5.7 - Electronics

This section describes the circuitry for the signal amplifiers, power supplies and monitors on the four payloads. The electronics associated with the trigger diodes and attitude sensors are described with those devices.

The signals from the optical sensors on each payload were treated in essentially the same way; current was converted to voltage in a preamplifier, this voltage was fed to a sample and hold module (if desired) and the output presented to telemetry by a buffer. Figs 5.7(i) and (ii) show two such circuits; the first one was used for the MOP6 sensors and the MOP5 and 7 monitor diodes while the second (incorporating voltage gain in the preamplifier) was used for the MOP3 sensors and the MOP5 and 7 main sensors. From optical calibration of the sensors an estimate of the maximum possible flight current was obtained (using known solar or lunar spectrum data), and the preamplifiers were set up to give about 4V output with this current. Since the telemetry accepted signals up to 5.6V this gave a generous margin of error on the estimate of maximum current.

Although similar in principle there were differences in practice between the four payloads. On MOP6 there were three outputs to telemetry for each sensor - a running output and two held outputs. The reasons for choosing a running and a held output are described in the next section, while the reason for having two held outputs was basically a logistical one. The experiment could be conducted on either of two successive days, with the moon almost twice as bright on the second day as on the first. To avoid having to strip down the rocket if the first day was missed it was clearly desirable to have the sensor outputs in a form suitable for either day. This was done by providing gain in the buffer sections so that one gave good signals on the first day and the other on the second day. The running output was scaled for the second day since it was only intended as a back-up system. Its signals were therefore rather low on the first day.

The main sensor amplifier for the daytime rounds was also non-standard because of the two optical channels serving the same photodiode. Trigger diodes located next to the two channels and coaxial with them allowed the relevant signal to be chosen for each telemetry channel, and the output from the two sample and hold circuits was again scaled for telemetry by the buffers.

The rocket battery provided voltage lines at 28V, 17V and 12V, which had to be modified for use by the experiment. The sample and hold modules (Burr Brown SHC80KP) needed $\pm$15V and 0V, and these levels were provided by a special DC/DC converter (Hybrid Systems D15-100/12) working off the 12V supply. All the operational amplifiers used the + 15V rail, and the logic circuitry for the lunar attitude sensor derived +5V from this rail via a regulator.

The photomultipliers on MOP6 needed 1kv across the dynode chain to operate, so an EHT power supply was built for each one. Separate power supplies made it possible to set up the amplifiers correctly after calibration, since the photomultiplier gain was extremely sensitive to EHT. For the same reason, the power supply had to be very stable with variations in load and temperature. The heart of the unit was a Brandenburg 481N EHT modules, which was incorporated in a control loop. The loop maintained the desired output by comparison with a reference voltage; this was done by a Texas UA723CN circuit (see 5.7(iii)).

A similar circuit was used to provide the -90V required on the cathodes of the photodiodes, but using a multivibrator and transformer instead of the Brandenburg unit. One unit was sufficient for each payload since the photodiodes used (HTVR765) were not very sensitive to HT variation.

Each electronics box was of a standard type except for the daytime round amplifier boxes, which contained the photodiode mounted vertically in the centre. A thermistor was provided in each amplifier box, and used in the temperature calibrations of the amplifiers. These thermistors also provided outputs (by a potential divider and buffer) for low speed telemetry channels, to monitor the temperature in the amplifier box during flight. Similar outputs were provided for the thermistors mounted in the MOP3 sensors, to aid in investigating sensitivity drifts in flight. Low speed channels were also allocated to monitors on the $\pm$15V lines and -90 or EHT lines (whichever was applicable). These outputs were most useful during ground testing of equipment, though they could also show up power supply faults during flight.

5.8 Night time Ozone sensors

The occultation technique used by both the night time and dawn rounds made the optical requirements of their sensors very similar. The lunar spectrum is not sufficiently different from the solar spectrum to alter the choice of wavelengths, and the considerations given to the lens were still applicable.

The full moon, however, is a million times less bright in the UV than the sun, and, as explained in sect. 2, the experiment had to take place when the lunar brightness was 24% of full moon. The lunar intensity at 270 nm was therefore $\sim 10^{-7}$ $Wm^{-2}nm^{-1}$, and this necessitated using a photomultiplier as the detector. Some of the characteristics of these detectors are described in Appendix A.

Given a field of view in roll of $\sim 30^{\circ}$ (see fig 5.8a) and an expected rocket spin rate of 8Hz $\pm$ 2Hz the pulse rise time could be as small as 4ms. To estimate the expected cathode current at normal incidence with no ozone attenuation the following data is needed:

Cathode area = 3×10^{-4} m^2 (ϕ = 20 mm)
filter bandwidth = 10 nm
filter peak transmission = 20% at 270 nm
attenuation due to lens = 0.2
quantum efficiency of photocathode = 10%
lunar irradiance = 10^{-7} $Wm^{-2}nm^{-1}$

This gives J_o (electrons per second from photocathode) = 1.6×10^6

Appendix A(d) gives a formula for the signal to noise ratio to be expected for a photomultiplier and R.C amplifier system. Fig (i) of that appendix shows how the signal to noise ratio varies through the pulse from a typical sensor - this is simply due to storage of charge on the capacitor. The values depend, of course, on the amplifier time constant, as shown in fig 5.8b.

Unfortunately this time constant could not be chosen arbitrarily. Fig 5.8b shows that the longer it was the better the signal to noise ratio of the system. But a long time constant also modifies the shape of a pulse, as shown in 5.8a. The derivation of curve (b) is given in Appendix B, where it is also shown that the area beneath the curve is independent of the time constant. Modification of the pulse shape would thus not be a problem if we were sure that the moon was the only source in the sky capable of exciting the sensor. Unfortunately this was not so: a similar sensor flown in September 1978 showed considerable background signal, modulated with roll angle and varying with rocket height. This is thought to have been due to stray sunlight in the near UV ($>$ 310 nm) which was scattered over the horizon. Since this might also happen with MOP6 the sensor had to be capable of resolving the background illumination near to the pulse - otherwise photons not from the moon could contaminate the signal. It was felt that a time constant of $\sim$3 ms was the longest we could use, since background changes of $\sim$10% signal pulse height were seen over $\sim 35^{\circ}$ of roll with the previous sensor.

A photon counting system would therefore have improved the signal to noise ratio; it is the best possible from the point of view of photon noise and it also allows dark current to be discriminated against (Appendix A(b)). Such a system also has its limitations, however. An estimate of the background illumination was still needed, and this would have meant counting photons in several 'bins' of roll angles. Such a system would have been physically bulky, complex and difficult to calibrate. The possibility of pulse bunching also had to be considered (Appendix A(e)) - with $J_o = 1.6 \times 10^6$ electrons s^{-1} and a pulse width of 50 ns this would introduce an undesirable 8% nonlinearity between photon arrival rate and signal output.

However, the most important reason for rejecting a photon counting system was the tube itself. The primary criterion in its selection was its ability to survive the launch shock of 66g, which severely limited the choice available. Adding to this the requirement for a solar blind tube (very important in view of the need to cut down the background signal as much as possible) and the need for a reasonable price pointed unequivocably to the Hamamastu R431S, as the only practical choice.

This tube was not designed for photon counting (Appx A(b)) and it could not therefore be assumed that the discriminator could be set to reject dark pulses and count photon pulses. In any case, with the R431s and the currents we wished to measure, the dark current was ~ .1% of signal and could easily be ignored as part of the background illumination.

We therefore decided to proceed with an analogue system, with a time constant of 3.3 ms. An effort was made to procure tubes with higher quantum efficiencies than average and filters with higher peak transmissions and better rejection of the near U.V. than average. The filter manufacturers (Ditric Optics Inc). were able to do this, but HTV were not able to improve the quantum efficiency of their tubes beyond about 8% at 270 nm.

The decision about whether to fly a trigger diode was a finely balanced one. The trigger diode allows one sample of the pulse at the same point in roll every time. However, because these pulses had been broadened by the amplifiers, and because there were more available telemetry channels on MOP6 than on the other payloads, it was possible to sample each pulse several times. The roll angle of each sample could be computed from the roll sensor output (see Thesis for details). This technique was capable of increasing the signal to noise ratio to nearer the value possible with a photon counting system, but was inherently more complicated and prone to error. In the end a trigger diode was flown, but the sensors' outputs were also continuously sampled to give an estimate of the background illumination and its variation with roll angle. Despite the fact that the trigger diode was very similar to the two diodes used in the MOP6 attitude sensor (which worked perfectly) the trigger diode malfunctioned (triggered erratically) during flight so the continuous sampling record had to be used in the data processing.

The mechanical design of the sensors was straightforward: the optical section being the same as for the MOP3 (dawn) sensors. A cross-section diagram is shown in fig 5.8c. The photomultiplier was encased in silicone rubber to give it some protection against launch, and a mumetal shield was wrapped around the inside of the housing to protect the tube from strong magnetic fields during vibration testing. The inside of the sensor was filled with dry nitrogen before flight to avoid any condensation problems. The EHT supply of ~ 1 kV was supplied by an electronics package at the back of the sensor (see sect 5.7).

5.9 Solar Attitude Sensors

Paramount in the design of the solar attitude sensors was the need for compactness, particularly for the daytime rounds where the optical section was very congested, and space for electronics also at a premium. The solution adopted relied on the angular response of the Siemens BPX63 photodiode, and consisted of two diodes mounted at an angle to each other thus:

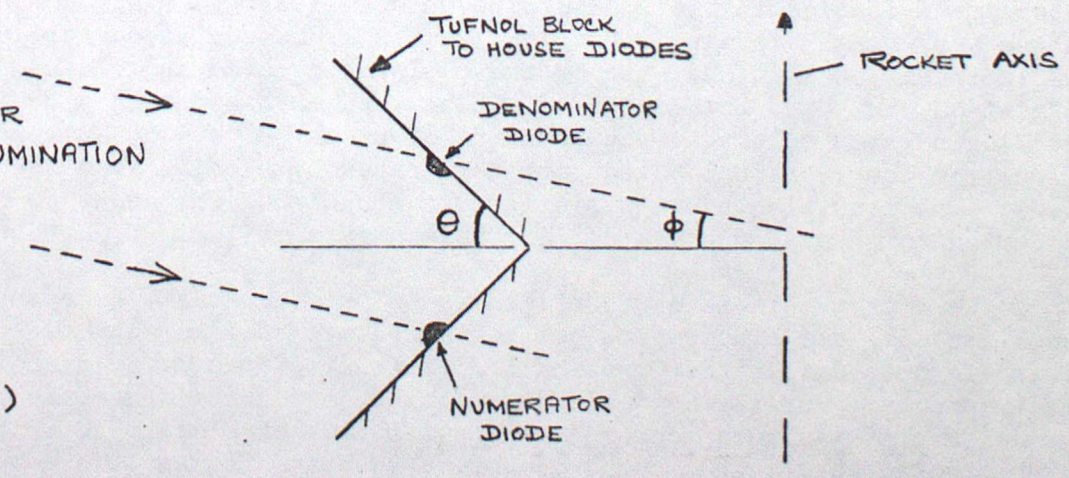

FIG 5.9(i)

As the angle ϕ (the solar attitude angle) varied, the outputs of the two diodes also varied. By taking the ratio of the two outputs a quantity directly related to ϕ was obtained.

The electronic circuit therefore had a current to voltage converter for each diode, the outputs of which were taken to an analogue divider module (Burr - Brown 4291H). This module provided a voltage proportional to the ratio of the inputs, which was taken to a sample and hold module so that the signal could be held at normal incidence in roll for telemetry sampling. A buffer amplifier completed the circuit (see fig. 5.9 (ii)).

The output of this device was not a linear function of ϕ (a typical response is shown in fig. 5.9 (iii)) - a problem which could be alleviated by keeping θ small. Unfortunately this restricted the field of view of the device, and a value of $\theta = 60^{\circ}$ was adopted to ensure an adequate range of ϕ.

The attitude sensor for MOP3 was a self-contained unit, with its own trigger diode and circuitry (Fig 5.9(iv)). On MOP5 and 7 the sensor used the front trigger diode and shared the circuit boards next to the baseplate with both trigger diodes.

It is very difficult to assess the absolute accuracy of this device. Conversion of sensor flight outputs to angles rested on a laboratory calibration (see thesis) with different preamplifier gains and under static conditions. During flight the relationship of fig. 5.9 (iii) (for instance) might not have been strictly true due to such factors as the diode not quite triggering at normal incidence. Nevertheless, we believe the absolute accuracy to be within a degree, and the reproducibility of the output with ϕ to be much better than a degree. Since the latter quality was the one actually needed for the data-processing this device proved adequate for its purpose.

5.10 Lunar Attitude Sensor

Because moonlight is so much dimmer than sunlight the diode currents to be expected in an attitude sensor of the solar type would have been far too small to ratio accurately. An alternative system was devised, a photograph of which is attached (Fig 5.10).

The system comprised of two Siemens BPX63 diodes, one placed behind a vertical slit and the other behind a diagonal slit. Each diode was illuminated briefly in turn as the rocket spun, giving a current pulse to the electronics. The time delay between the two pulses varied with the lunar attitude angle in a manner described in Appendix E.

After amplification in the rear of the sensor block (to minimise interference to the very small diode currents) the pulses from each diode were taken to an electronics box at the base of the payload, squared and cleaned with a Schmitt trigger. The box contained a clock and an 8-bit binary counter, together with logic gates such that the counting of clock pulses was initiated by a pulse from the 'vertical' diode and terminated by a pulse from the 'diagonal' diode. The resulting count was held by a monostable for about 50 ms and converted to an analogue voltage for telemetry sampling.

Since the rocket spin rate was needed to calculate the attitude angle from the sensor output, the electronics box contained a system to measure it accurately. Alternate pulses from the 'vertical' diode started and stopped another 8-bit binary counter, running off a faster clock than the attitude sensor. Since the delay time was much longer, the counter completed about 20 ramps before being stopped (the output being presented to telemetry as before). The resulting ambiguity in spin period was resolved by using main sensor pulses to give a rough

estimate, which was refined with the spin sensor output.

The precision with which the attitude angles could be measured was limited by the resolution of the telemetry, about $\pm$ 20 mV for one pulse, corresponding to about 0.2°. The absolute accuracy of the device depended on the accurate measurement of γ_c (see Appendix E), the angular separation of the two slits, and this introduced an uncertainty of $\pm.5^{\circ}$. Relative accuracy, however, was much better than the $.2^{\circ}$ limit imposed by the telemetry precision. The spin sensor enabled a determination of the spin period correct to 30 μs (.02%).

6. Acknowledgements

We are grateful to Mr L France and Mr G Roberts at U.C.W, Aberystwyth, for their help in collaborating on the payload design, and to Mr Roberts for building the night time payload structure. The mechanical construction of the sensors and the other payloads was undertaken by Mr C Gazzard and his staff in the Met O 16 London Road Workshops, whom we warmly thank for their cooperation at all times and their many useful suggestions.

Thanks are also due to Mr D E Miller, Mr G P Carruthers and Mr C G De Jonckheere, all of whom contributed suggestions on the design and construction of the payloads.

The help of the sounding rocket section at AWRE is also acknowledged in the vibrational testing of the payloads, and for advice on payload integration.

References

D E Miller and P Ryder (1973) Planet Space Sci. 21 963-970.

C G De Jonckheere and D E Miller (1974). Planet Space Sci. 22 497-499.

G Vaughan (1981) Submitted to Nature.

P B Hays and R G Roble (1973) Planet Space Sci. 21 273-279.

G R Riegler et al. (1977) Geophys. Res. Lett. 4 145-148.

L H Weeks et al (1972) J. Atmos. Sci. 29 1138-1142.

D F Heath et al (1977) Science 197 886-889

C G De Jonckheere (1975) Q.J.Roy.Met.Soc 101 217-226.

A L Broadfoot (1972) Astrophys. J. 173 681-689.

E.C.Y. Inn and Y. Tanaka (1959) Advances in Chemistry No 21, P.263. American Chemical Society, Washington.

Shardanand and Prasad Rao (1977) J Q S R T 17 433-439

M Ogawa (1971) J. Chem Phys 54 2550-2556.

M Ackerman (1972) Ann. Geophys. 28 79-83.

ECY Inn & Y. Tanaka (1953) J.O.S.A. 43 870-873.

COSPAR (1978) Techniques Manual No 7. ed. J P Delaboudiniere et al.

P. C. Simon (1975) Bull. Acad. Sci. Roy. Belgique, Cl. Sci, 61 p.399.

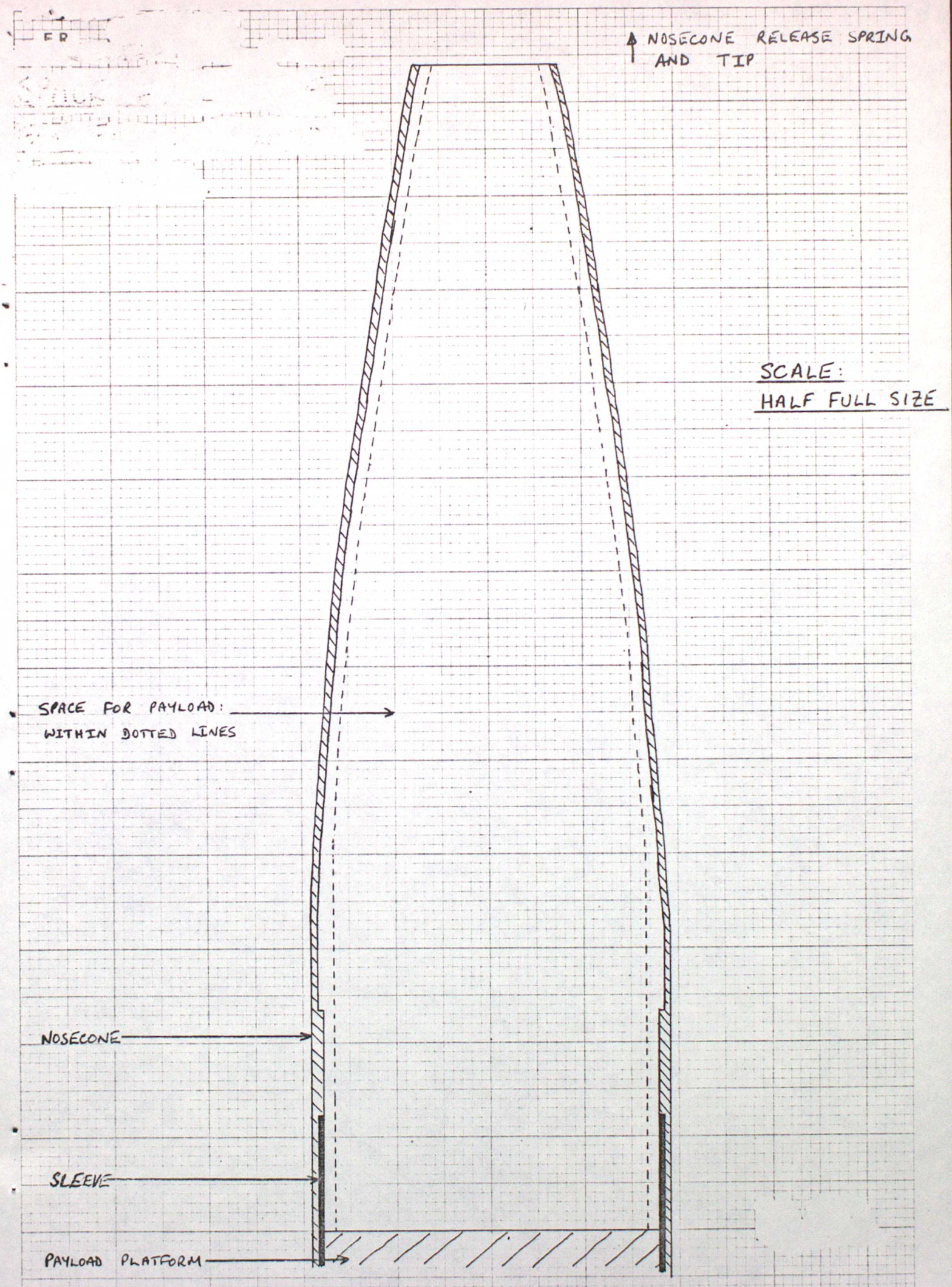

FIG 3 (i). SPACE AVAILABLE FOR PAYLOAD INSIDE NOSECONE

E.R.

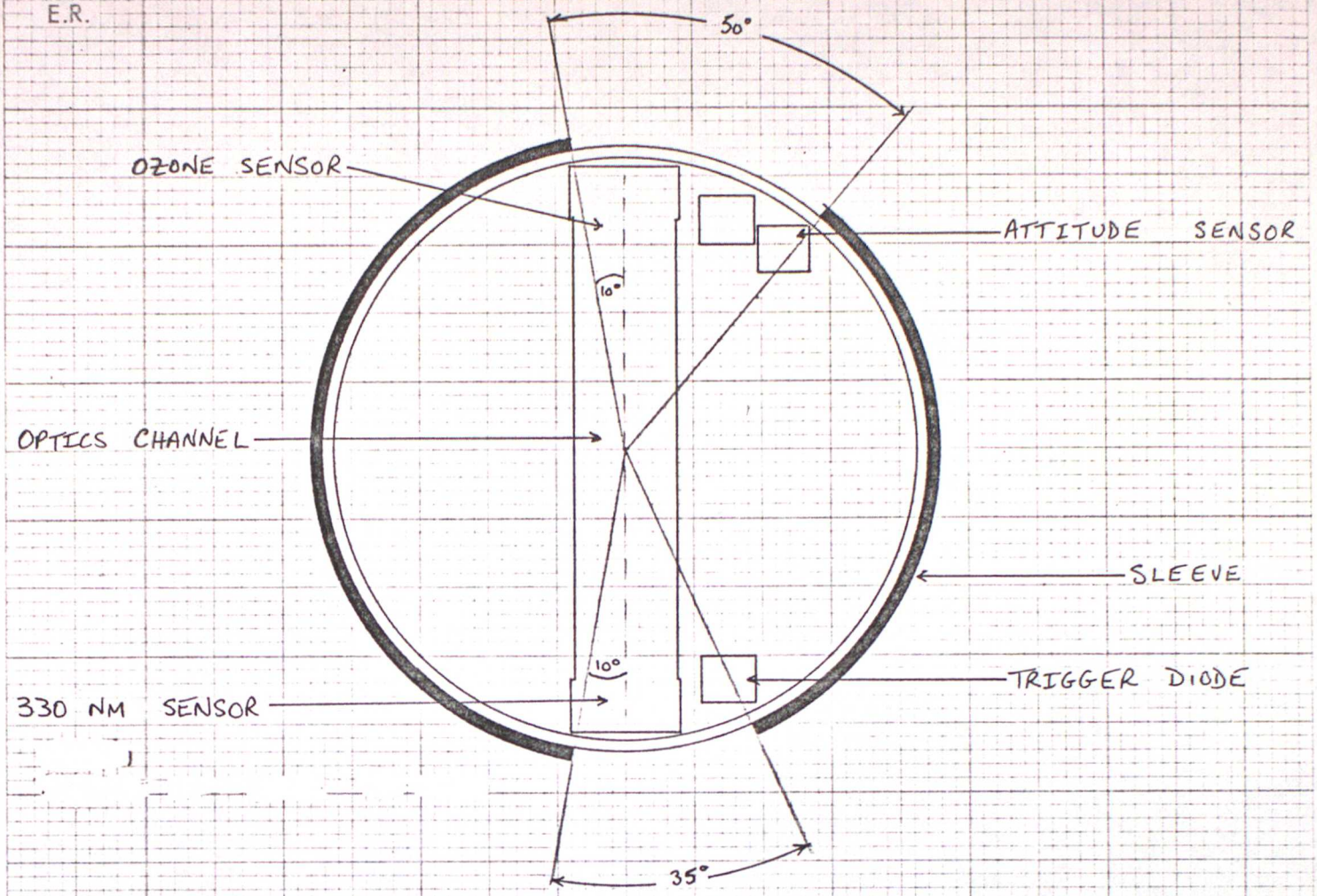

FIG 3(ii) : POSITION OF CUTOUTS IN SLEEVE FOR DAYTIME ROUNDS

E.R. VARIATION OF SENSITIVITY WITH ANGLE OF ILLUMINATION,

MOP6 265 nm SENSOR.

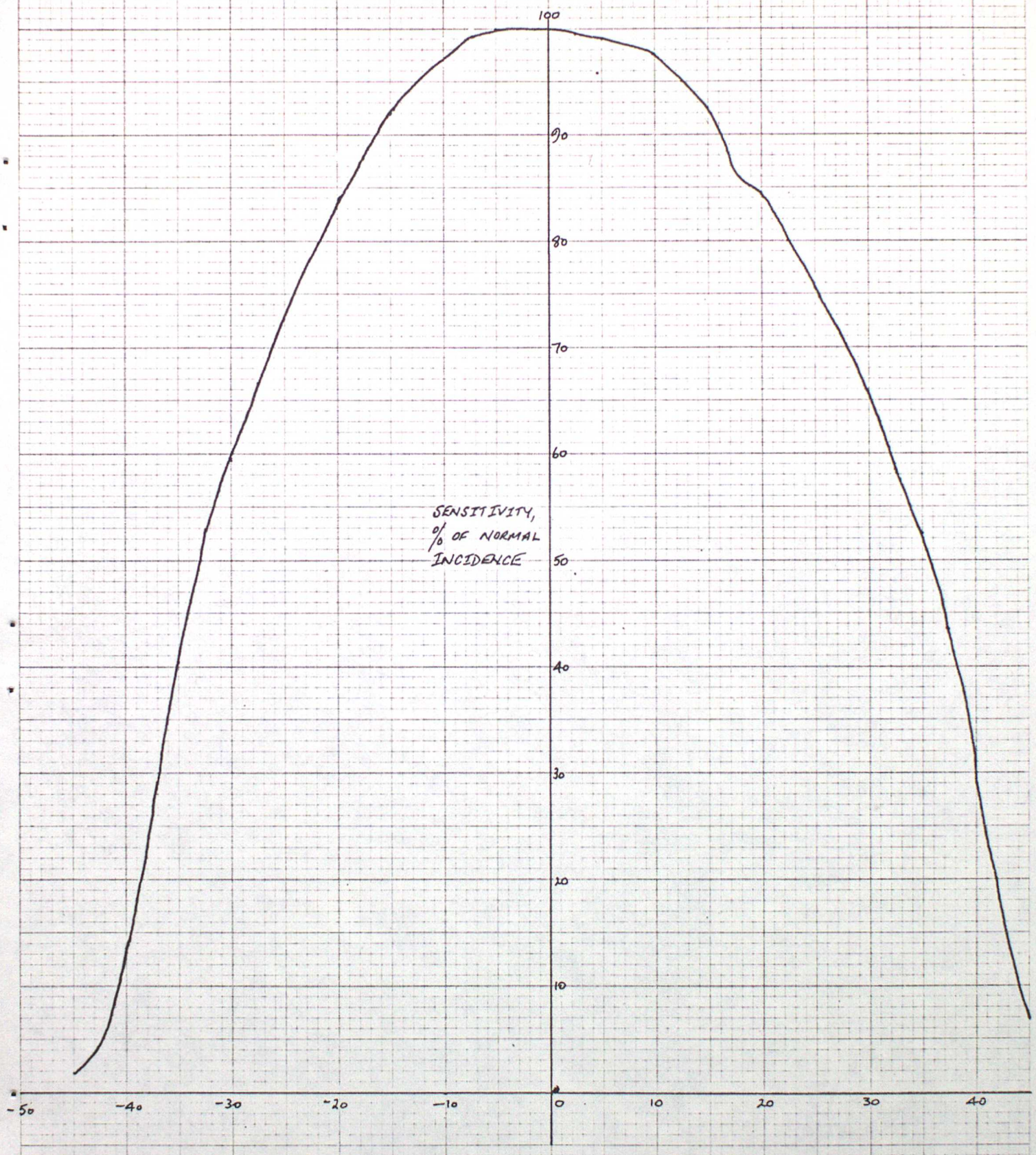

FIG 4.1

FIG. 4.2

MOP3 (DAWN) PAYLOAD

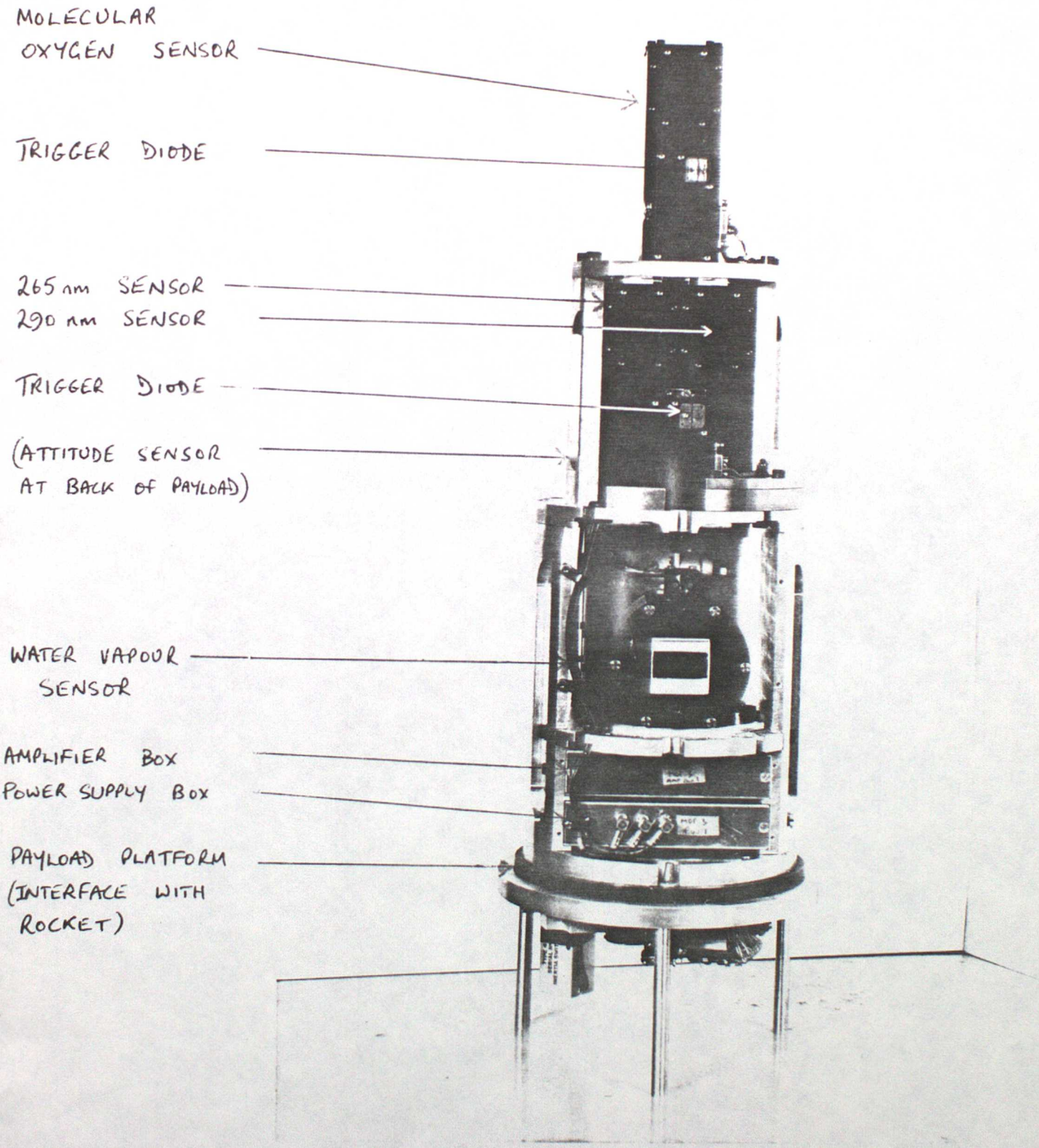

FIG 5.2a

SOLAR IRRADIANCE 230-320nm

AFTER A. LYLE BROADFOOT (1972)

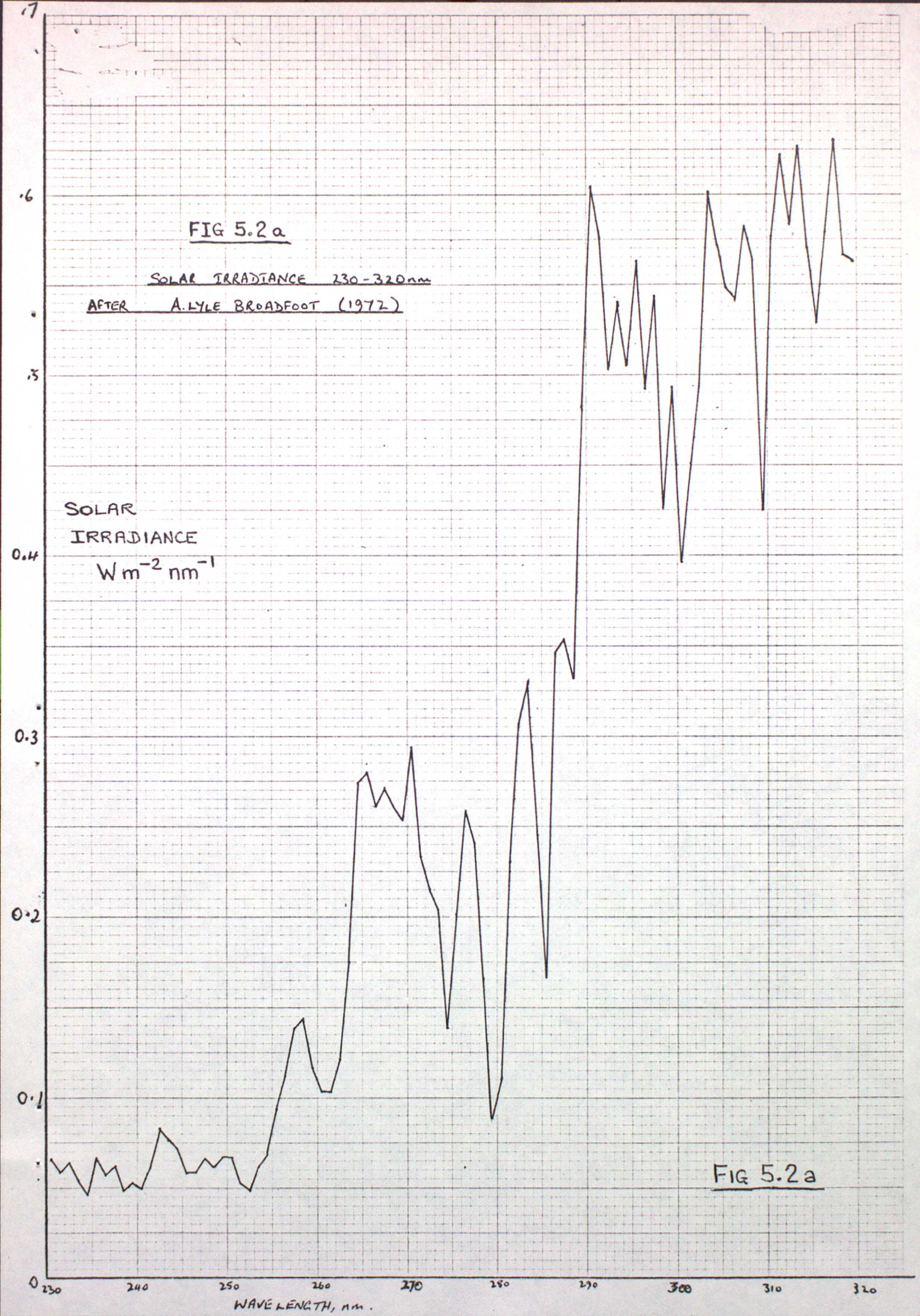

FIG 5.2a

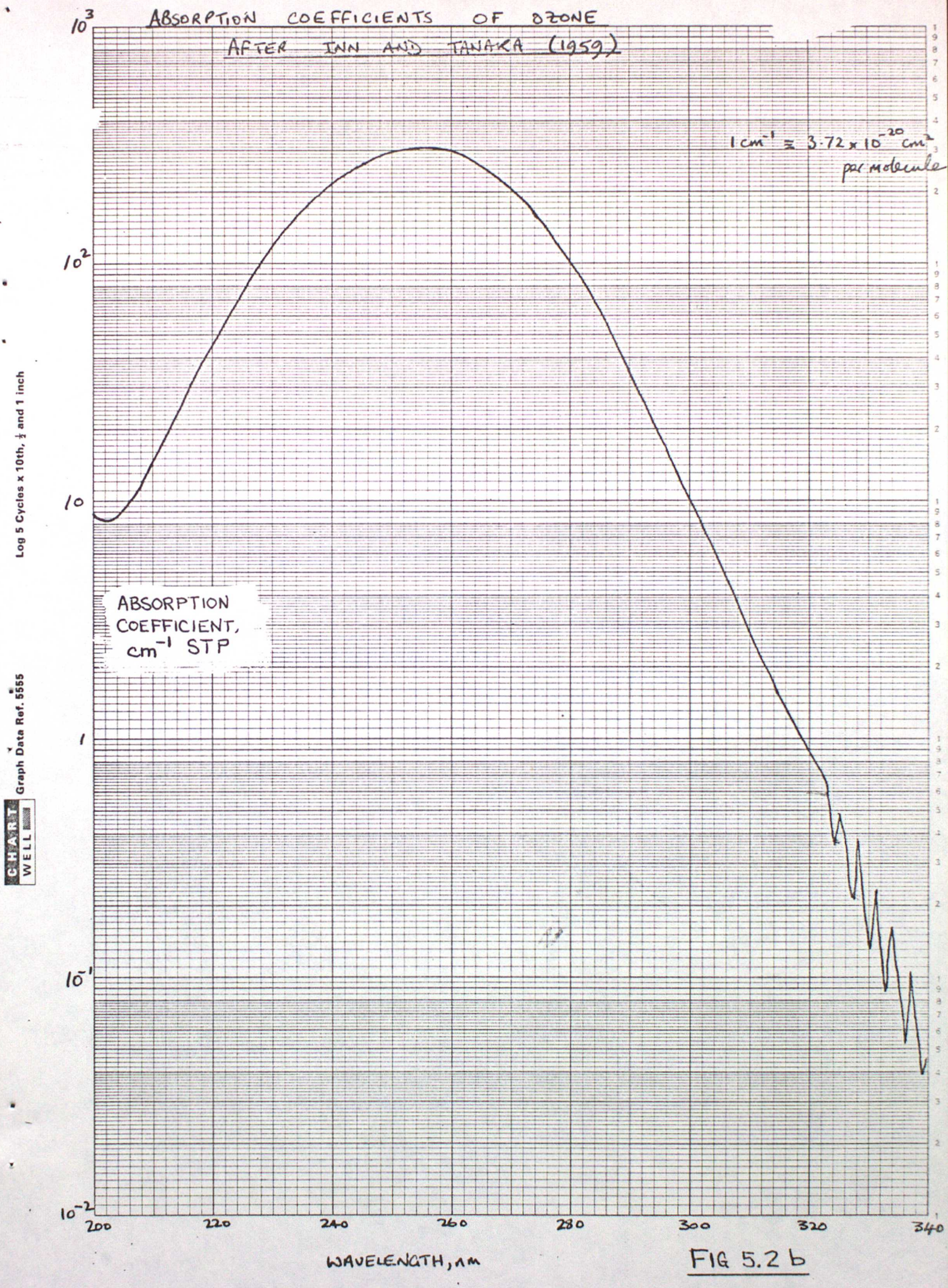
ABSORPTION COEFFICIENTS OF OZONE
AFTER INN AND TANAKA (1959)
$1\,cm^{-1} \equiv 3.72 \times 10^{-20}\,cm^2$ per molecule
ABSORPTION COEFFICIENT, cm^{-1} STP
10^3
10^2
10
1
10^{-1}
10^{-2}
200
220
240
260
280
300
320
340
WAVELENGTH, nm
Log 5 Cycles x 10th, ½ and 1 inch
Graph Data Ref. 5555
CHART WELL

FIG 5.2 b

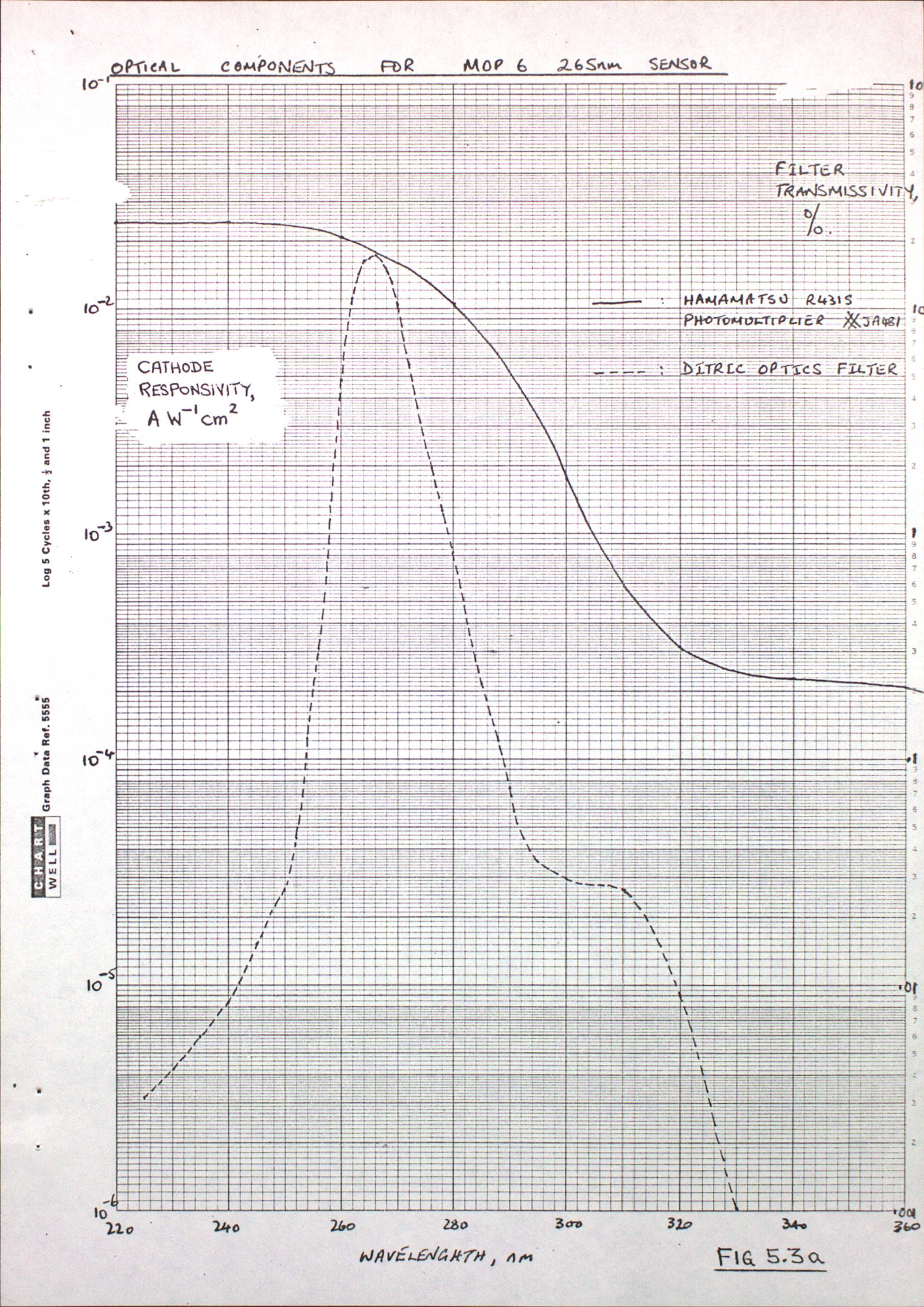
OPTICAL COMPONENTS FOR MOP 6 265nm SENSOR
FILTER TRANSMISSIVITY, %.
HAMAMATSU R431S PHOTOMULTIPLIER XJA481
DITRIC OPTICS FILTER
CATHODE RESPONSIVITY, A W⁻¹ cm²
10⁻¹
10⁻²
10⁻³
10⁻⁴
10⁻⁵
10⁻⁶
220
240
260
280
300
320
340
360
WAVELENGHTH, nm
Log 5 Cycles x 10th, ½ and 1 inch
Graph Data Ref. 5555
CHART WELL

FIG 5.3a

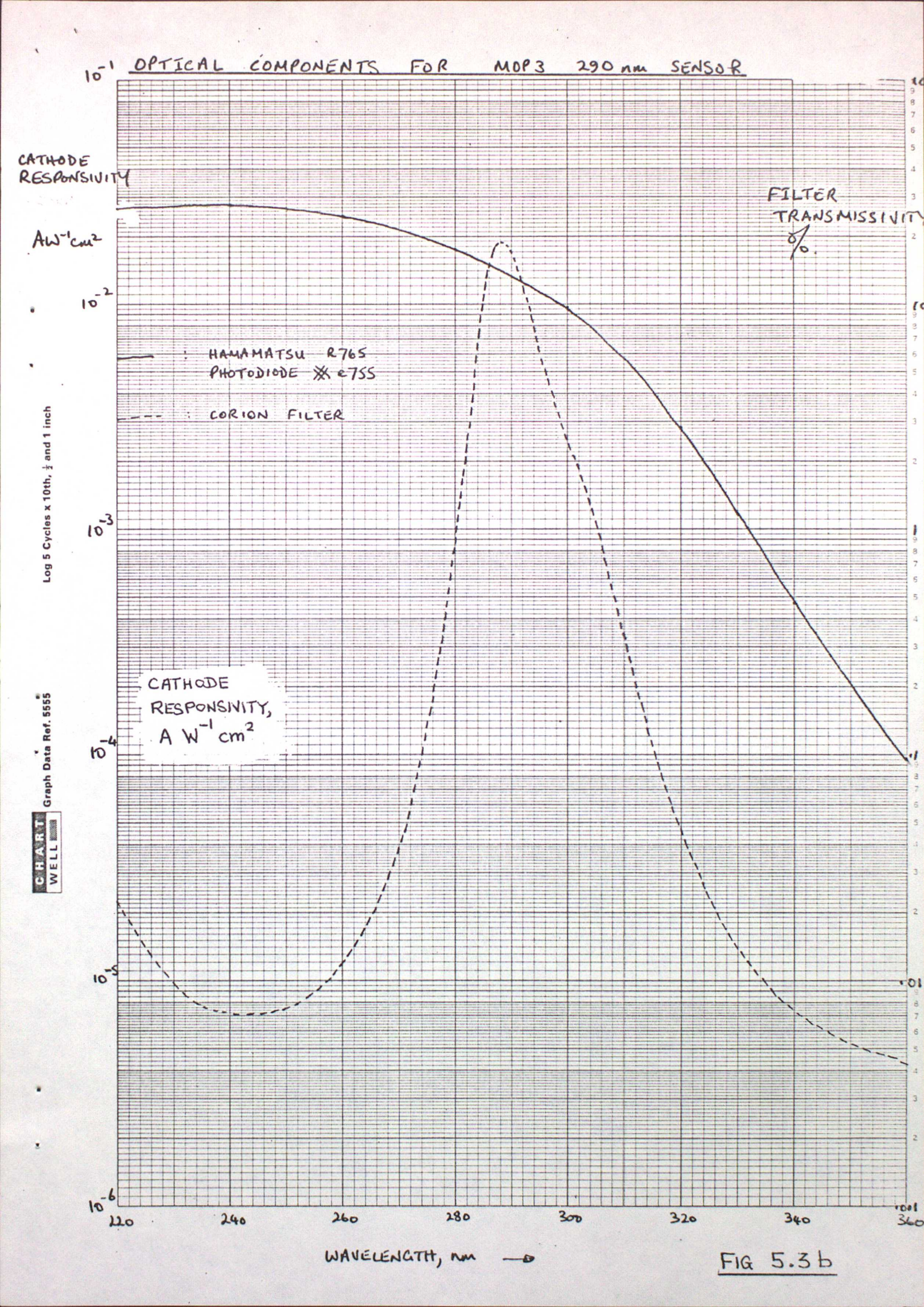
OPTICAL COMPONENTS FOR MOP3 290 nm SENSOR
CATHODE RESPONSIVITY
AW⁻¹cm²
FILTER TRANSMISSIVITY %
HAMAMATSU R765 PHOTODIODE ※ e755
CORION FILTER
CATHODE RESPONSIVITY, A W⁻¹ cm²
Log 5 Cycles x 10th, ½ and 1 inch
Graph Data Ref. 5555
CHART WELL
10⁻¹
10⁻²
10⁻³
10⁻⁴
10⁻⁵
10⁻⁶
220
240
260
280
300
320
340
360
WAVELENGTH, nm

FIG 5.3b

DETECTOR SPECTRUM CONVOLVED WITH FULL SUN SPECTRUM.

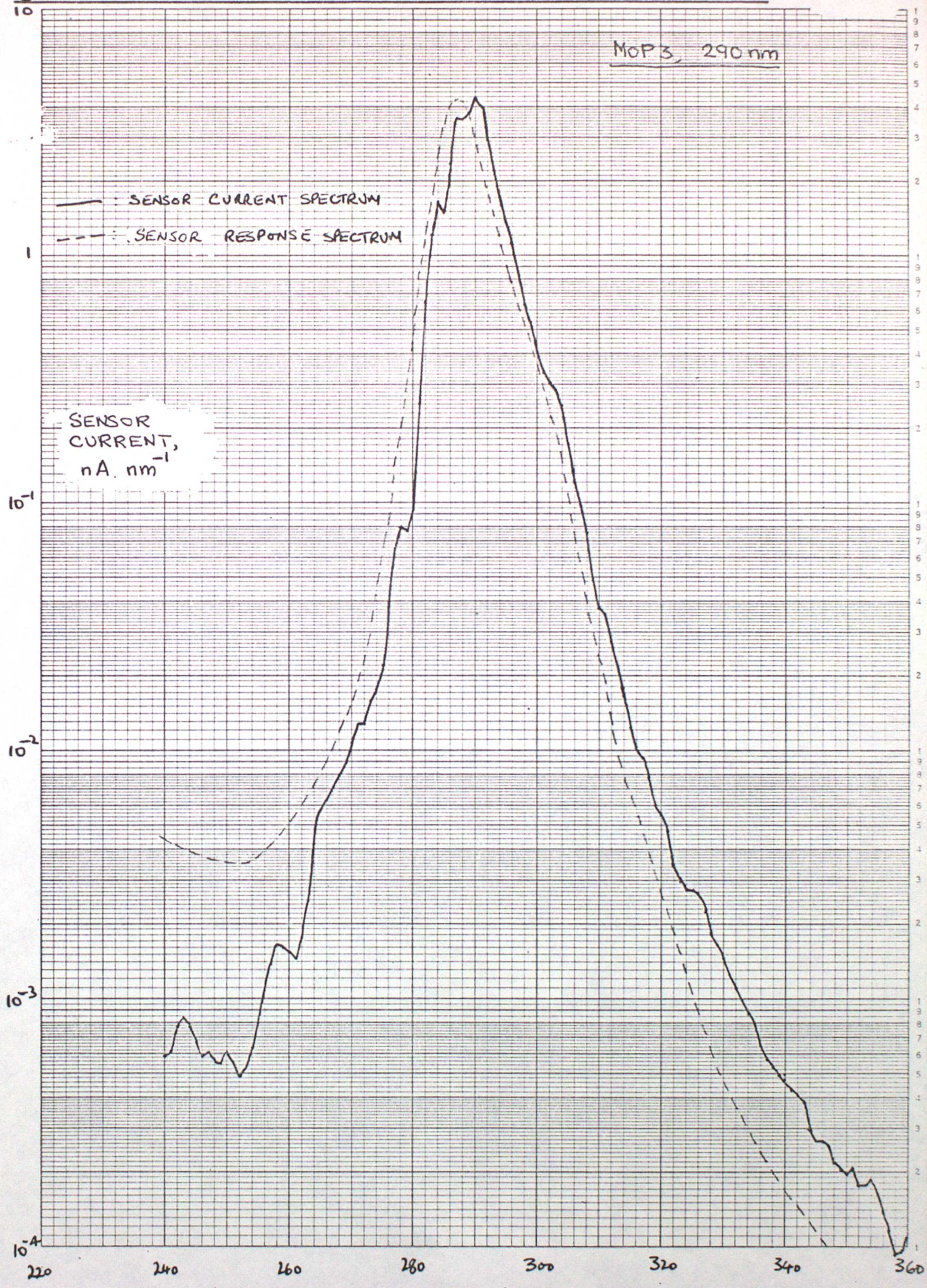

FIG 5.3c

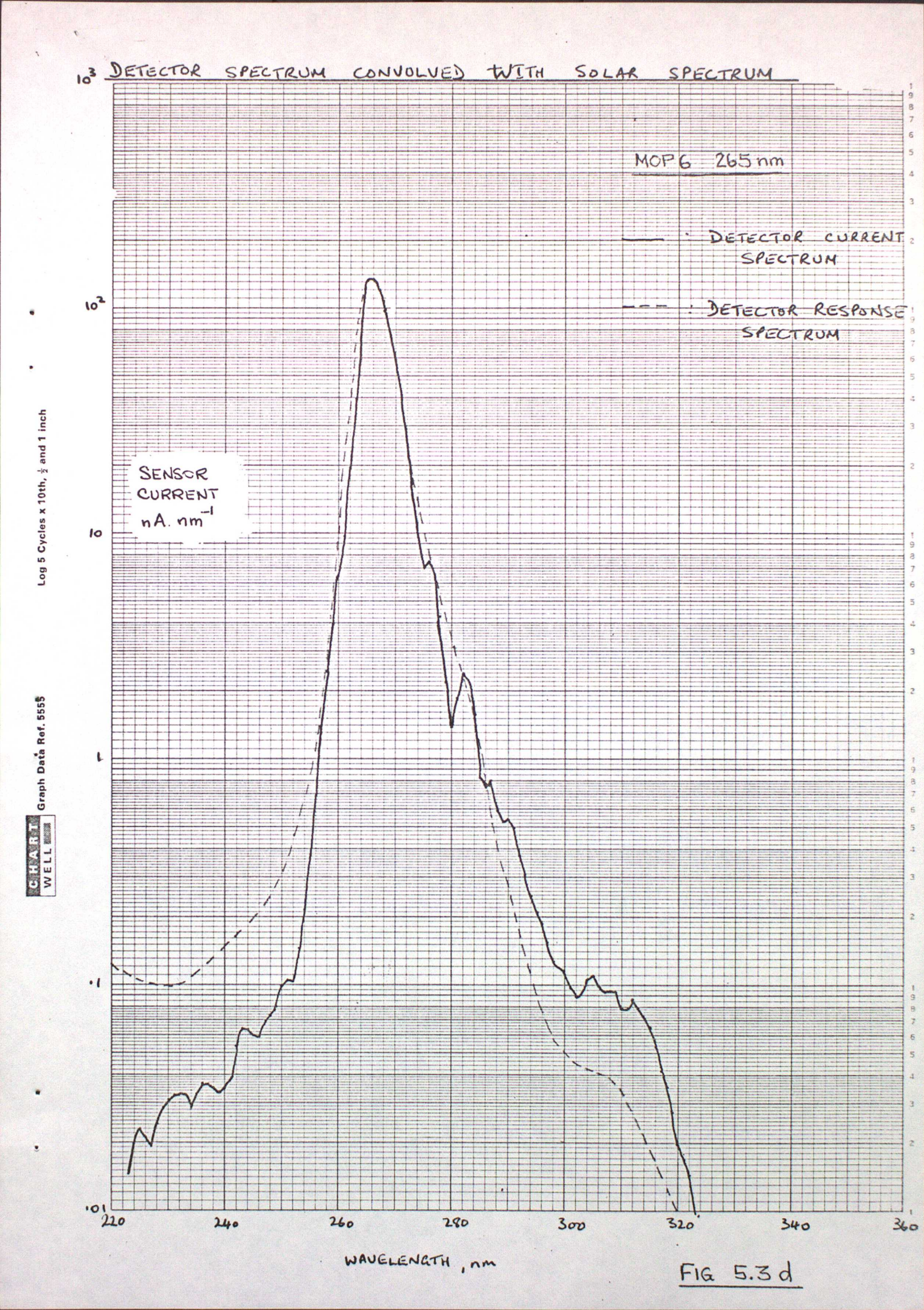
DETECTOR SPECTRUM CONVOLVED WITH SOLAR SPECTRUM
MOP 6 265 nm
—— : DETECTOR CURRENT SPECTRUM
– – – : DETECTOR RESPONSE SPECTRUM
SENSOR CURRENT nA. nm⁻¹
10³
10²
10
1
·1
·01
220
240
260
280
300
320
340
360
WAVELENGTH, nm
Log 5 Cycles x 10th, ½ and 1 inch
Graph Data Ref. 5555
CHART WELL

FIG 5.3 d

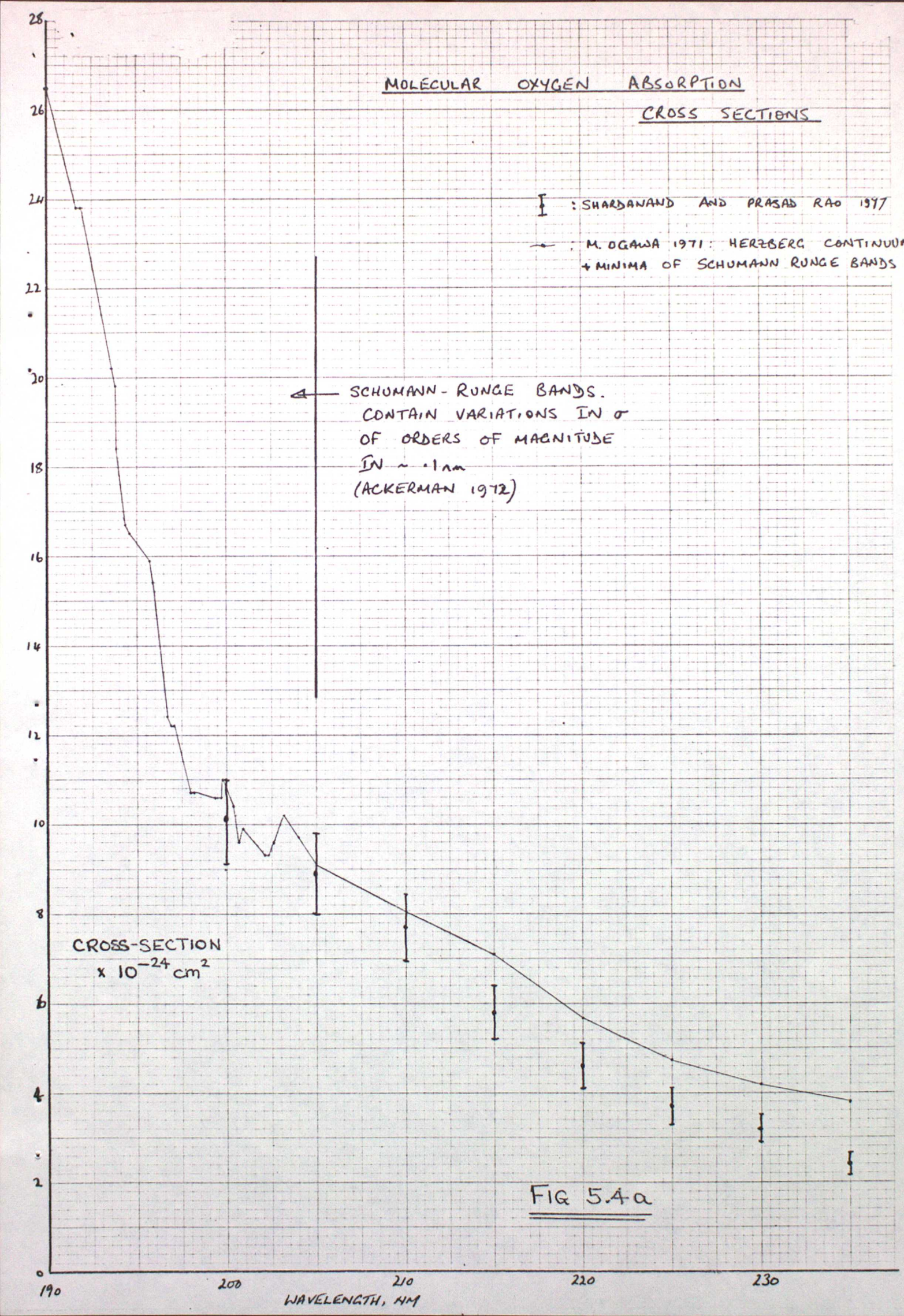
MOLECULAR OXYGEN ABSORPTION CROSS SECTIONS
: SHARDANAND AND PRASAD RAO 1977
: M. OGAWA 1971: HERZBERG CONTINUUM + MINIMA OF SCHUMANN RUNGE BANDS
SCHUMANN-RUNGE BANDS. CONTAIN VARIATIONS IN σ OF ORDERS OF MAGNITUDE IN ~ ·1nm (ACKERMAN 1972)
CROSS-SECTION x 10⁻²⁴ cm²
28
26
24
22
20
18
16
14
12
10
8
6
4
2
0
190
200
210
220
230
WAVELENGTH, NM

FIG 5.4a

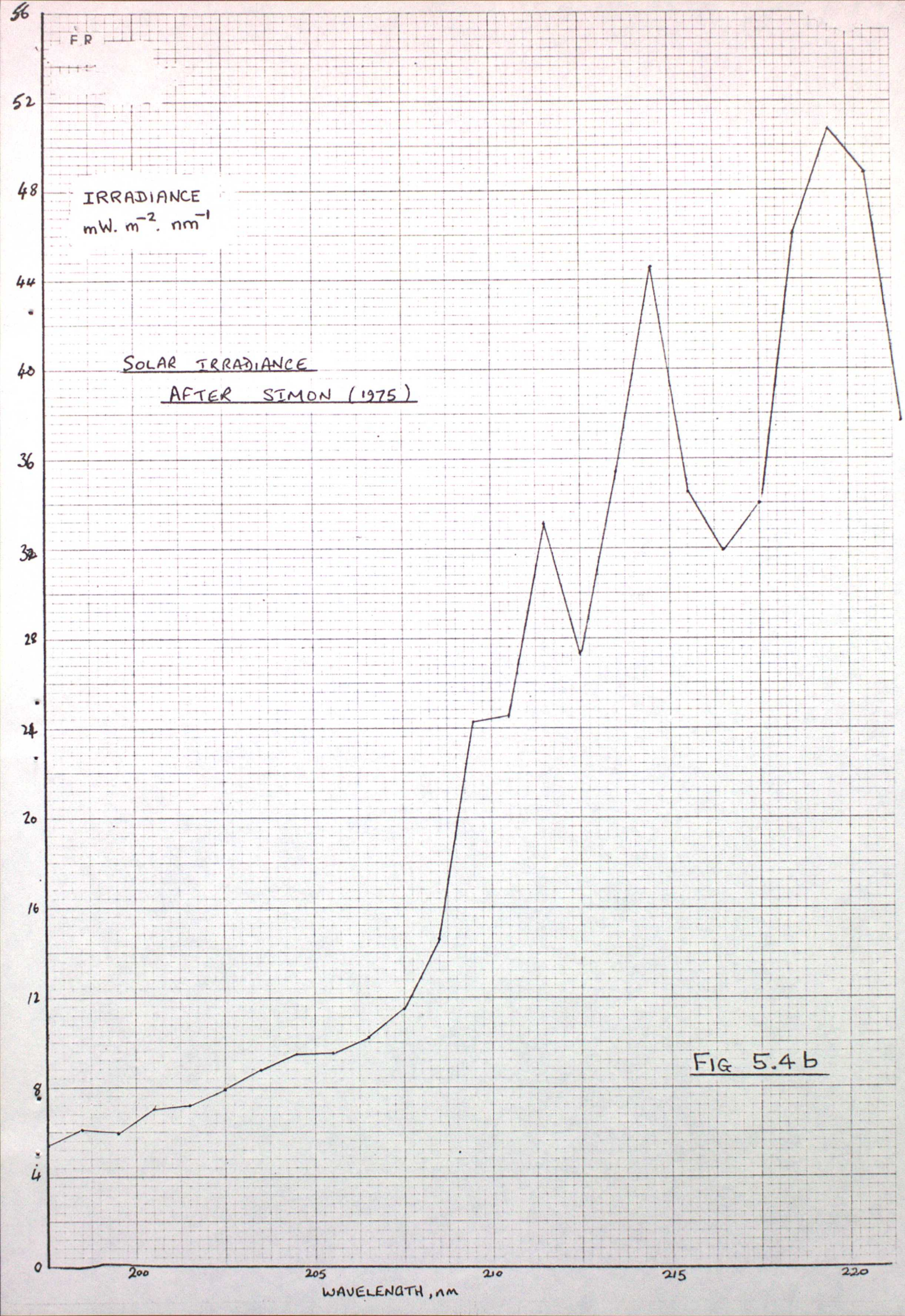
56
FR
52
48
IRRADIANCE
mW. m^{-2}. nm^{-1}
44
40
SOLAR IRRADIANCE
AFTER SIMON (1975)
36
32
28
24
20
16
12
8
4
0
200
205
210
215
220
WAVELENGTH, nm

FIG 5.4b

OXYGEN SENSOR:

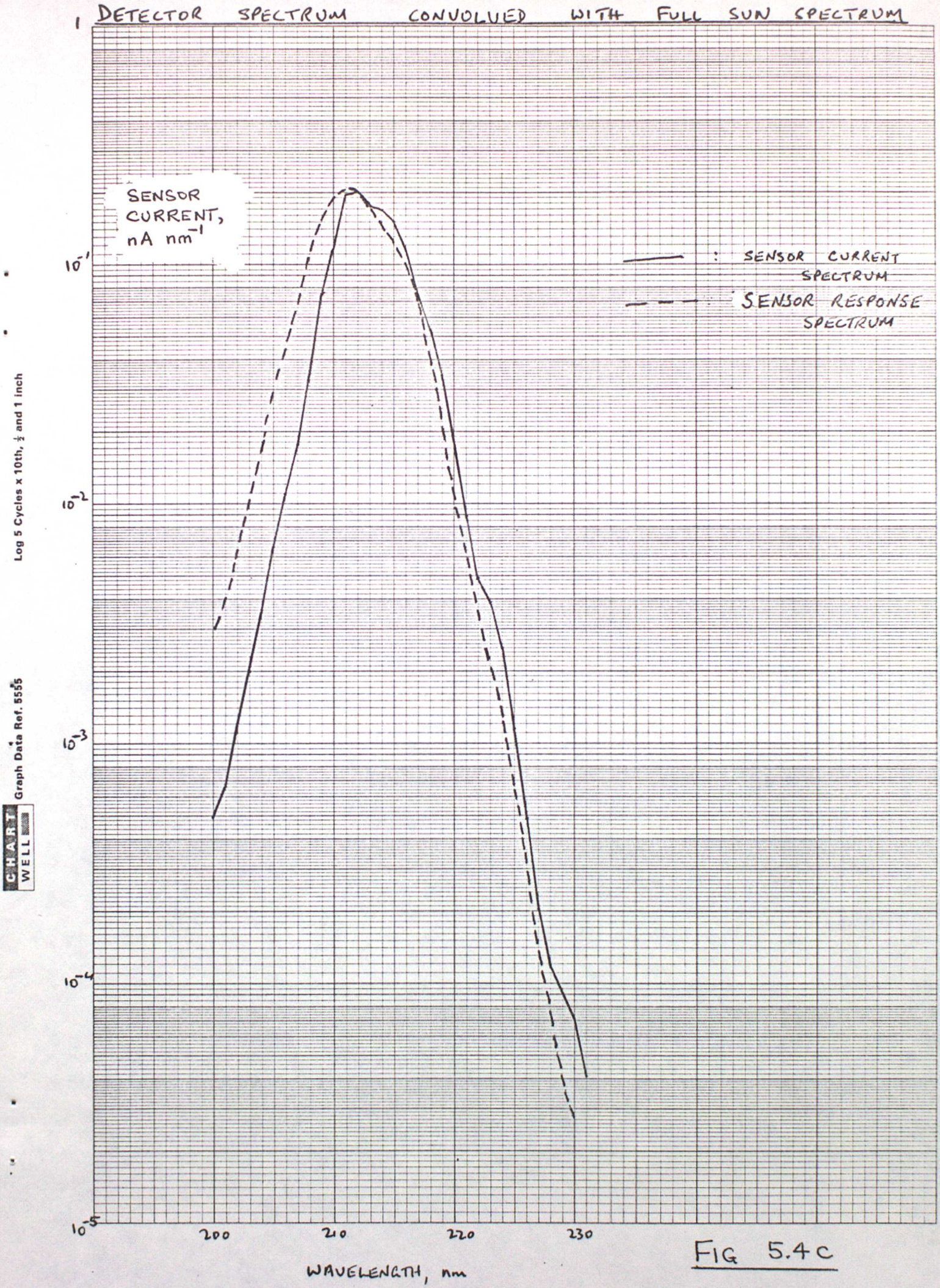

FIG 5.4c

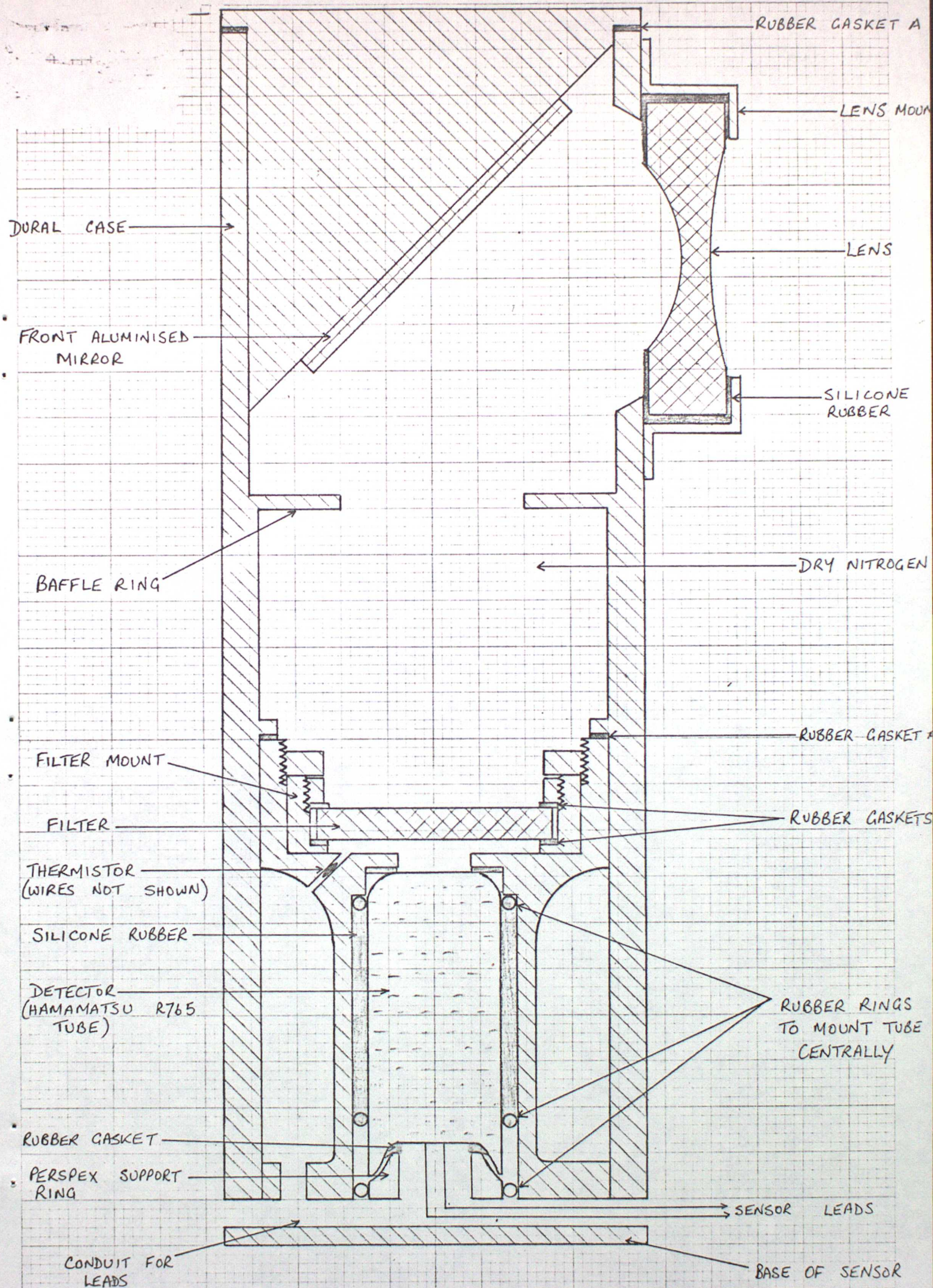

FIG 5.5a(i) MOP3 SENSOR. Scale: Twice Full Size

E.R.

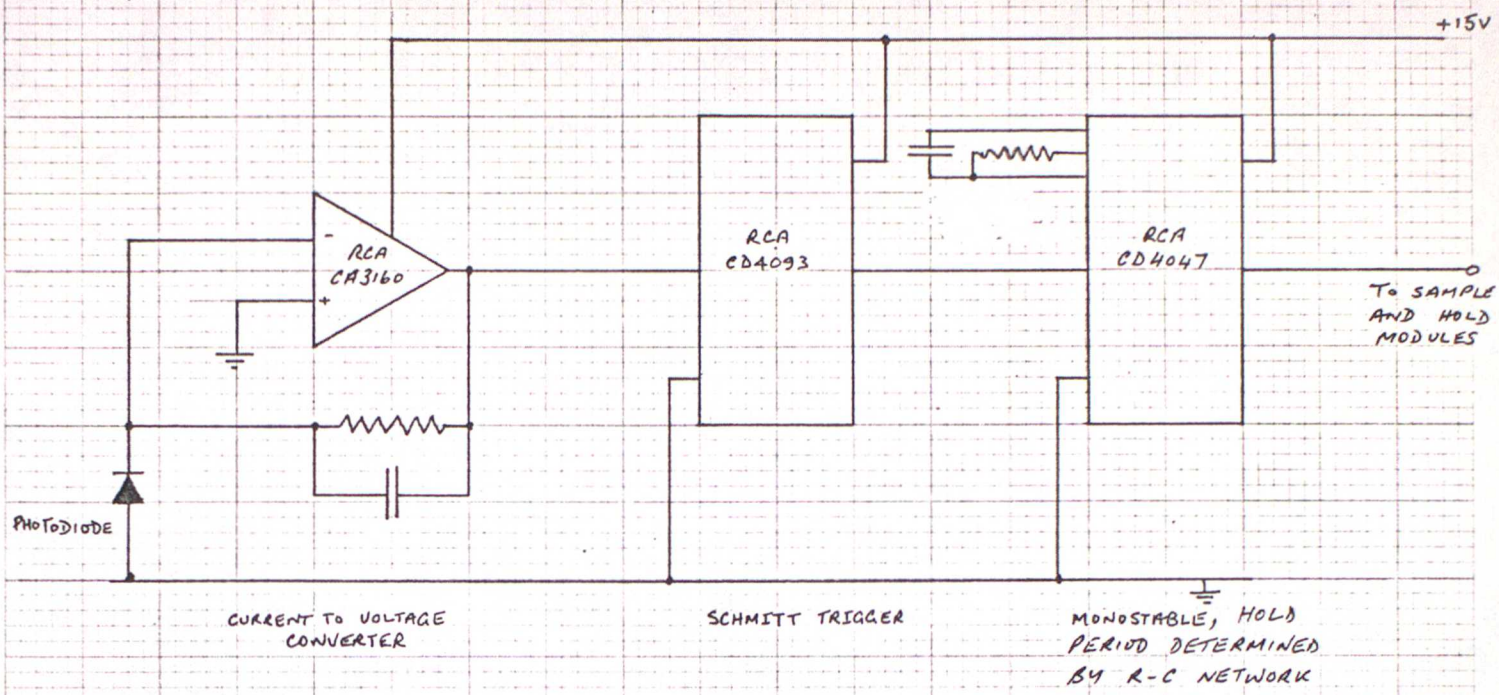

Fig. 5.5b(i) CIRCUIT FOR MOP3 TRIGGER DIODES

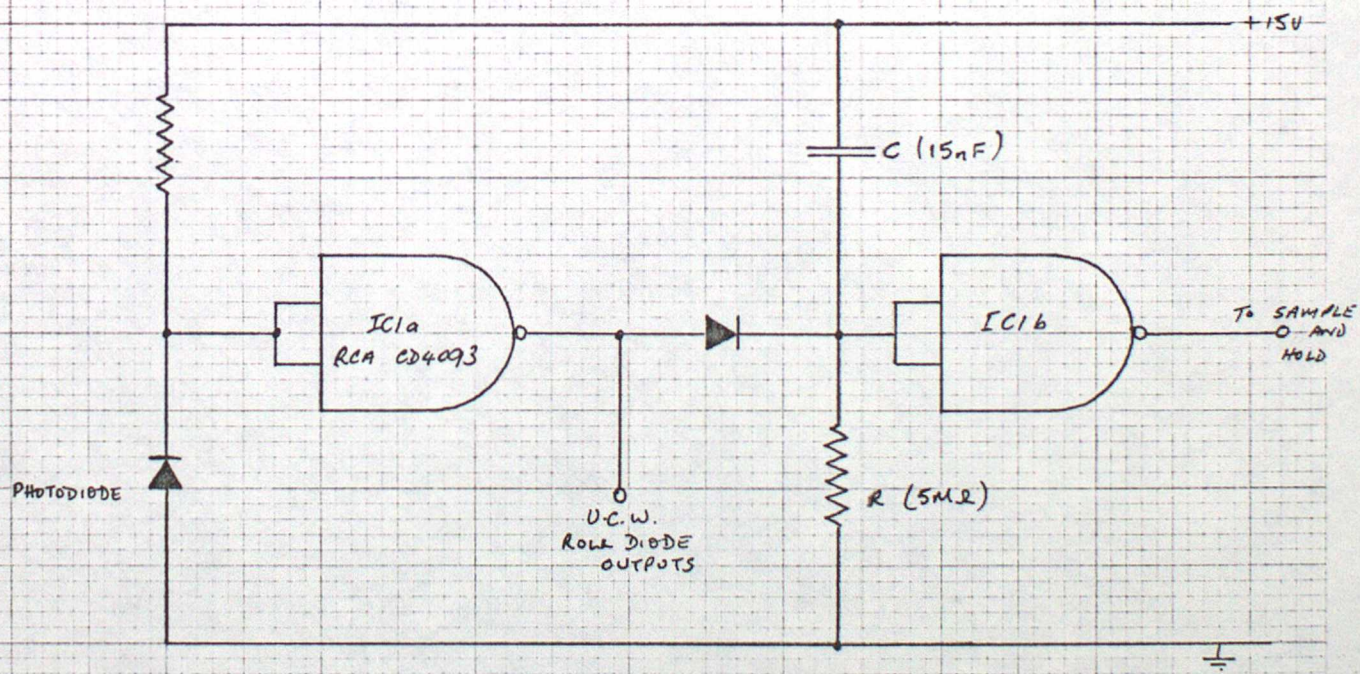

Fig 5.5b(ii) CIRCUIT FOR MOP 5 & 7 TRIGGER DIODES. (ONE DIODE ONLY SHOWN)

R AND C DEFINE THE HOLD PERIOD.

THE IC1 CONTAINS 4 SCHMITT TRIGGER CIRCUITS, TWO FOR EACH DIODE.

Fig 5.6a

VERTICAL CROSS SECTION OF THE OPTICAL SECTION

E.R.

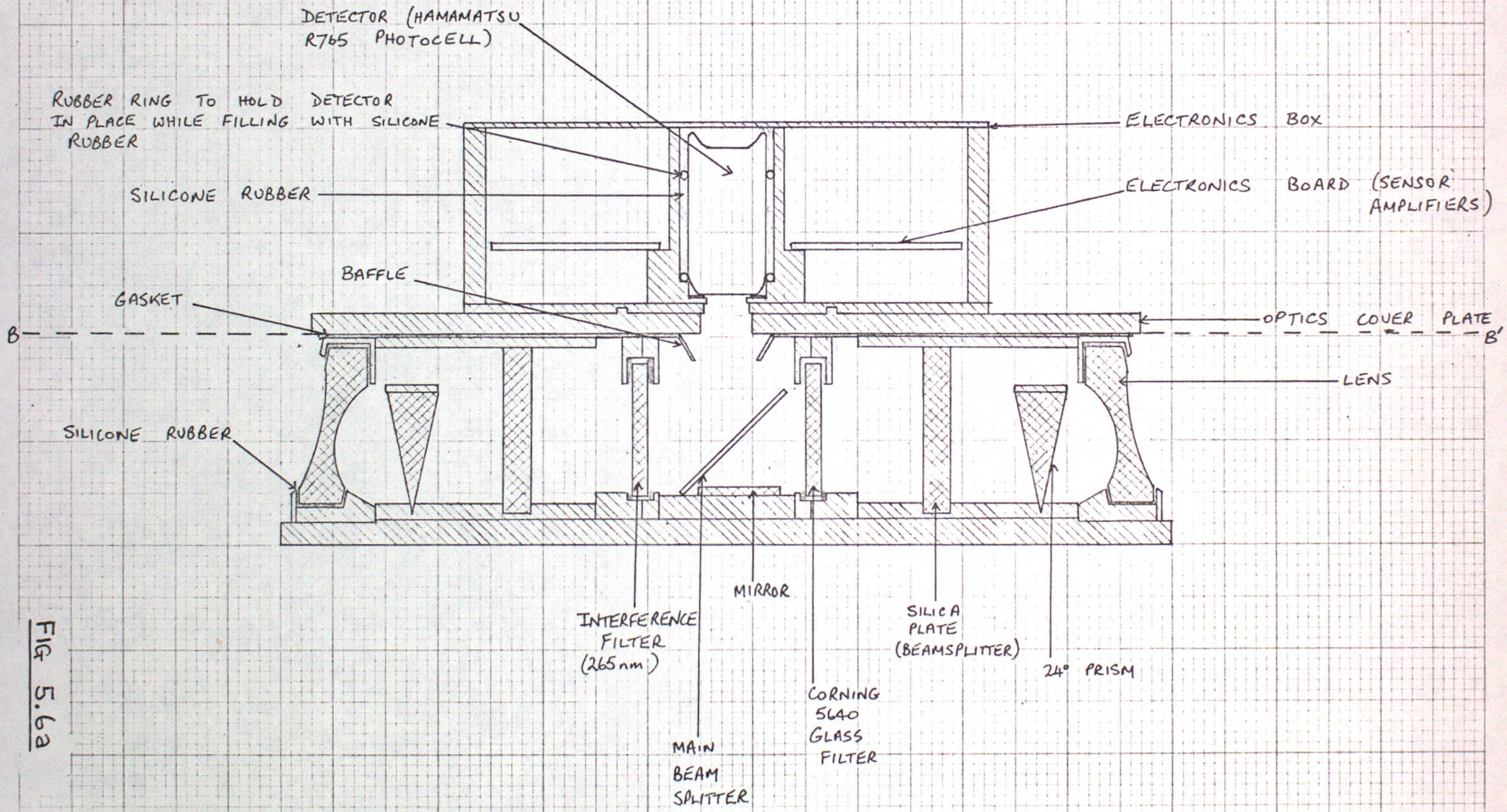

FIG 5.6a

SECTION: A – A' ON FIG. 5.6 c

SCALE: FULL SIZE

DAYTIME ROUND MONITOR CHANNEL SPECTRAL RESPONSIVITY

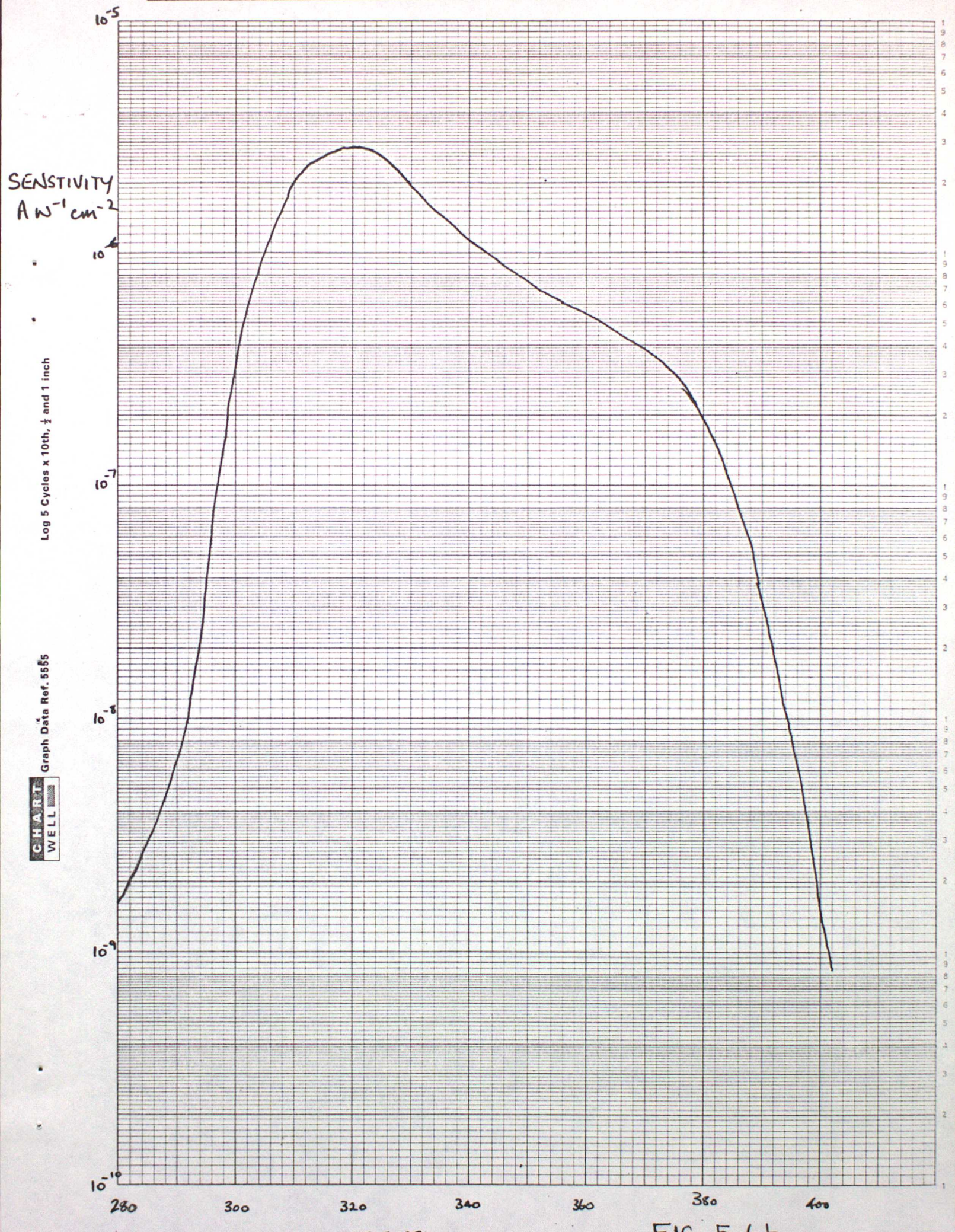

FIG 5.6b

E.R.

PLAN VIEW OF OPTICS SECTION

(SECT BB' ON FIG. 5.6a)

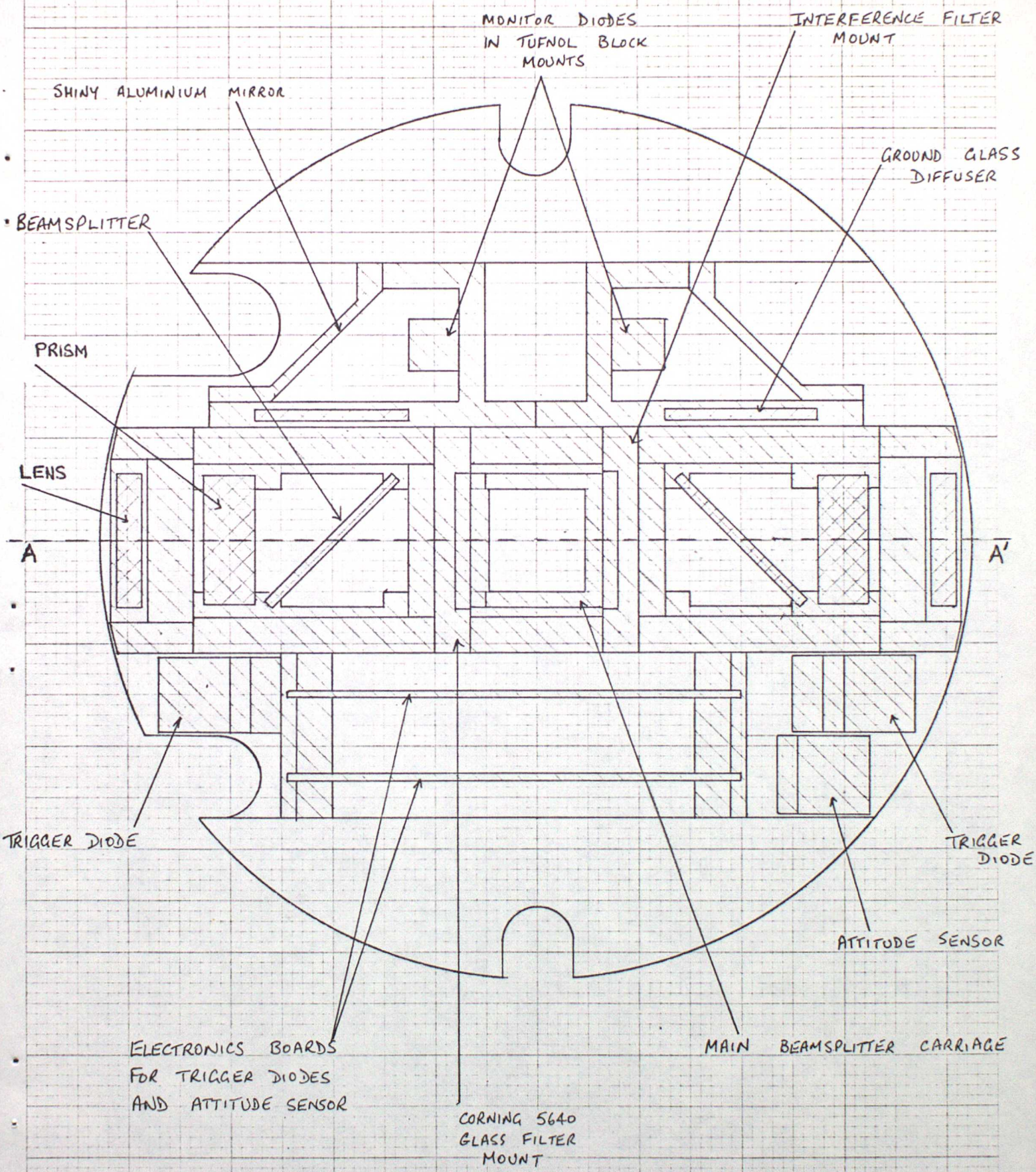

FIG 5.6c

SCALE : FULL SIZE

E.R.

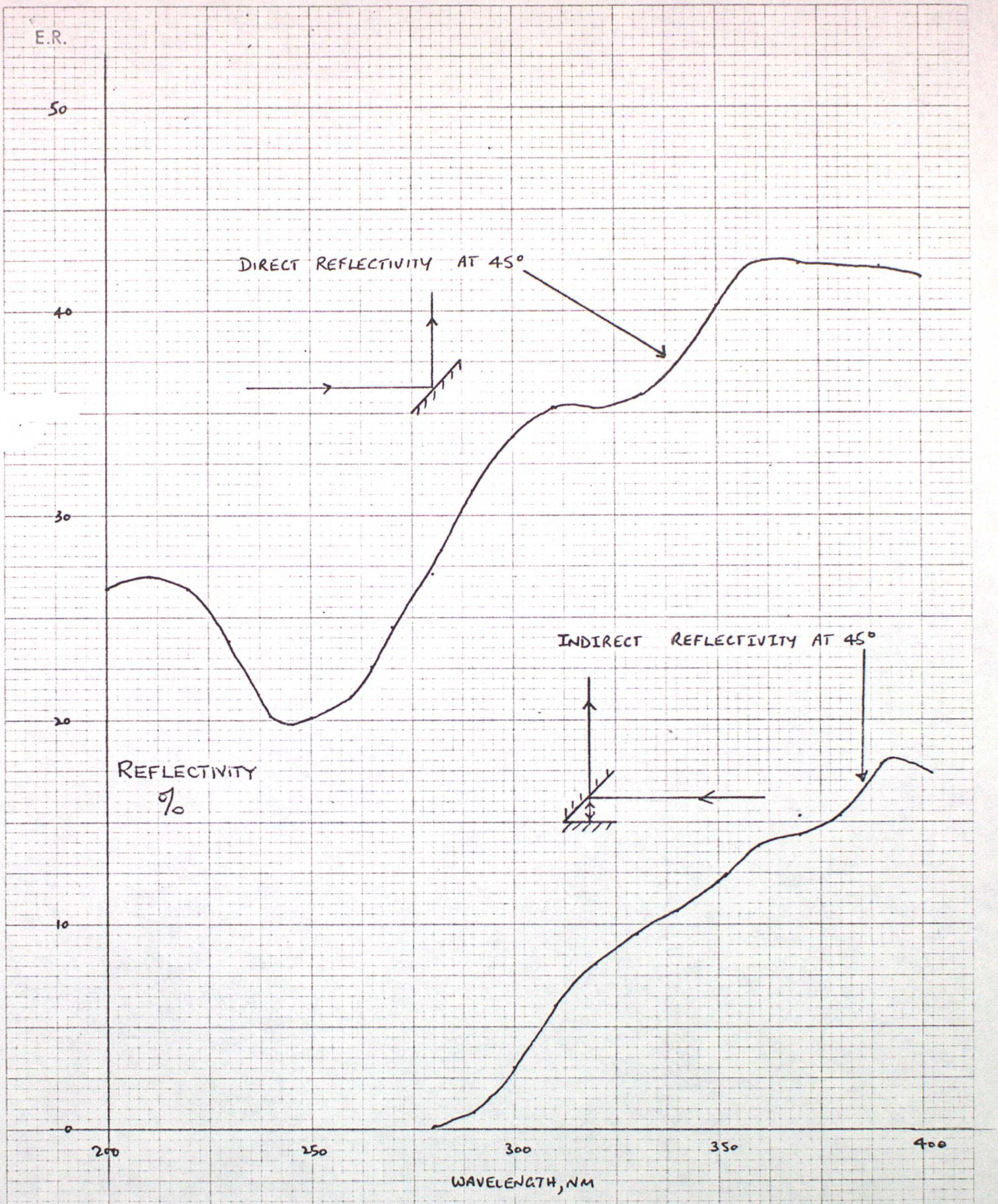

Fig. 5.6d REFLECTIVITY OF DAYTIME BEAMSPLITTERS

FIG 5.6c
MOP 5 (MORNING) PAYLOAD

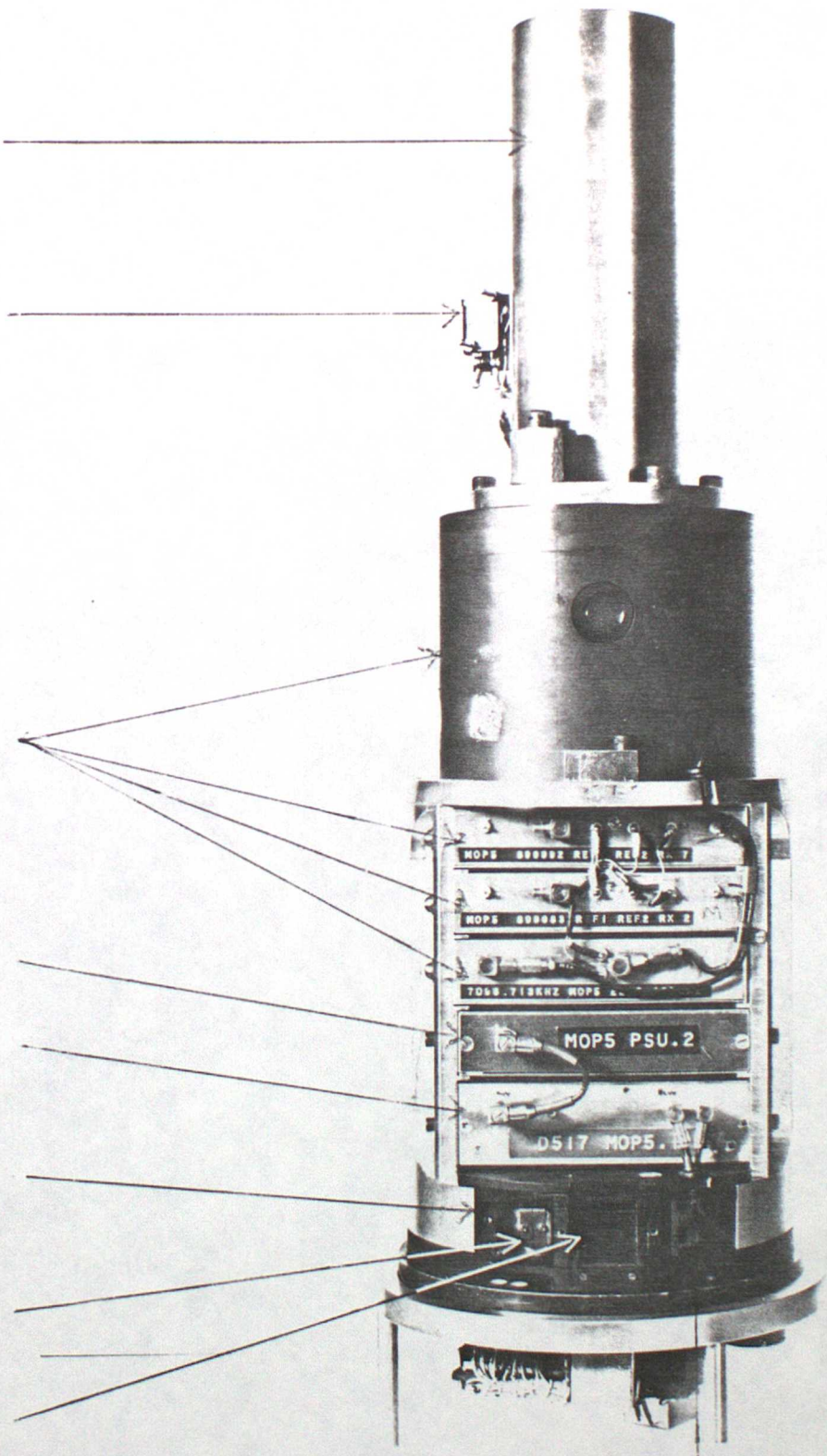

METAL BLOCK FOR BALLAST

NOSE-CONE RELEASE MONITOR

U.C.W. FARADAY ROTATION EXPERIMENT

POWER SUPPLY BOX

AMPLIFIER AND MAIN SENSOR BOX

ATTITUDE SENSOR

TRIGGER DIODE

FRONT LENS (OZONE SENSOR SIDE)

SHINY PLATE (REFLECTOR FOR MONITOR DIODE)

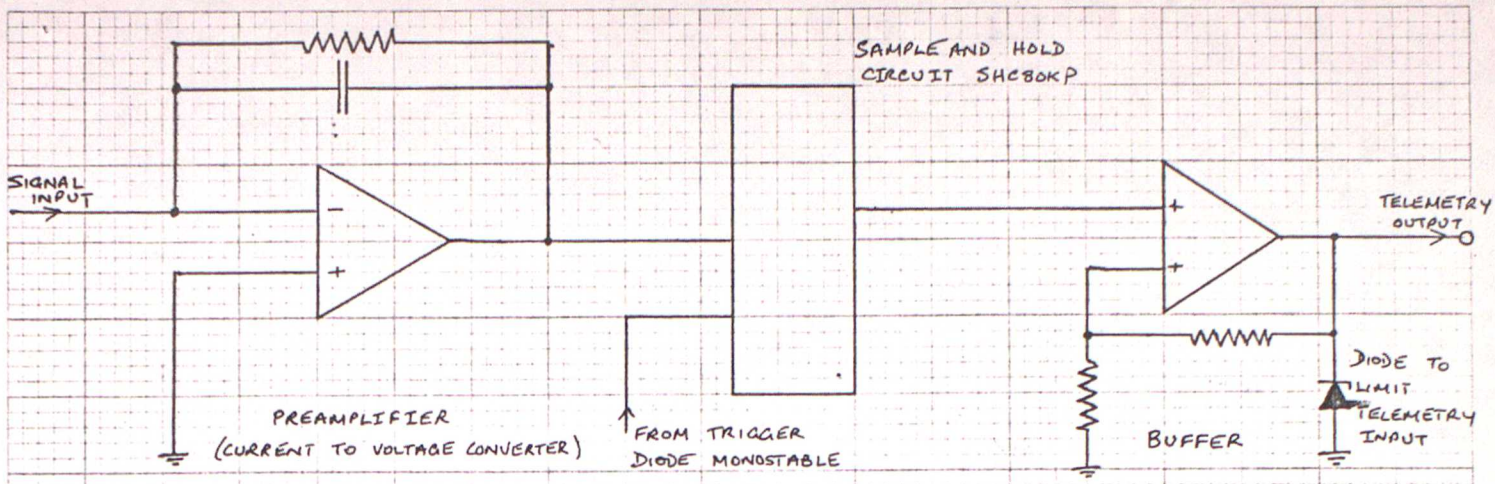

FIG. 5.7(i) PRINCIPALS OF SIGNAL AMPLIFIER CIRCUITS

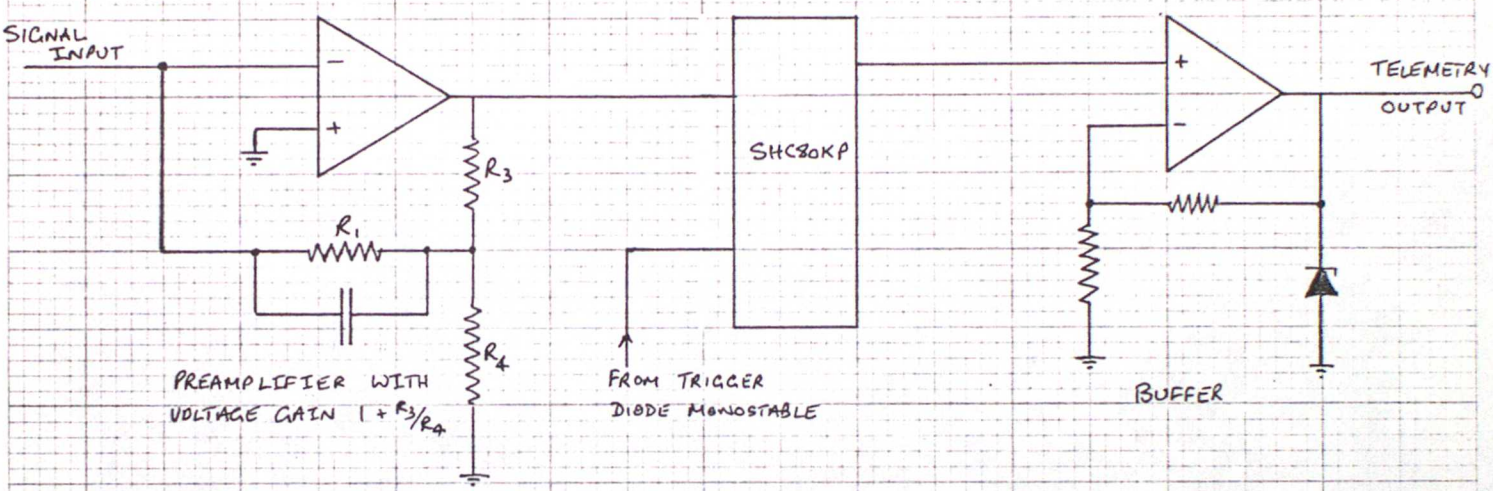

FIG 5.7(ii) SIGNAL AMPLIFIER CIRCUIT WITH PREAMPLIFIER VOLTAGE GAIN

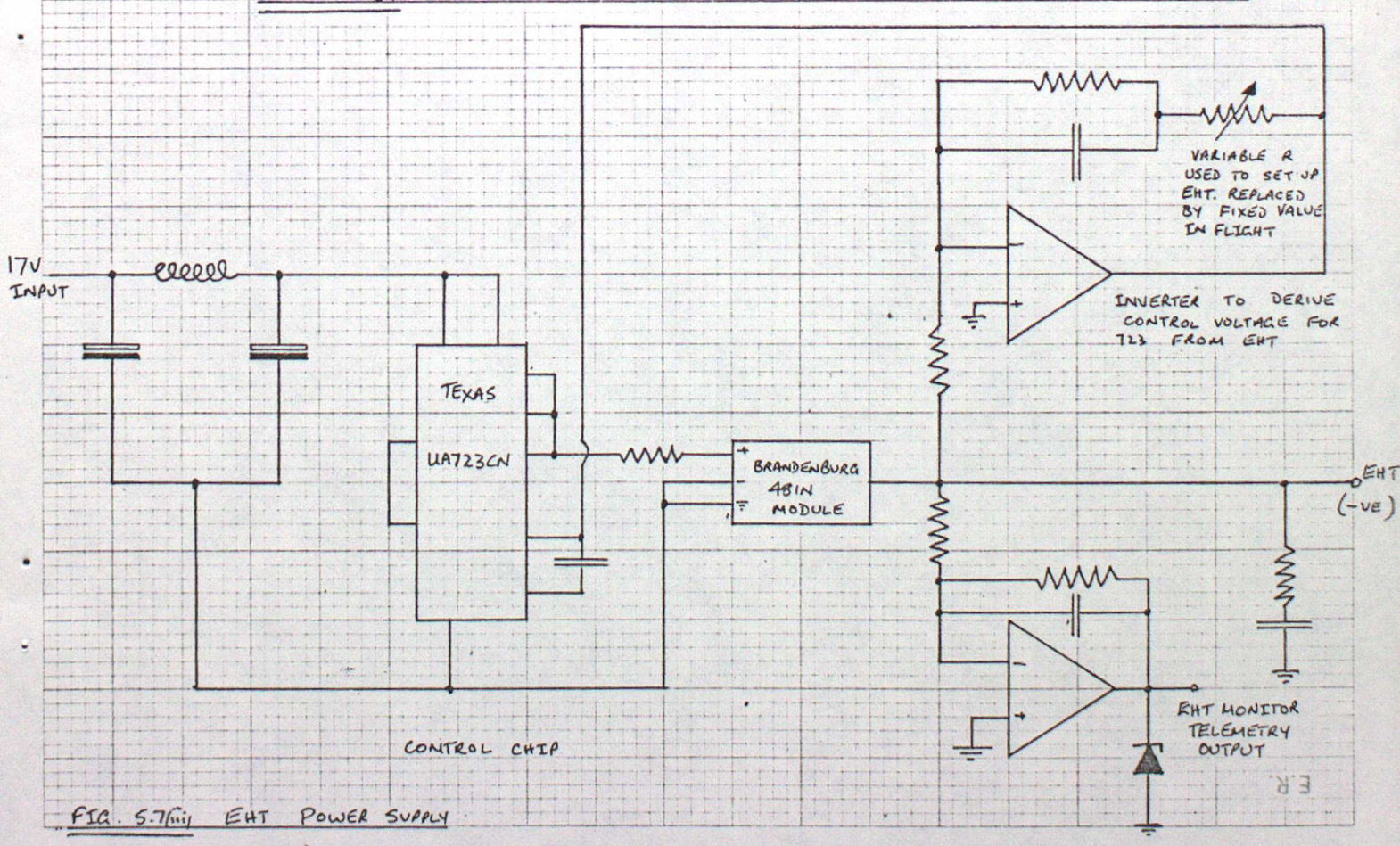

FIG. 5.7(iii) EHT POWER SUPPLY

VARIATION OF SENSITIVITY OF MOP6 265 nm SENSOR WITH ROLL ANGLE AT 266 nm

EXPECTED PULSE (8 Hz SPIN RATE)

CURVE a: D.C. CALIBRATION AS A % OF NORMAL INCIDENCE $-V(t)$

CURVE b: PREAMPLIFIER OUTPUT Δ DIVIDED BY THE FEEDBACK RESISTANCE R FOR THE CURVE (a). AS INPUT $I(t)$

PREAMPLIFIER $R = 10^7 \Omega$
$C = 330 pF$
$RC = 3.3 ms$
$\Delta f \sim 303 Hz$

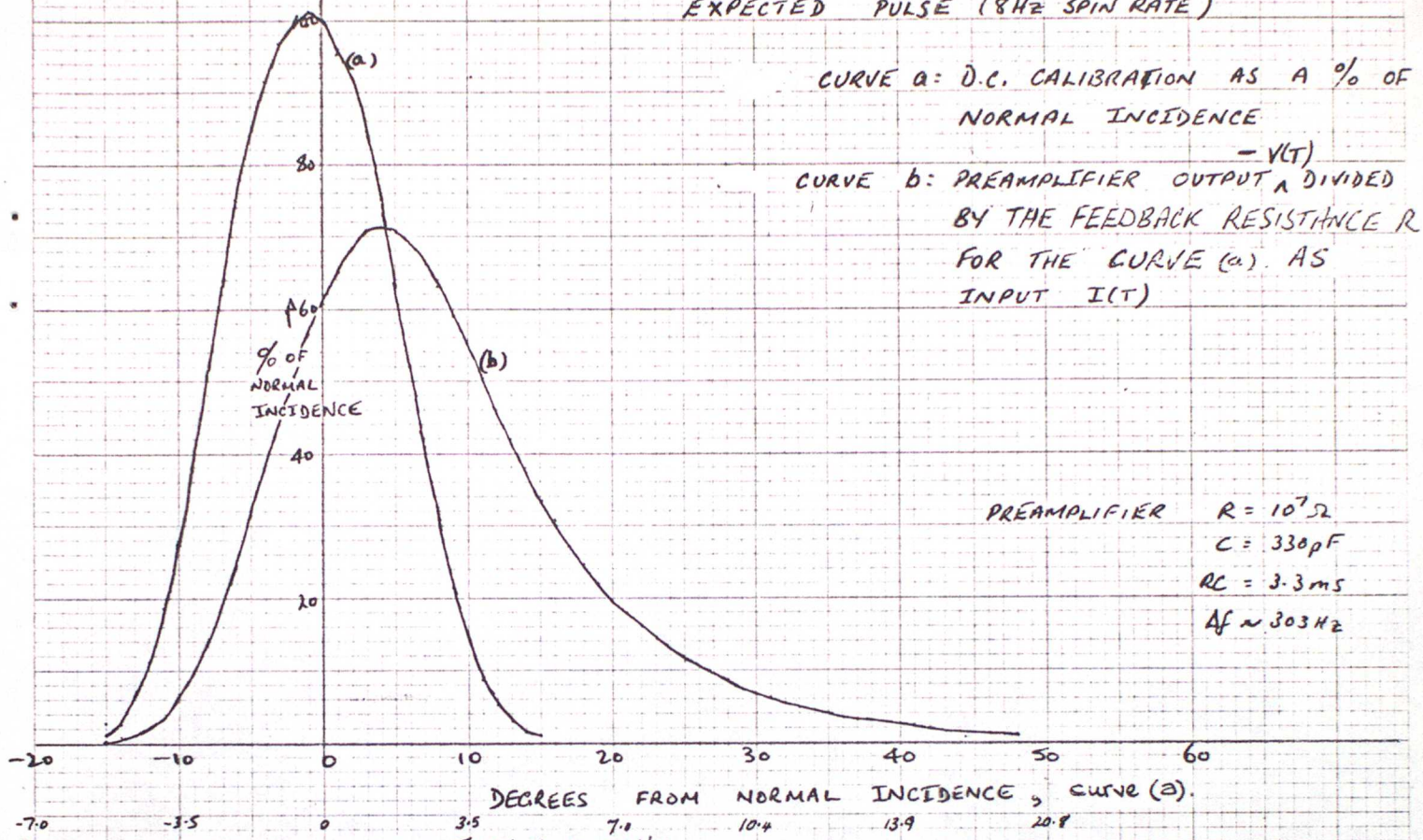

OBSERVED FLIGHT PULSE (6.9 Hz SPIN RATE)

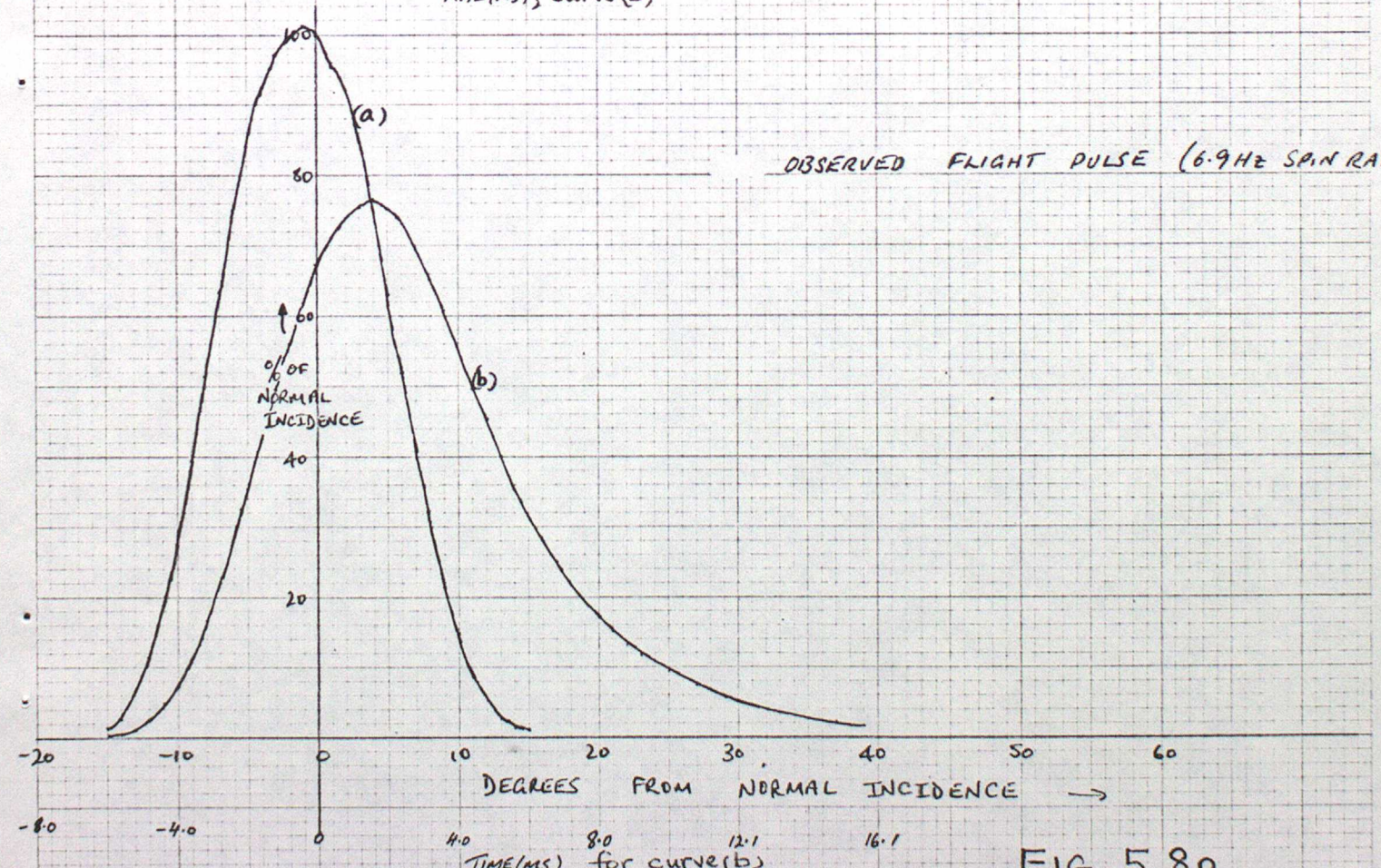

FIG 5.8a

E.D.

EXPECTED SIGNAL TO NOISE RATIOS: MOP6 265 nm SENSOR

(SEE APPENDIX A FOR DERIVATION OF VALUES AND TERMINOLOGY)

SPIN RATE 8Hz

PEAK PHOTON ARRIVAL RATE $1.6 \times 10^7 s^{-1}$

QUANTUM EFFICIENCY OF PHOTOCATHODE 10%

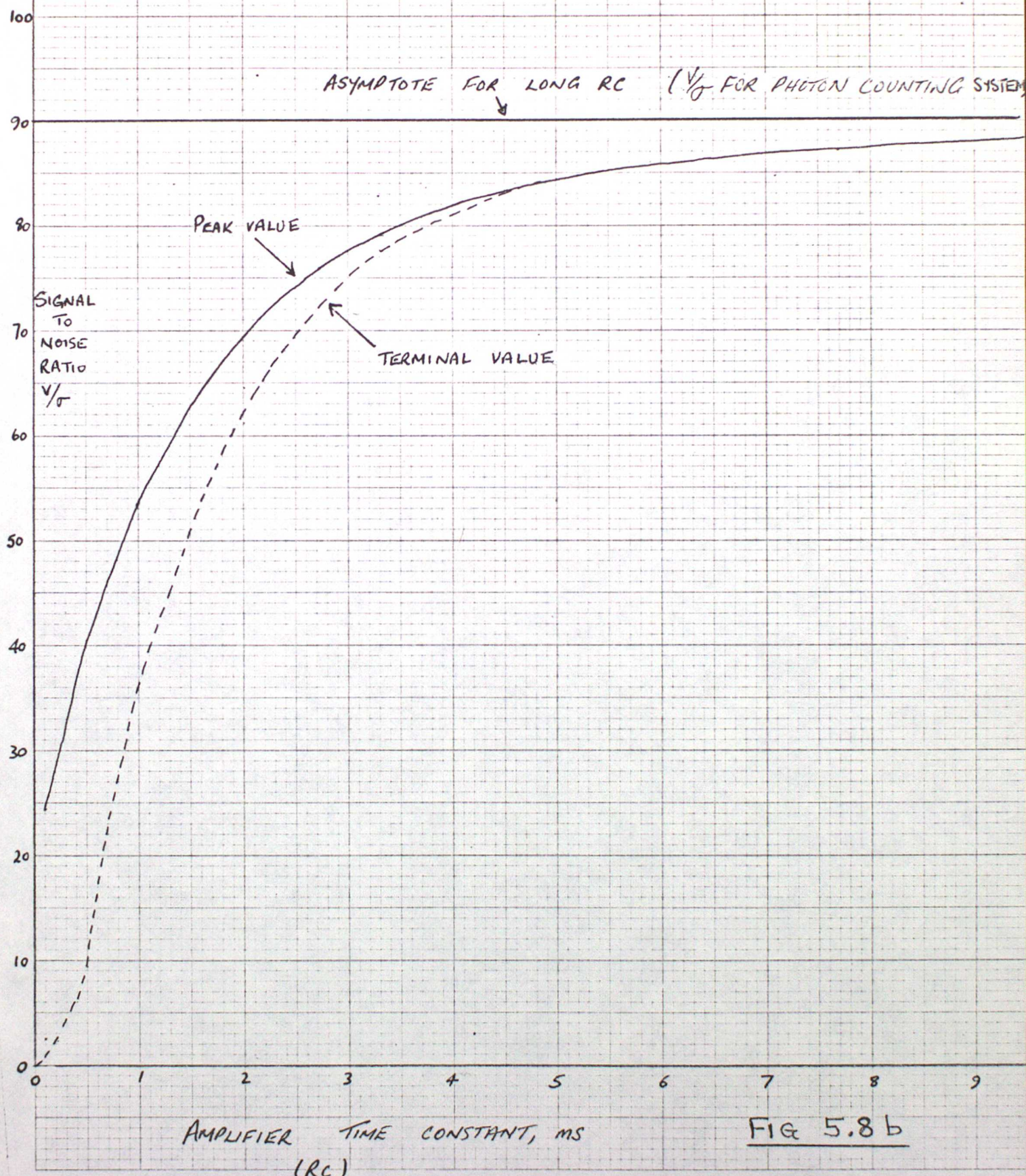

FIG 5.8b

NIGHT TIME OZONE SENSOR

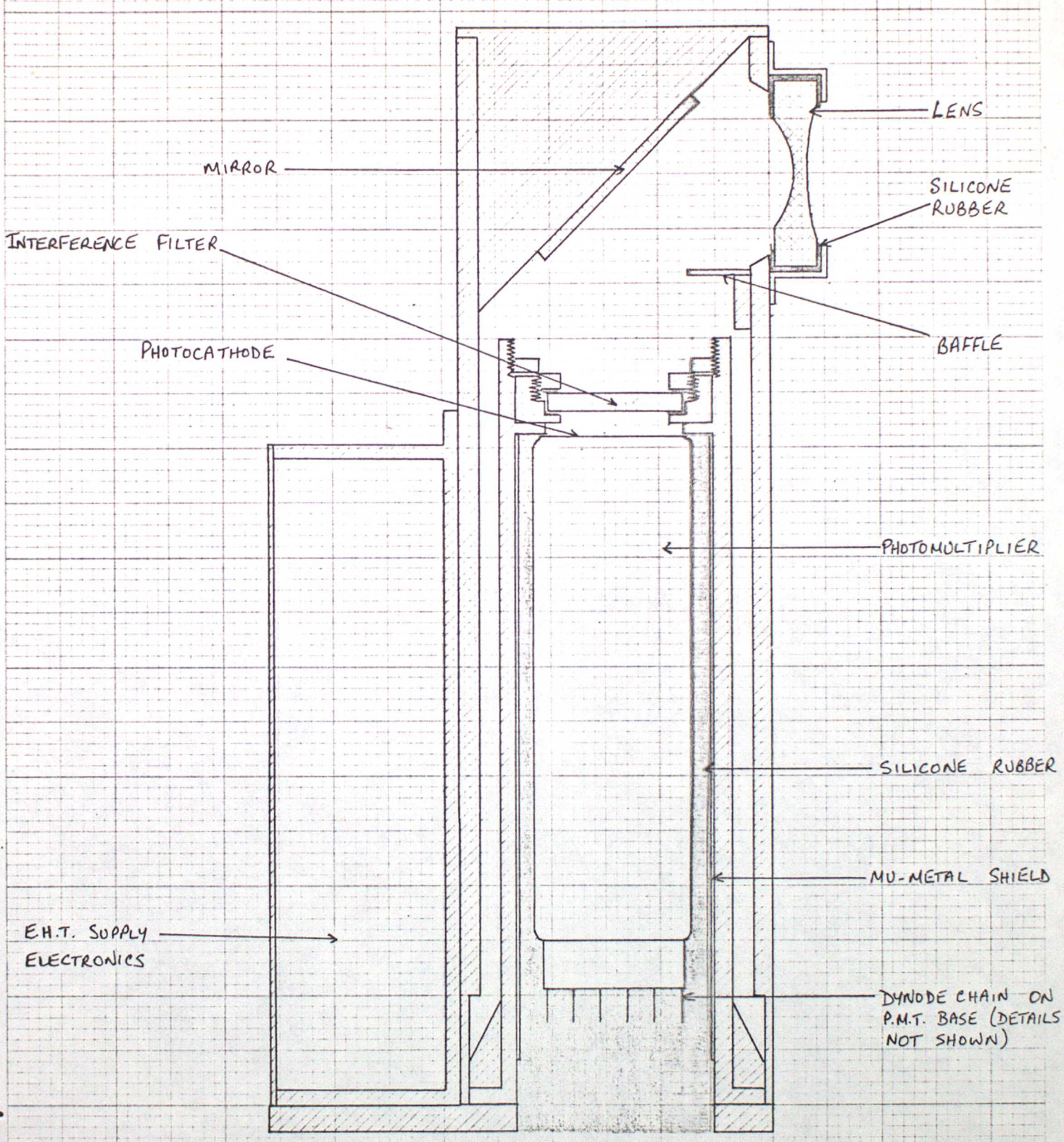

SCALE : FULL SIZE

FIG 5.8c

FIG 5.8(d)

MOP6 (NIGHT-TIME) PAYLOAD

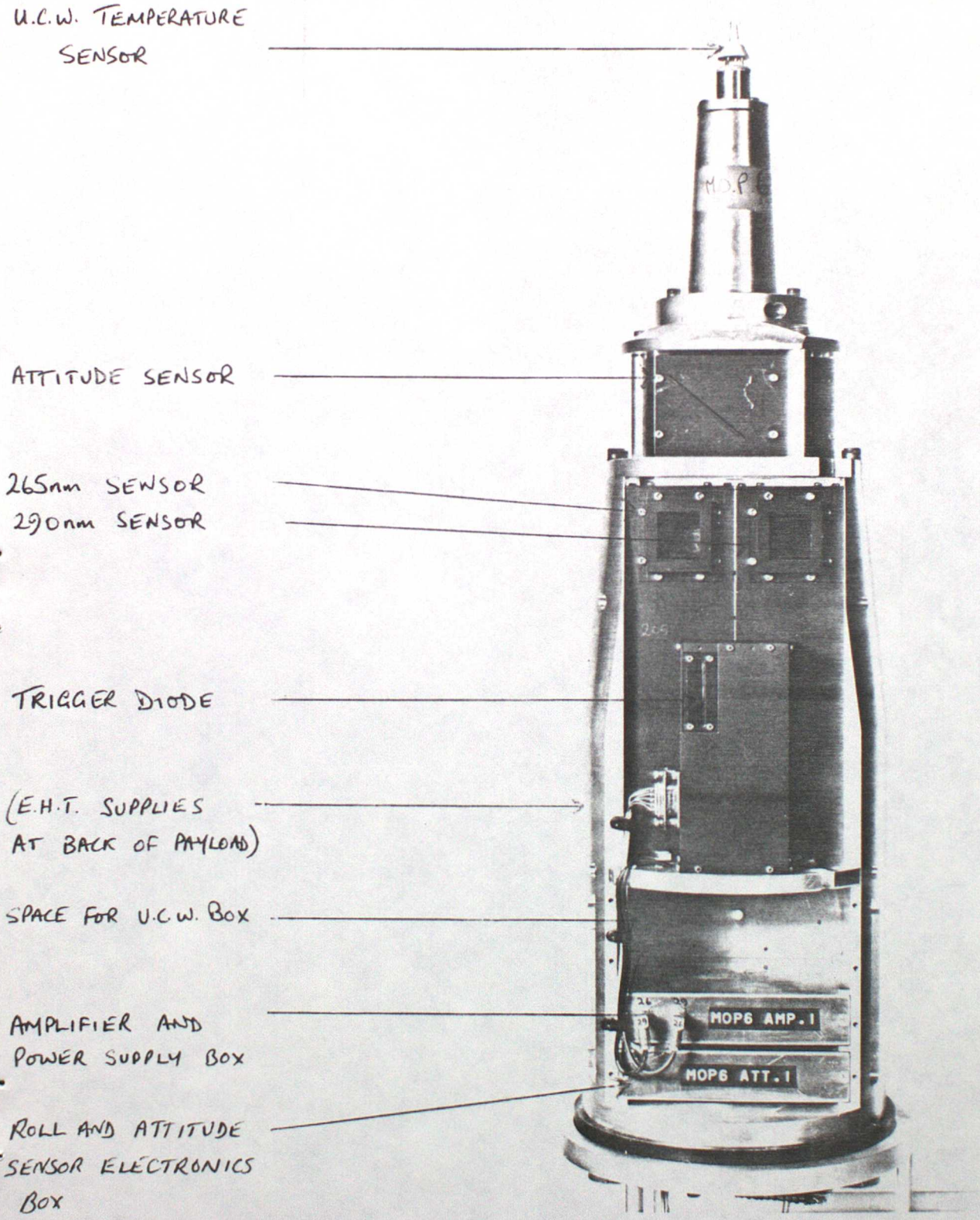

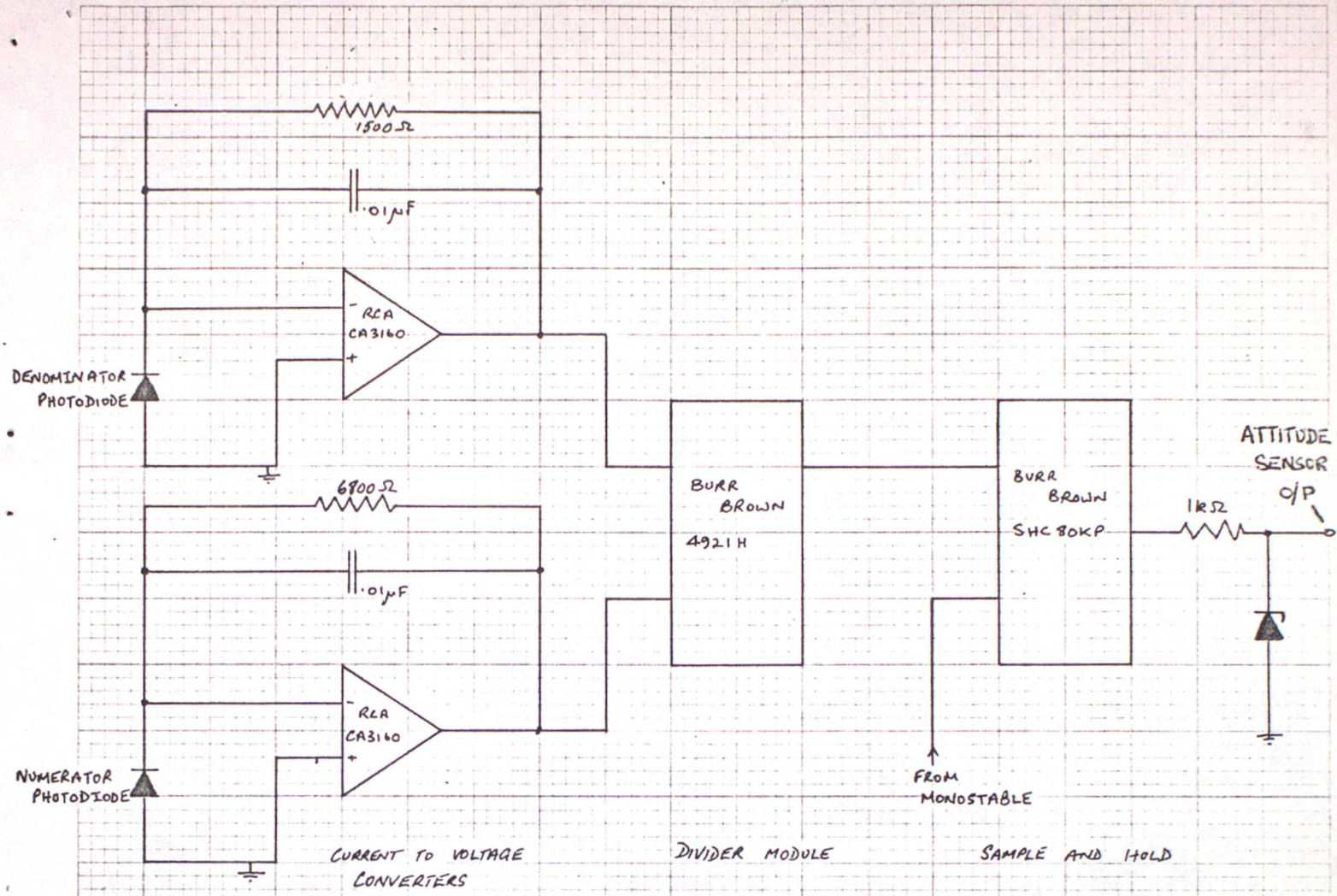

Fig. 5.9(ii) MOP3 ATTITUDE SENSOR CIRCUIT

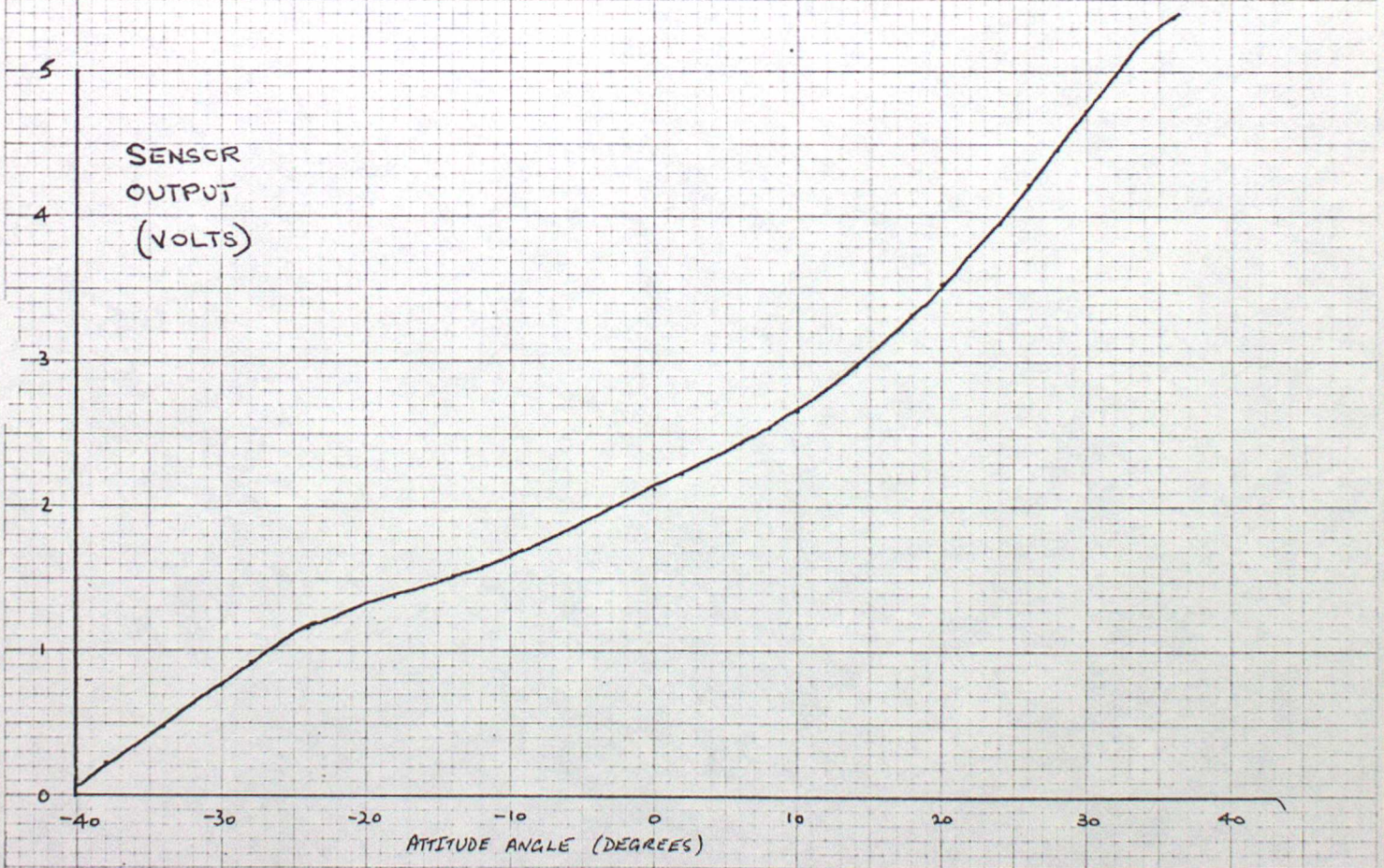

Fig 5.9(iii) CALIBRATION OF MOP3 ATTITUDE SENSOR

E.R.

FIG 5.9 (iv)

DAWN ATTITUDE SENSOR

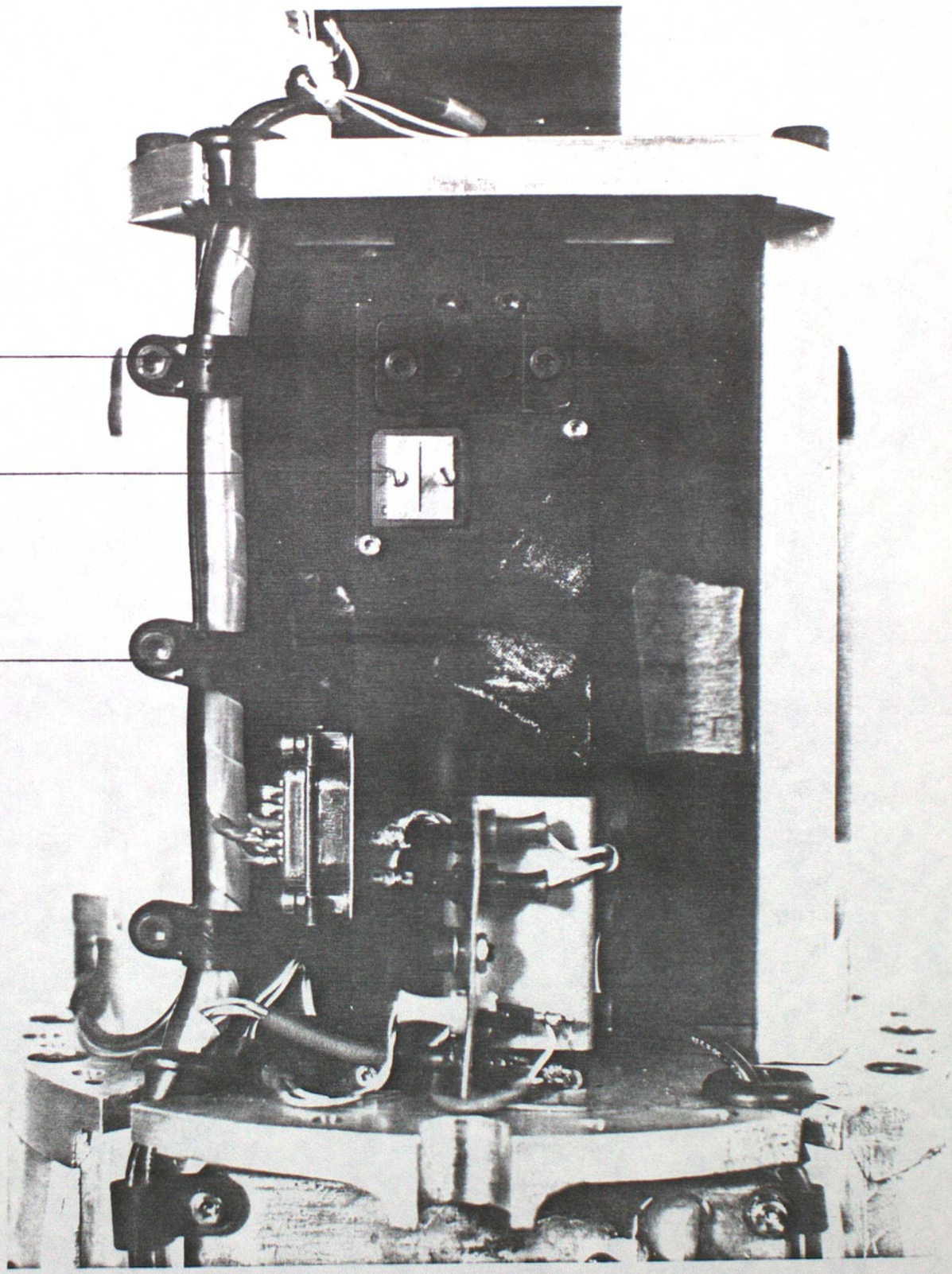

FIG. 5.10

LUNAR ATTITUDE SENSOR

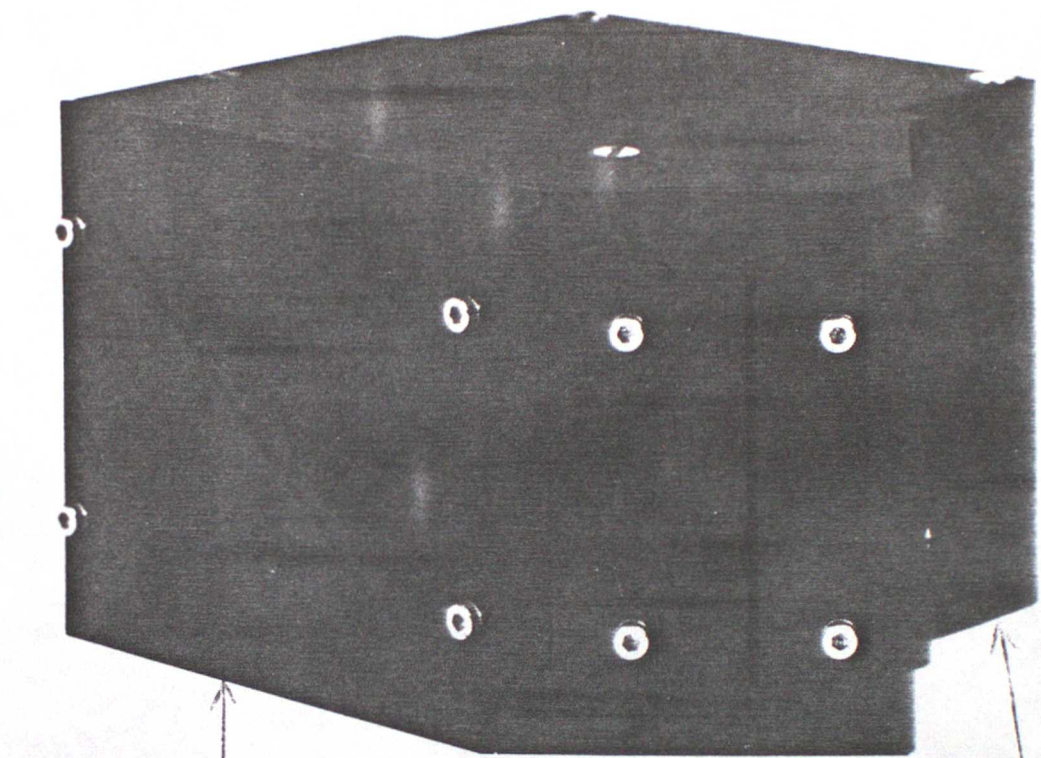

Appendix A Some Notes on Photomultiplier Theory

a) Time Resolution

When counting pulses from a photomultiplier it is necessary to ensure that there is negligible overlap between pulses emanating from different photons. This in turn depends on the time response of the tube, which is something of this form:

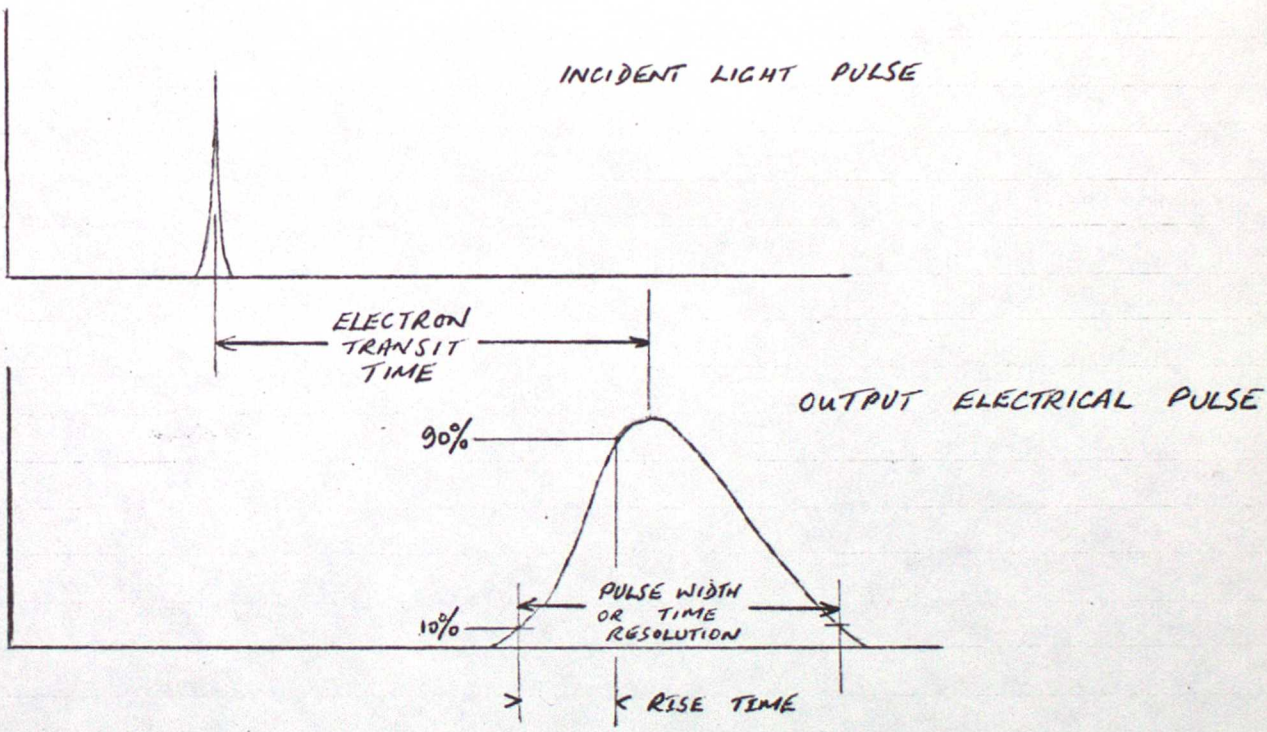

For the R4315 rise time was ~ 15ns (so pulse width was ~ 50ns)

If the tube operates in an analogue mode pulse bunching as such is not a problem since the electronics measures the total current from the tube, which is proportional to the light intensity. This state of affairs remains true while the photocurrent is much less than (<1%) the dynode current; for higher currents the tube exhibits saturation and current is no longer directly proportional to light intensity.

b) Photon Counting

Pulses may be emitted from a photomultiplier due either to incident photons or 'dark electrons' (e.g. thermal noise). The pulses vary in height, and the pulse height distribution depends on the type of tube, e.g.

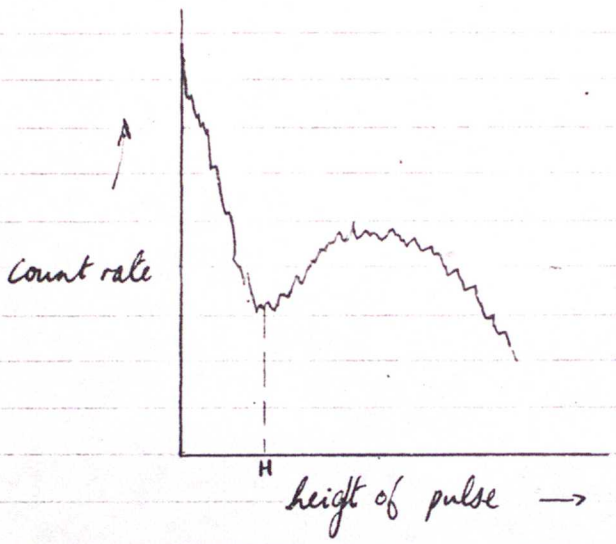

(a)

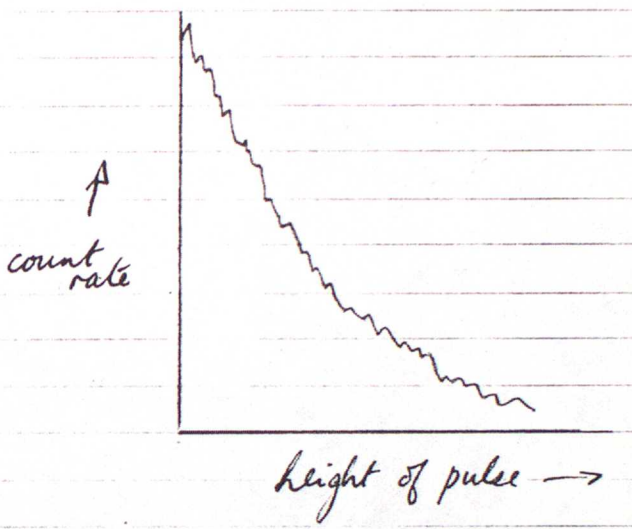

(b)

For tube (a) it is possible to set a discriminator to reject pulses with height < H as dark pulses and counting only those pulses > H. For tube (b) it is not so easy to set the discriminator. Manufacturers try to build tubes for photon counting with pulse height distribution as in a); the HTV R4315 was not built with photon counting in mind.

(c) Photomultiplier noise for a photon counting system

The photon arrival rate is governed by the Poisson distribution, i.e.

probability of r photons reaching photocathode in time Δt seconds $= \frac{(I_0 \Delta t)^r}{r!} \exp - I_0 \Delta t$

where I_0 is the mean photon arrival rate (per second).

For the Poisson distribution

$$\langle r \rangle = I_0 \Delta t$$
$$\langle r^2 \rangle = \langle r \rangle^2 + \langle r \rangle$$

Therefore the standard deviation is $(I_0 \Delta t)^{\frac{1}{2}}$, as is the signal to noise ratio. A similar distribution governs the emission of electrons from the cathode in response to I_0, and, in the symbols used above, ignoring dark current:

signal to noise ratio $= (Q I_0 \Delta t)^{\frac{1}{2}}$

where Q = quantum efficiency of photocathode.
Δt = effective width of light pulse
I_0 = peak photon arrival rate

(d) Photomultiplier noise for an analogue system

Consider the following preamplifier:

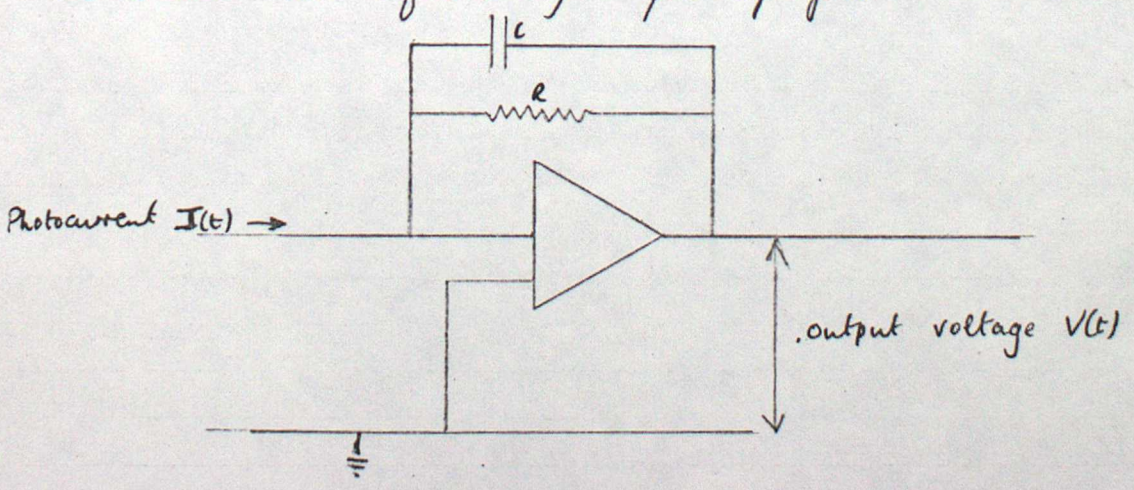

Consider a number of discrete packets of charge q arriving at the input of the amplifier. They last for a very short time (~5ons, sect. A), so for an amplifier time constant of a few ms they can be considered as being stored entirely on C. This gives rise to a voltage $V = -q/C$ per pulse.

Suppose a moon pulse is divided up into time periods $\tau_1, \tau_2, \ldots \tau_n$, each of length τ. The voltage at the end of the n^{th} period is V_n, and r_n packets arrive in that period.

Then $V_n = V_{n-1} \exp - \tau/RC + q/C \, r_n$

The recurrence relation may be stated

$$V_n = -\sum_{s=1}^{n} \frac{q}{C} r_s \exp - (n-s)\frac{\tau}{RC}$$

if V was 0 at the beginning

Clearly then

$$\langle V_n \rangle = -\sum_{s=1}^{n} \frac{q}{C} \langle r_s \rangle \exp - (n-s)\frac{\tau}{RC}$$

from which the formula in Appendix B may be derived.

If $\sigma_n^2 = \langle V_n^2 \rangle - \langle V_n \rangle^2$

$$\sigma_n^2 + \langle V_n \rangle^2 = \left\langle \frac{q^2}{C^2} \sum_{s=1}^{n} r_s \exp - (n-s)\frac{\tau}{RC} \sum_{v=1}^{n} r_v \exp - (n-v)\frac{\tau}{RC} \right\rangle$$

$$= \frac{q^2}{C^2} \sum_{s=1}^{n} \sum_{v=1}^{n} \langle r_s r_v \rangle \exp - (2n-s-v)\frac{\tau}{RC}$$

For the Poisson distribution r_s and r_v are independent variables if $s \neq v$ (the no. photons arriving in different time periods are independent of each other).

So $\langle r_s r_v \rangle = \langle r_s \rangle \langle r_v \rangle$ if $s \neq v$

$\langle r_s^2 \rangle = \langle r_s \rangle^2 + \langle r_s \rangle$ (sect. c)

$$\therefore \sigma_n^2 + \langle v_n \rangle^2 = \frac{q^2}{C^2} \sum_{s=1}^{n} \sum_{v=1}^{n} \langle r_s \rangle \langle r_v \rangle \exp - (2n - s - v) \frac{\tau}{RC}$$

$$+ \frac{q^2}{C^2} \sum_{,}^{n} \langle r_s \rangle \exp - 2(n-s) \frac{\tau}{RC}$$

$$= \langle v_n \rangle^2 + \frac{q^2}{C^2} \sum_{,}^{n} \langle r_s \rangle \exp - 2(n-s) \frac{\tau}{RC}$$

$$\therefore \sigma_n^2 = \frac{q^2}{C^2} \sum_{,}^{n} \langle r_s \rangle \exp - 2(n-s) \frac{\tau}{RC}$$

For time steps $\tau \ll$ characteristic time of anode pulse this equation may be replaced by an integral.

$q \langle r_s \rangle = J(t)\, dt$ where $J(t)$ = photomultiplier current

$\sigma_n = \sigma(T)$

$n\tau = T$

$s\tau = t$

$$\therefore \sigma_n^2 = \frac{q}{C^2} \int_{-\infty}^{T} J(t) \exp - \frac{2(T-t)}{RC}\, dt$$

Then signal to noise ratio

$$\frac{V}{\sigma} = \frac{\frac{1}{C} \int_{-\infty}^{T} J(t) \exp - \frac{(T-t)}{RC}\, dt}{\left\{ q/C^2 \int_{-\infty}^{T} J(t) \exp - \frac{2(T-t)}{RC}\, dt \right\}^{1/2}}$$

write $J(t) = qN_0(t) + q\mathcal{E}$

where $N_0(t)$ = mean cathode electron emission rate at time t

$\mathcal{E}$ = equivalent to $N_0(t)$ in dark current

Then Signal $= N_0(t)$ since $\mathcal{E}$ is not part of the signal we want

and $$\frac{V}{\sigma} = \frac{\int_{-\infty}^{T} N_0(t) \exp - \left(\frac{T-t}{RC}\right) dt}{\left\{ \int_{-\infty}^{T} (N_0(t) + \mathcal{E}) \exp - \frac{2(T-t)}{RC}\, dt \right\}^{1/2}}$$

An example of the effect of this equation on a real pulse is shown in fig A(i) for the MO16 265nm sensor full moon pulses.

For a steady photocurrent (or a pulse whose characteristic time is $>> RC$)

$$\frac{V}{\sigma} = \left(2 \frac{N_0^2}{N_0 + \Sigma} RC \right)^{1/2}$$

Ignoring Σ which was small V/σ would be 103 for the MOP6 sensors in a steady state.

e) Effect of Pulse Bunching on Nonlinearity of response

Suppose a system consisting of a tube and a discriminator which rejects pulses below a certain height value. The time resolution of the tube is τ. Suppose pulses are counted for period T. The number of photoelectrons emitted from the cathode is $J_0 T$ and the number of pulses counted is $J_D T$ (J_0, J_D are mean counting rates).

The time during which a pulse is being detected is $J_D T \tau$. The expected number of undetected pulses is therefore $J_0 J_D T \tau$

$$\text{So} \quad J_0 T = J_D T + J_0 J_D T \tau$$

$$\text{whence} \quad J_0 / J_0 = \frac{1}{1 + J_0 \tau}$$

which is a factor describing the nonlinearity of the pulse counting rate with light intensity.

MOPi 265 nm sensor.

(a) : D.C. ROLL CALIBRATION AT 266 nm AS A % OF NORMAL INCIDENCE

(b) : PULSE SHAPE EXPECTED IN FLIGHT $\frac{V(T)}{R}$, AS A % OF THE D.C. NORMAL INCIDENCE VALUE

(c) : EXPECTED SIGNAL/NOISE RATIO FROM THE AMPLIFIER FOR PEAK CATHODE ELECTRON EMISSION RATE $1.6 \times 10^6\ s^{-1}$ (photon noise only)

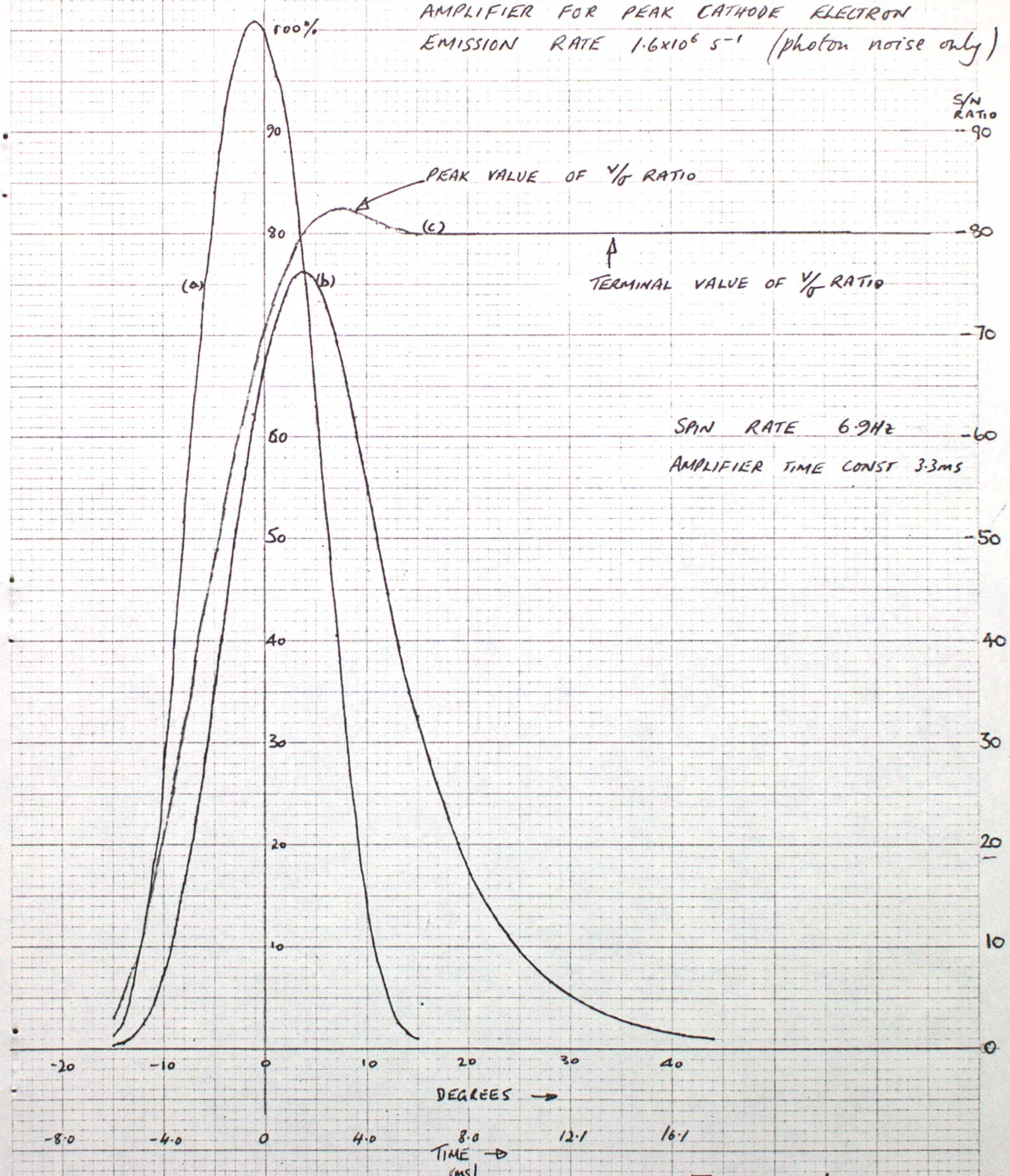

FIGURE A(i)

E.R.

Appendix B: Effect of a slow amplifier on an input pulse

(i) Consider a current pulse $I(t)$ being converted to a voltage pulse $V(t)$ by the following amplifier:

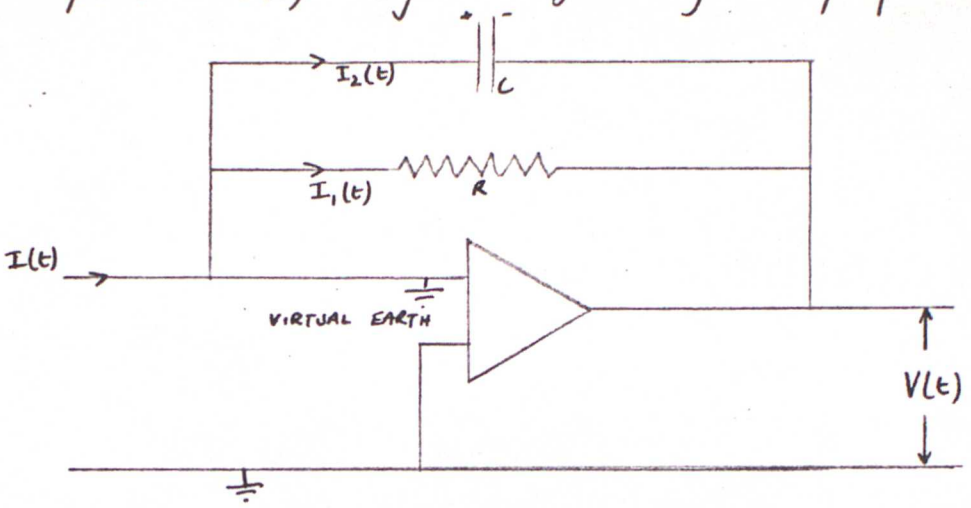

$$V(t) = -I_1(t)\,R \qquad - \quad 1$$

$$I_1(t) + I_2(t) = I(t) \qquad - \quad 2$$

$$\frac{\partial V(t)}{\partial t} = -\frac{1}{C} I_2(t) \qquad - \quad 3$$

Eliminating I_1, I_2:

$$\frac{\partial V}{\partial t} = -\frac{V}{RC} - \frac{1}{C} I(t)$$

$$\therefore \quad \frac{\partial V}{\partial t} \exp t/RC + \frac{V}{RC} \exp t/RC = -\frac{1}{C} I(t) \exp t/RC$$

$$\therefore \quad V(T) = -\frac{1}{C}\int_{-\infty}^{T} I(t) \exp -\left(\frac{T-t}{RC}\right) dt$$

assuming that $I(-\infty) = 0$!

(ii) The effect of such a function on the shape of a pulse is shown in fig. A In this figure, however, the area underneath both black and red curves is identical; what the pulse

loses in height it gains in width:

$$-\frac{1}{R}\int_{-\infty}^{\infty} V(T)\,dT = +\frac{1}{RC}\int_{-\infty}^{\infty} dT \int_{-\infty}^{T} I(t)\exp-\left(\frac{T-t}{RC}\right) dt$$

$$+\frac{1}{RC}\int_{-\infty}^{\infty} dT \exp-T/RC \int_{-\infty}^{T} I(t)\exp+t/RC\,dt$$

Writing $F(T) = \int_{-\infty}^{T} I(t)\exp t/RC\,dt$

Then $\frac{dF}{dT} = I(T)\exp T/RC$

$$\therefore -\frac{1}{R}\int_{-\infty}^{\infty} V(T)dT = \frac{1}{RC}\int_{-\infty}^{\infty} dT \exp-T/RC\, F(T)$$

Integrate by parts

$$= \frac{1}{RC}\left\{\left[-RC\,F(T)\exp-T/RC\right]_{-\infty}^{\infty} + RC\int_{-\infty}^{\infty}\frac{dF}{dT}\exp-T/RC\,dT\right\}$$

Given that $I(-\infty) = 0$ then $F(-\infty) = 0$ so

$$-\frac{1}{R}\int_{-\infty}^{\infty} V(T)dT = \int_{-\infty}^{\infty} I(T)dT$$

Appendix C: Occultation Geometry

In the occultation method the detector views the source by looking down through the atmosphere. The resulting long path length makes the method especially suitable for measuring concentrations of minor constituents by absorption spectroscopy.

a) Definition of Grazing Ray Height.

For a non-refracting atmosphere, consider a ray from a point source to a detector on a rocket.

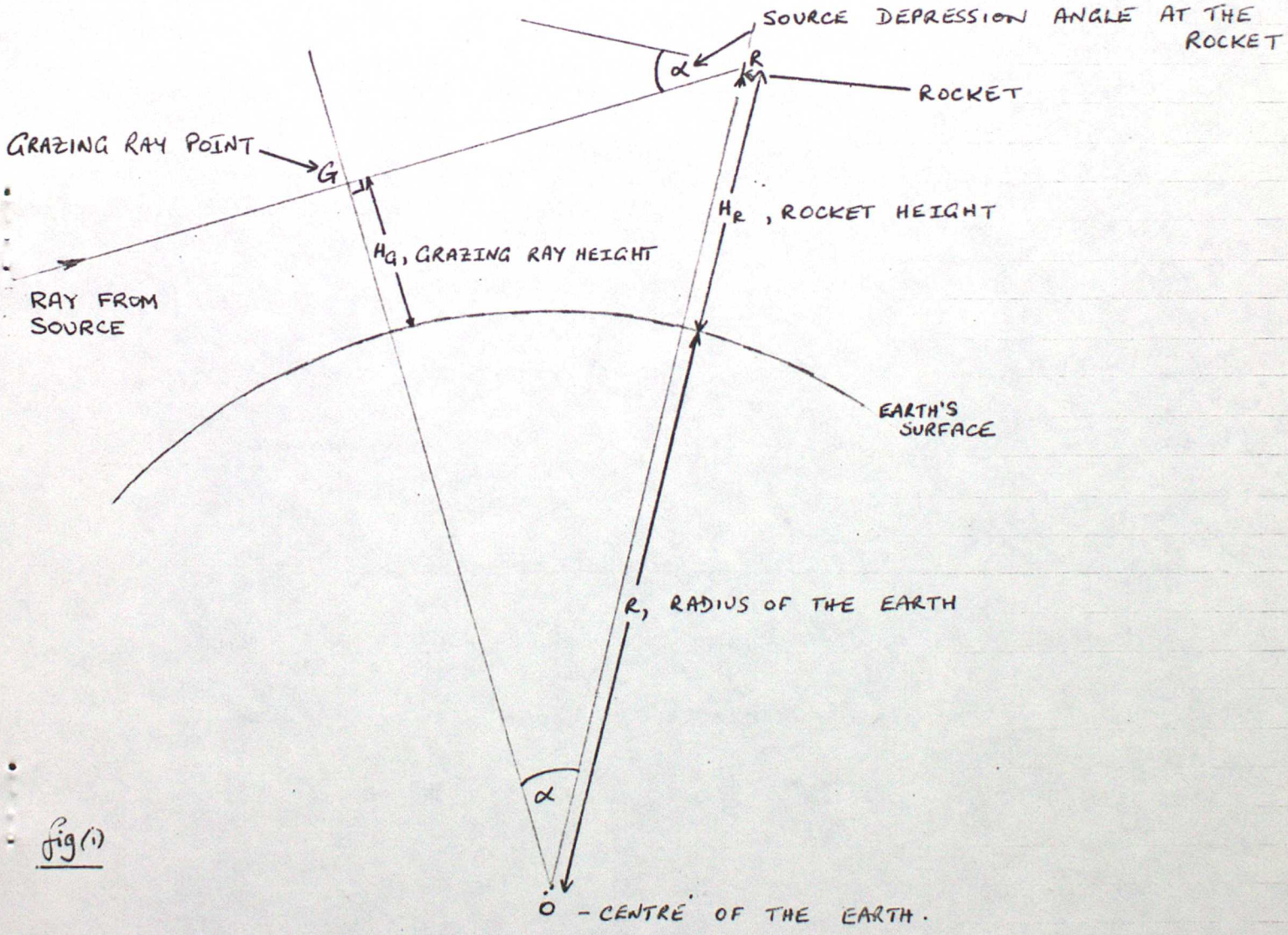

fig(1)

The Grazing Ray Height is defined as the height of closest approach of the ray to the earth's surface. It is clear from ΔOGR that

$$\cos\alpha = \frac{R + H_G}{R + H_R}$$

For rockets $H_G, H_R \ll R$ so:

$$\cos\alpha = 1 - \tfrac{1}{R}(H_R - H_G)$$

For $\alpha < 5°$, $\cos\alpha = 1 - \frac{1}{2}\alpha^2$ to within 3 parts in 10^6 so:

$$H_G = H_R - \tfrac{1}{2}R\alpha^2 \quad \text{, with } \alpha \text{ in radians}$$

By a numerical coincidence, the conversion factor from radians to degrees, when squared, is equal to $\frac{2}{6566}$. To within 3% accuracy one can therefore write

$$H_G = H_R - \alpha^2 \quad \text{, where } H_G, H_R \text{ are in km, } \alpha \text{ is in degrees.}$$

For grazing ray heights above 40km the effects of refraction are negligible (deviation of a ray is $\sim .01°$ at 40km) and the simple treatment given here is accurate.

b) <u>Effect of a source of finite angular size</u>

Suppose the source has angular size ω, and α refers to the depression angle of its centre. Referring to fig.(ii), the grazing ray point now becomes a range of heights, of magnitude ΔH.

$$\Delta H = L\omega$$

$$= \omega(R + H_R)\sin\alpha \quad \text{(see fig.(i))}$$

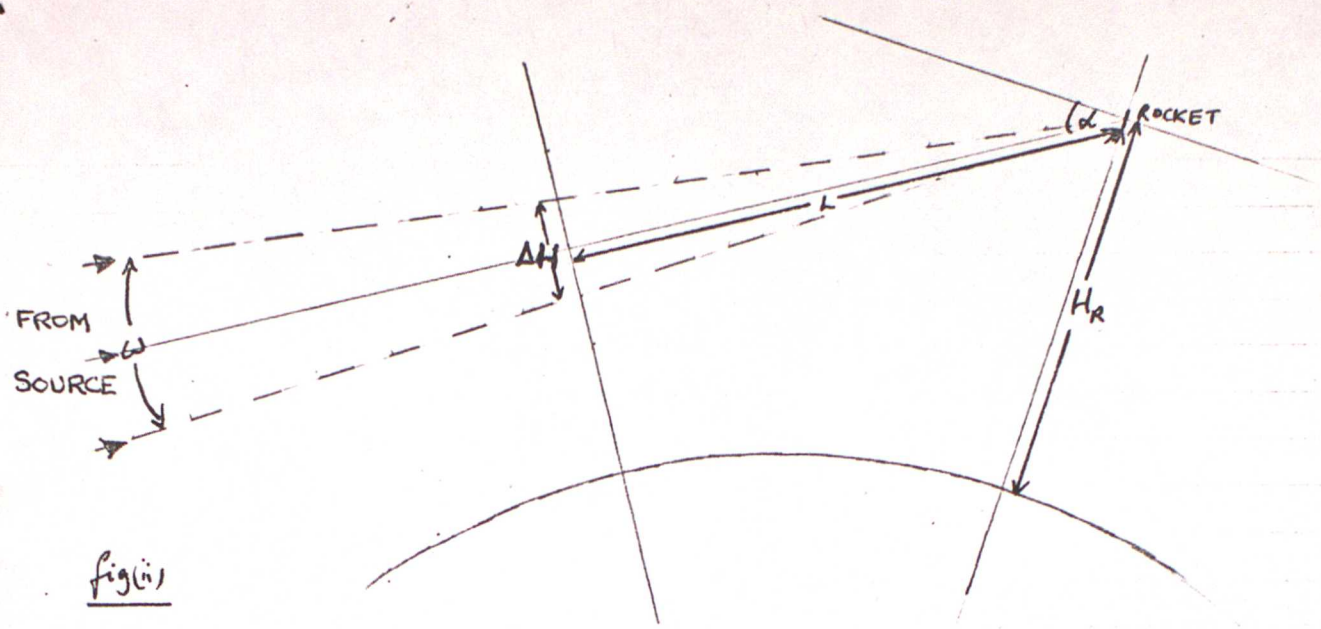

fig(ii)

Since α is small $\sin\alpha \approx \alpha$ and also $H_R << R$ so

$$\Delta H = R\alpha\omega .$$

Once again conversion of α and ω from radians to degrees allows one to write

$$\Delta H = 2\alpha\omega \quad \text{in km.}$$

and, since both sun and moon have $\omega \sim \frac{1}{2}^\circ$

$$\Delta H \sim \alpha \quad \text{km for these two sources.}$$

The finite size of the source therefore limits the height resolution possible with an occultation measurment.

Appendix D : Ray Tracing through a Lens.

Consider parallel light incident at an angle θ to the axis of an acylindrical lens, that is, a lens whose cross-section does not vary along its length. The objective of the ray tracing as far as sensor design is concerned may be understood by reference to fig. D. Given incident light at an angle θ to the axis of the lens one needs to know the 'apparent displacement' z of the ray emanating at an angle ψ to the axis on the other side. A knowlege of $z(\theta, \psi)$ enables the lens to be treated as a flat plate in the sensor design.

The shape of the two sides of the lens are defined with reference to points A and B, and are given in polar form by $r_1(\delta)$ and $r_2(\psi)$. The angles ϕ_1 and ϕ_2 between the radius vector and the normal to the surface may be derived as follows:

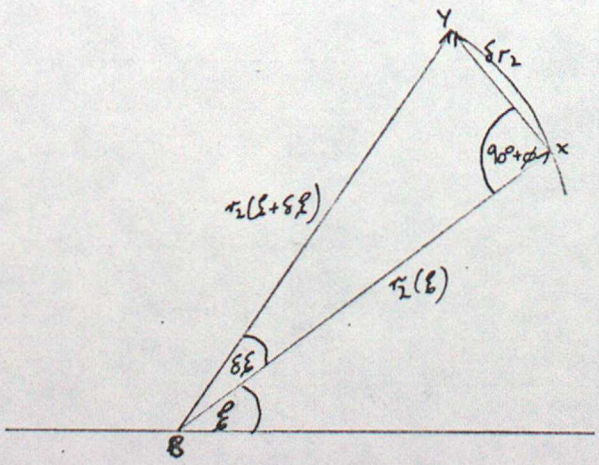

Fig D(i)

Consider a very small displacement along the surface of the lens and apply the sine rule to triangle BXY:

$$\frac{r_2(\xi)}{\sin(\pi - (\xi_\xi + \pi/2 + \phi))} = \frac{r_2(\xi + \delta\xi)}{\sin(\pi/2 + \phi)}$$

from which, by expansion using Taylor's theorem:

$$\frac{\partial r_2}{\partial \xi}\cos\phi - r_2(\xi)\sin\phi + O(\delta\xi) = 0$$

and therefore $$\tan\phi_2 = \frac{1}{r_2(\xi)}\frac{\partial r_2(\xi)}{\partial \xi} \quad \text{— 1}$$

similarly $$\tan\phi_1 = \frac{1}{r_1(\delta)}\frac{\partial r_1(\delta)}{\partial \delta} \quad \text{— 2}$$

Returning to the ray tracing, and applying Snell's law at the entrance and exit of the ray from the lens:

$$n \sin a_1 = \sin(\theta + \delta - \phi_1) \quad \text{— 3}$$

$$n \sin a_2 = \sin(\xi + \gamma - \phi_2) \quad \text{— 4}$$

It is also clear from the triangle formed by the two normals at the exit and entrance points and the ~~line~~ ray path between them that:

$$a_1 + a_2 = \delta - \phi_1 + \xi - \phi_2 \quad \text{— 5}$$

To couple the two sides of the lens one may express the displacement of the exit point Q from the axis in two ways:

1) displacement = $r_2 \sin\xi$

2) displacement = $r_1 \sin\delta - (r_1(0) - r_1\cos\delta + d + r_2(0) - r_2\cos\xi)\tan(a_1 + \phi_1 - \delta)$

where $r_1(0)$ and $r_2(0)$ are the 'radii' of the lens along the axis. These two equations may be combined to give

$$r_2 \sin\left(\xi + (\delta - a_1 - \phi_1)\right) = \left(r_1 \sin\delta + (r_2(0) + r_1(0) + d - r_1\cos\delta)\tan(\delta - a_1 - \phi_1)\right)\cos(\delta - a_1 - \phi_1)$$

— eqn. 6

Finally an expression for z is needed

$$z + (d/2 + r_2(0) - r_2\cos\xi)\tan\psi = r_2\sin\xi$$

or

$$z = r_2(\xi)\sin(\xi + \psi)\sec\psi - (r_2(0) + d/2)\tan\psi \quad - 7.$$

These seven equations provide the information needed to derive $z(\theta, \psi)$. To solve them a computer program was written using an iterative method.

The attenuation of the beam's intensity a distance x from the lens is given by

$$\text{attenuation} = \left(\frac{1}{1 + x\,\partial\psi/\partial z}\right)\cos\theta$$

This was computed numerically and allowed predictions of the angular response of the sensor to be made assuming perfect transmission through the lens.

E.R.

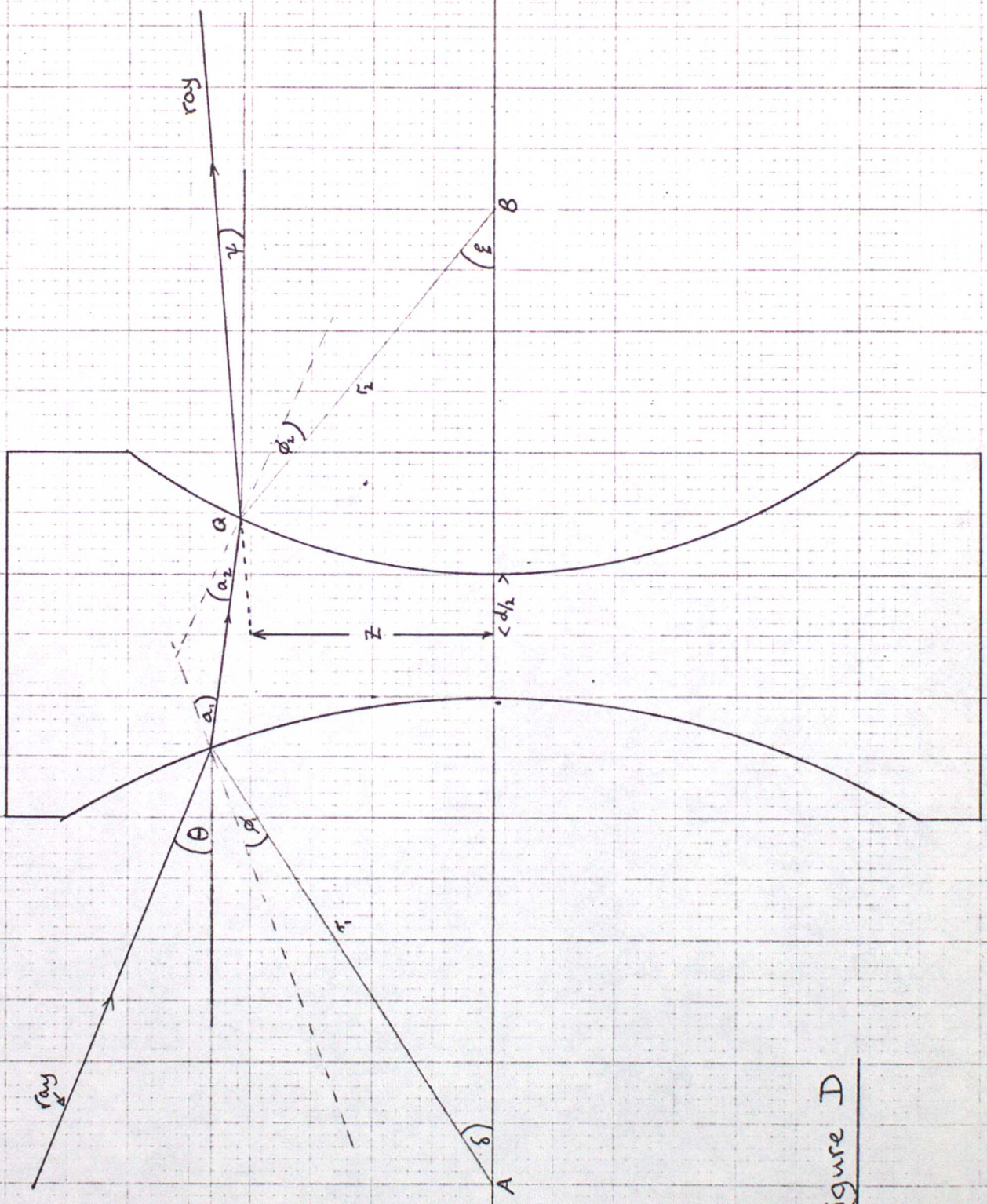

Figure D

Appendix E : Geometry of the Two-Slit Attitude sensor

The principle of this sensor is that the angle (in roll) when the diode behind the inclined slit is illuminated depends on the pitch angle of illumination. The relation between the two is described here.

(i) Consider a slit inclined at an angle α to the vertical in a flat vertical plate. A distance d horizontally behind the centre C of the slit is a diode D. The diode is illuminated at an angle θ to the horizontal, through a point P on the slit whose angular displacement from the centre of the plate has a horizontal component γ.

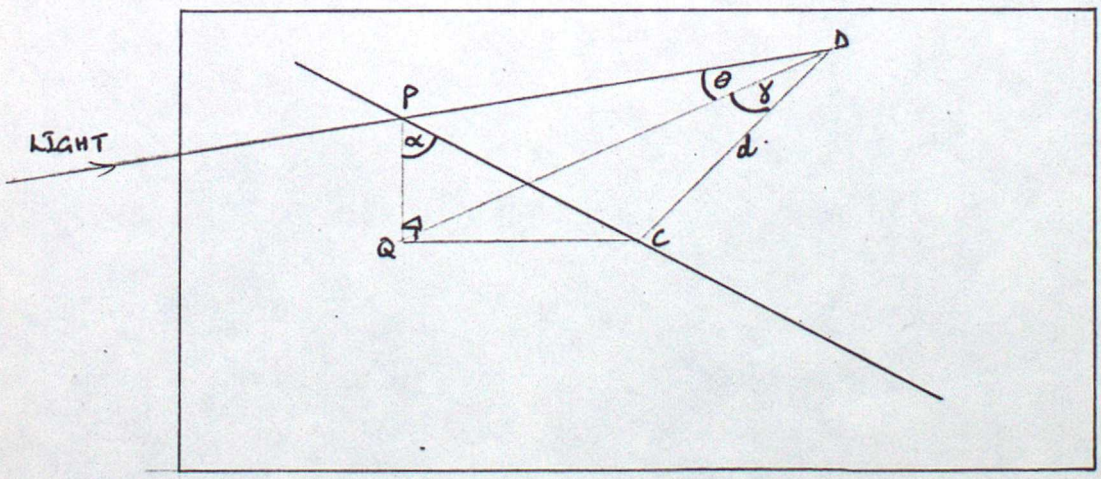

For Point Q as shown, $CD = d$ (perpendicular to the plate)

$$QC = d \tan\gamma$$

$$QD = d \sec\gamma$$

$$\therefore \quad PQ = d \sec\gamma \tan\theta$$

$$\text{So} \quad \tan\alpha = \frac{\tan\gamma}{\sec\gamma \tan\theta}$$

$$\therefore \quad \sin\gamma = \tan\theta \tan\alpha$$

(ii) For rocket spin rate ν Hz, the time delay between the triggering of the vertical and inclined slit diodes is

$$t = \frac{1}{2\pi\nu}(\gamma_0 + \gamma)$$

where γ_0 = angular separation in roll between illumination of vertical diode and inclined diode for $\theta = 0$.

Relationship between γ and θ for $\alpha = 50°$

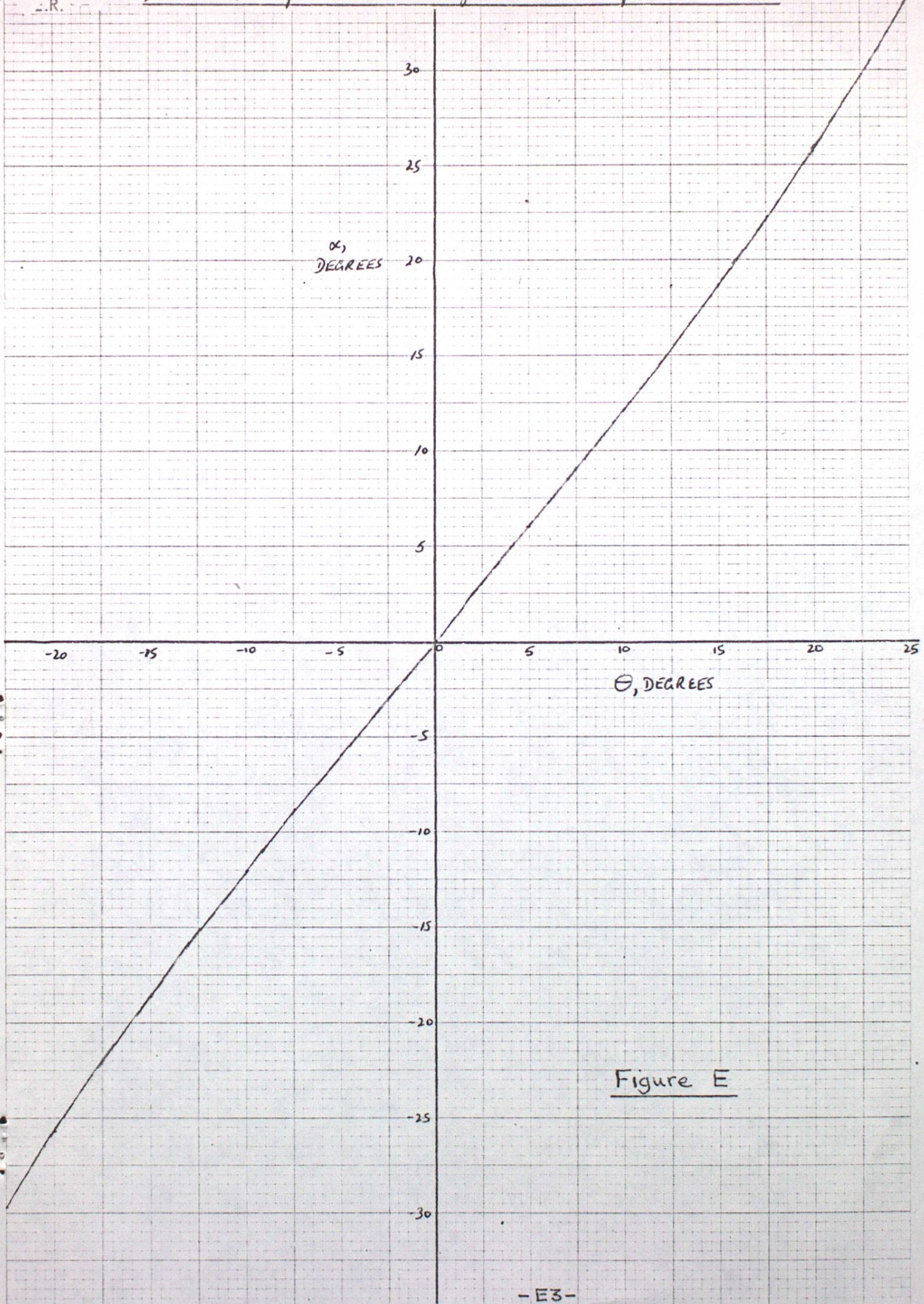

Figure E